9-1-2018

Arrhenius Rate Chemistry Informed Inter-phase Source Terms (ARCIIST) for Macro-Scale Explosive Hydrocodes

Matthew J. Schwaab

Arrhenius Rate Chemistry Informed Inter-phase Source Terms (ARCIIST) for Macro-Scale Explosive Hydrocodes

DISSERTATION

Matthew J. Schwaab, Maj, USAF

AFIT-ENY-DS-18-S-072

DEPARTMENT OF THE AIR FORCE
AIR UNIVERSITY

AIR FORCE INSTITUTE OF TECHNOLOGY

Wright-Patterson Air Force Base, Ohio

AFIT-ENY-DS-18-S-072

ARRHENIUS RATE CHEMISTRY INFORMED INTER-PHASE SOURCE TERMS (ARCIIST) FOR MACRO-SCALE EXPLOSIVE HYDROCODES

DISSERTATION

Presented to the Faculty

Graduate School of Engineering and Management

Air Force Institute of Technology

Air University

Air Education and Training Command

in Partial Fulfillment of the Requirements for the

Degree of Doctor of Philosophy

Matthew J. Schwaab, B.S., M.S.

Maj, USAF

AFIT-ENY-DS-18-S-072

ARRHENIUS RATE CHEMISTRY INFORMED INTER-PHASE SOURCE TERMS (ARCIIST) FOR MACRO-SCALE EXPLOSIVE HYDROCODES

DISSERTATION

Matthew J. Schwaab, B.S., M.S.
Maj, USAF

Committee Membership:

Robert Greendyke, Ph.D.
Chairman

Chad Hale, Ph.D.
Member

Maj Darrell Crowe, Ph.D
Member

Kevin Gross, Ph.D.
Member

Carl Hartsfield, Ph.D.
Dean's Representative

Abstract

A critical factor in hydrocodes designed to simulate explosive material is defining the chemical reaction rate under various conditions. This rate determines how quickly the granular solid explosive is converted to its gaseous products. Currently, the state of the art for macro-scale hydrocodes is to use one of numerous burn models. These burn models are designed to estimate the bulk chemical reaction rate. Unfortunately, these burn rate models are largely based on empirical data and must be recalibrated for every new material being simulated. While these calibration methods are well established, they require full synthesis of the explosive before any simulations can be made. This requirment has prevented macro-scale simulations of detonations from becoming more predictive in characterizing new explosive formulations.

This research proposes that the use of an equilibrium Arrhenius rate reacting chemistry model in place of these empirically derived burn models can improve the accuracy for these computational codes. To accomplish this, the Arrhenius Rate Chemistry Informed Inter-Phase Source Term (ARCIIST) method for multi-phase continuum hydrocodes has been developed. In essence, ARCIIST creates an interface between a series of zero-dimension constant volume thermal explosion (CVTEX) simulations and the macro-scale hydrocode. The information from the CVTEX simulations is used to determine the mass transition rate between the condensed and gaseous phases of a reacting explosive. In this manner, the hydrocode is transformed into a simultaneous multi-scale simulation capable of capturing the complexities of deflagration to detonation transition (DDT).

ARCIIST was tested by incorporating an Arrhenius reacting chemistry model developed for the cyclic-nitramine RDX by the Naval Research Laboratory (NRL)

into the Air Force Research Laboratory's (AFRL) Multi-Phase Explosive Simulation (MPEXS) continuum hydrocode. NRLs chemistry model itself is based largely on theoretical chemistry, thus creating a pathway to create predictive macro-scale models without any synthesis of the explosive itself.

MPEXS simulations of RDX using ARCIIST have been compared to identical simulations using more common, pressure dependent burn models. Results indicate that, through the use of ARCIIST, MPEXS can more accurately capture the complex physics of an explosive undergoing DDT. Additionally, the run-to-detonation distances computed by the ARCIIST RDX simulations were compared with experimental data for two RDX based Polymer-Bonded Explosives (PBX). Analysis revealed that the initiation mechanisms inherent in traditional, empirically calibrated burn models are not captured by the ARCIIST method. An ignition sensitivity study was conducted and proved the need to develop accurate hot-spot initiation models to complement ARCIIST in macro-scale hydrocodes.

ARCIIST has successfully linked micro-scale chemical kinetics to macro-scale hydrodynamics. It is, therefore, a critical piece to connecting predictive theoretical chemical kinetics to system scale simulations with less reliance on empirical data.

This dissertation is dedicated to my children. You all are the motivation behind everything I do.

Acknowledgements

I would like to thank Dr. Michael Crochet and Dr. Igor Schweigert upon whose work this research is built. Thank you for the generous use of your source material as well as the time and guidance you provided. I would also like to thank Dr. Robert Greendyke, Dr. Bryan Steward, and my entire committee for their instruction and guidance during this research.

To my family, thank you for being so supportive of me during this ordeal. In particular, thank you to my wife who has not only kept our personal lives on track but voluntarily agreed to proofread this document in its entirety.

Matthew J. Schwaab

Table of Contents

Page

List of Figures

Figure Page

List of Tables

List of Acronyms

AFRL Air Force Research Laboratory

ALE3D Arbitrary-Lagrangian-Eulerian Three Dimentional Finite Element Code

ARCIIST Arrhenius Rate Chemistry Informed Inter-phase Source Terms

BN Baer and Nunziato

CJ Chapman-Jouguet

CFL Courant-Friedrichs-Lewy

CREST Computational Reaction Evolution dependent on Entropy(S) and Time

CVTEX Constant Volume Thermal Explosion

DDT Deflagration to Detonation Transition

DFT Density Functional Theory

EOS Equations of State

HE High Explosives

HMX cyclotetramethylenetetranitramine

JWL Jones-Wilkins-Lee

KNP Kurganov-Noelle-Petrova

LANL Los Alamos National Laboratory

MCBM Multi-Phase Convective Burn Model

MG Mie-Gruneisen

MPEXS Multi-Phase Explosive Simulation

NRL Naval Research Laboratory

ODE Ordinary Differential Equations

PBX Polymer-Bonded Explosives

RDX cyclotrimethylenetrinitramine

SIG Simplified Ignition and Growth

SPD Simple Pressure-Dependent

SURF Scales Uniform Ractive Front

USAF United States Air Force

ZND Zeldovich, Von Neumann, and Deering

0-D Zero-Dimension

List of Symbols

α_{sg} drag partitioning function

$\alpha_{i,r}$ reactant stochiometric coefficient

A Arrhenius preexponential parameter

$\mathcal{A}$ JWL constant

a_x wave propagation speed

$\mathcal{B}$ JWL constant

β_s inter-granular stress

$\beta_{i,r}$ product stochiometric coefficient

$\mathcal{C}$ mass source term

C_v specific heat coefficient

c_o 1st Hugoniot constant

c_{sg} compaction partitioning function

$\breve{c}$ CFL number

D Detonation velocity

δ_{sg} drag coefficient

Δt time step size

Δx cell length

$\overline{E}$ energy source term

E_a activation energy

E_i i-th solid total specific energy

E_g gas total specific energy

Γ Gruneisen coefficient

H_{sg} heat transfer coefficient

k Arrhenius rate coefficient

κ burn rate constant

λ mass fraction

λ_s mass fraction of the condensed phase

λ_g mass fraction of the gas phase

m_i mass of the i-th species

$\overline{m}$ mass of the mixture

M_i molecular weight of the i-th species

μ_{sg} compaction viscosity

n Arrhenius preexponential parameter

N pressure exponent

N_x spatial refinement level

N_s number of species in the condensed phase

N_g number of species in the gas phase

ν depletion exponent

$\overline{P}$ mixture pressure

P_{CJ} CJ pressure

P_i i-th condensed phase pressure

P_{ign} ignition pressure

P_g gas pressure

P_s condensed phase pressure

ϕ_i i-th solid volume fraction

ϕ_s condensed phase volume fraction

Ψ ignition sensitivity factor

$R_{b,r}$ backward reaction rate

$R_{f,r}$ forward reaction rate

R_1 JWL constant

R_2 JWL constant

$\overline{\rho}$ mixture density

ρ_i i-th solid density

ρ_g gas density

$\rho_{o,s}$ initial condensed phase density

$\overline{\rho_o}$ initial mixture density

ρ_s condensed phase density

s 2nd Hugoniot constant

σ reaction rate prefactor

t time

$\overline{T}$ mixture temperature

T_g gas temperature

T_{IS} increased sensitivity temperature

T_o initial temperature

$\overline{T_o}$ initial mixture temperature

T_s condensed phase temperature

$\overline{u}$ mixture particle velocity

u_i i-th solid particle velocity

u_p piston velocity

ω JWL constant

$\dot{\omega}_i$ net species production rate

x position

ξ_{sg} chemical reaction partitioning function

X_i mole ratio of chemical species i

Y_i mass ratio of chemical species i

ARRHENIUS RATE CHEMISTRY INFORMED INTER-PHASE SOURCE TERMS (ARCIIST) FOR MACRO-SCALE EXPLOSIVE HYDROCODES

I. Introduction

The development of munitions containing High Explosives (HE) is particularly challenging due to the necessity to fulfill contradictory requirements. The ultimate goal of all HE munitions is to destroy its intended target through one or more damage mechanisms. These mechanisms include destruction through blast or overpressure, dispersal of high velocity fragments of the bomb body, and incendiary effects [22]. If the HE is sensitive to ignition and produces a strong detonation wave, it is very likely to produce the desired damage mechanism.

Unfortunately, in order to deliver a munition to the desired target it must first be constructed, handled, and transported by friendly forces. Often, this includes hostile environments such as captive carry on fighter aircraft where the munition may experience constant vibrations, turbulence, and high-G maneuvers. MIL-STD-2105D calls for an extensive series of tests to be conducted on no fewer than 18 test articles for insensitive munitions before they can be fielded. At least three such test articles must undergo vibration and 12-meter drop testing to simulate the "most intense vibration environment" it would encounter in its life cycle and accidental mishandling respectively [1]. Simulations, such as those proposed in this research, cannot entirely replace such testing. However, they can add greater confidence to the results and may even lead to a reduction in the number of test articles needed.

In recent conflicts, the need to penetrate through hardened targets before detonation has become a necessity. In these circumstances, the HE fill must be able to

withstand extremely rapid deceleration on impact with the target without exploding. Thus, modern HE munitions must be insensitive enough to remain dormant in these scenarios. Simultaneously, they must still detonate when set off by a fuse at the appropriate time. Determining the reliability of warheads designed for this mission is of critical importance to United States Air Force (USAF) munitions programs [30].

The development of HE munitions is further constrained by current efforts to reduce collateral damage. Although limiting impact to non-combatants has always been a consideration of war planners, it has become even more critical in the war on terrorism. Often enemy combatants will intentionally position themselves amongst civilian populations in order to be harder to find and target. Thus, HE munitions must be designed to optimize their damage mechanism such that only the desired target is affected.

Numerous computational models have been developed to aid in designing or improving HE fills for munitions. The biggest challenge for these HE simulations is how to handle the multi-phase physics of these energetic materials. To be successful, the models must include methods for capturing the exchange of mass, momentum, and energy between the phases.

Multi-phase hydrocodes commonly employ burn models to establish these exchange rates between phases. These burn models are designed to capture the bulk chemical reaction rate for a given explosive. Unfortunately, they are largely based on empirical data and must be recalibrated for every new material being simulated. While this may be suitable for well studied explosive compounds, any new explosive material needs to be experimented on extensively before a computational burn model can be established. Furthermore, since these burn models are based on experimentally measurable bulk material parameters, many end up averaging out or completely fail to capture some of the underlying physics of the reactions taking place.

The primary goal of this research was to replace these empirically derived burn models through the development of the ARCIIST technique for macro-scale continuum HE hydrocodes. This development was conducted by incorporating an Arrhenius reacting chemistry model developed for the cyclic-nitramine RDX by the Naval Research Laboratory (NRL) into the Air Force Research Laboratory (AFRL) Multi-Phase Explosive Simulation (MPEXS) continuum hydrocode. By basing the inter-phase mass, momentum, and energy exchange rates on Arrhenius rate reacting chemistry models, the ARCIIST method more accurately captures the underlying physics of shock-induced Deflagration to Detonation Transition (DDT). Furthermore, since the NRL chemistry model itself is based largely on theoretical chemistry, the ARCIIST technique creates a pathway towards more predictive macro-scale models without any synthesis of the explosive itself.

1.1 Overview of Subsequent Chapters

Chapter II provides a review of detonation and DDT theory as well as a description of the development and employment of burn models in explosive hydrocodes. This chapter also outlines the creation of Arrhenius rate chemistry models describing the decomposition of explosive materials. Chapter III gives a detailed description of the computational methodology behind the MPEXS hydrocode which was used as the baseline model to implement and test the new ARCIIST technique. This chapter also presents an overview of the NRL Arrhenius rate chemistry model for RDX. Chapter IV covers the development of the ARCIIST technique and the method in which it was used to implement the NRL chemistry model into MPEXS. Chapter V establishes the simulation parameters and the test matrix used to evaluate ARCIIST. The grid and temporal refinement studies as well as the equation of state verification studies used to define the simulation parameters are provided in this chapter. In Chapter

VI, the results of the MPEXS RDX simulations using ARCIIST are presented and compared to results from simulations using a Simple Pressure Dependant (SPD) and a Simple Ignition and Growth (SIG) burn models. The run-to-detonation distances predicted in these simulations are validated against Pop-Plot data for PBX-9405 and PBX-9407, two Polymer-Bonded Explosives (PBX) which are 93.7% and 94% RDX respectively. Furthermore, the RDX simulations are qualitatively compared to experimental velocity profile data of LX-14 to prove that the ARCIIST technique captures more details of the physics involved in DDT than using traditional burn models. Additionally, the results from the ARCIIST simulations resulted in a model of RDX that was uncharacteristically insensitive to shock initiation. Chapter VI also includes a scheme to modify the ignition sensitivity within ARCIIST as well as the results of a study testing various sensitivity settings. Finally, Chapter VII presents the conclusions reached while evaluating ARCIIST as well as a discussion of future work to be accomplished.

II. Background and Theory

As mentioned in Chapter I, there are many computational models which have been developed to simulate explosive material undergoing detonation. These models vary drastically in their scope, from modeling individual molecular interactions [6][31][38], through simulation of individual HE grains and meso-scale modeling [47][52], to continuum hydrodynamic modeling of multiple munitions [3][15][24][37]. Although their approaches may vary significantly, the end goal of all of these models is to capture the dynamic, and often chaotic, physics of an explosive material as it transitions from ignition to a steady state detonation. The resulting simulations provide details which cannot be captured through experimental methods and serve to validate empirical observations. Through the development of the ARCIIST technique, this research extends the capability of explosive modeling to be more predictive in nature, providing a path towards gaining key insights into the nature of an explosive material without prerequisite empirical data.

This chapter starts with a review of detonation and DDT theory in Sections 2.1 and 2.2. These sections are followed by a discussion of the prevalent use of empirically derived burn models in explosive hydrocodes to capture the mass, momentum, and energy exchange rates between the phases of a reacting explosive. Section 2.4 provides an overview of the development of Arrhenius rate chemistry models to describe the decomposition process of an explosive material. Finally, Section 2.5 outlines how the ARCIIST technique can be used to connect these chemistry models to existing explosive hydrocodes in order to improve their ability to capture the fundamental thermophysics which take place in the DDT process.

2.1 Ideal Detonation Theory

In order for a hydrocode to successfully simulate granular explosive material undergoing detonation, it must not only identify the location of the detonation wave front, but it must also obtain key steady state detonation parameters of the explosive being simulated. It is also crucial that the detonation wave form itself is properly represented.

Zeldovich, Von Neumann, and Deering (ZND) independently derived a simple theory of an ideal detonation in the 1940s [14] [56]. Figure 1 depicts the steady state pressure profile of a detonation wave described by the ZND model. Working from right to left, the vertical line in this figure represents the location of the detonation wave front. This shock wave is traveling to the right through condensed explosive material at a steady velocity (D). At the detonation front itself, the pressure and temperature of the condensed explosive jumps up significantly and initiates the chemical reactions within the explosive. This condition is known as the Von-Neumann spike. Although the Von-Neumann spike is often ignored in simple first-order analysis of explosives, it should be an expected result from the more complex shock hydrodynamics and

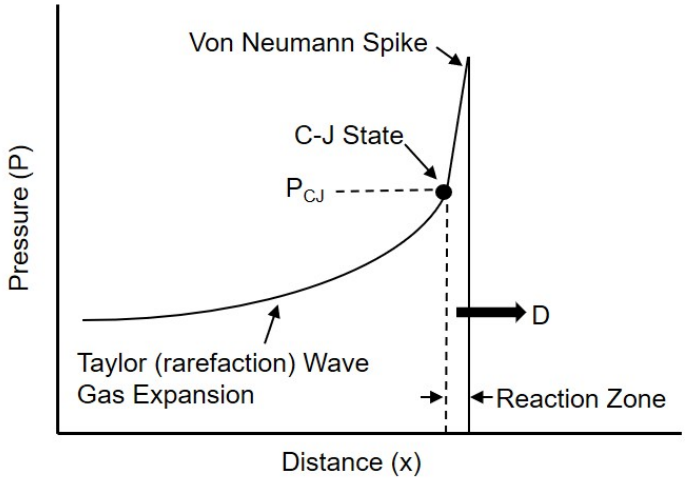

Figure 1. Diagram of an ideal steady state detonation wave.

chemical thermodynamics computed by explosive hydrocodes.

At the end of the reaction zone, all of the condensed explosive has been transformed into its gaseous products. This point is known as the Chapman-Jouguet (CJ) state. Through their experiments on gas-phase detonation in the 1800s, Chapman and Jouguet considered this point to be the steady state detonation condition of an explosive material [14] [56]. The pressure, density and temperature of the explosive products at this point are usually given the subscript "CJ". These CJ conditions are well cataloged for existing explosives and are used to characterize the expected detonation behavior [14] [21] [23] [56]. Thus, the CJ conditions can be used to determine the accuracy of an explosive simulation.

Behind the CJ point, the pressure undergoes a more gradual relaxation as expected from the rarefaction wave which follows any strong shock. The shape of this expansion wave is determined not only by the properties of the detonation products, but also by how confined the explosive material is [14]. Highly confined material results in a shallow curve, while low confinement results in a steeper curve. At the extreme, an unconfined explosive would have a very steep expansion curve following the detonation front striving to rapidly return the products to standard atmospheric conditions.

It will be shown in Sections 6.1 and 6.2 that the implementation of ARCIIST greatly improved MPEXS's ability to properly characterize the detonation wave form and accurately achieve the proper CJ state for RDX.

2.2 Shock Induced Deflagration to Detonation Transition (DDT)

Although characterization of an explosive which has reached detonation is well established, shock induced ignition and the transitional states leading up to full detonation are not fully understood. A packed granular explosive is not a homogeneous material. The prevalent theory regarding shock initiation of an explosive is that "hot-

spots" are formed through the collapsing of voids between grains, grain defects, or other micro-structural mechanisms as the shock wave passes through the explosive [54] [56]. These hot-spots then initiate the thermal decomposition of the explosive which eventually builds to a self-sustaining detonation.

It has been observed that after an initial shock passes through an explosive, there is a small induction time until the reaction rate of the explosive takes off exponentially. The rapid decomposition of the explosive forms a secondary wave front behind the initial shock [10] [56]. In many experiments, this secondary wave is observed as a "hump" forming behind the leading shock [29]. Since the hump is traveling though precompressed material, it travels at a velocity greater than the initial shock. Additionally, the higher pressure, density, and temperature in this region accelerate the chemical reaction rate, building the strength of the secondary wave and further accelerating it. Eventually, this secondary wave overtakes the initial shock to form an overdriven detonation front. This overdriven state continues until rarefaction gradually reduces it to the steady CJ state from ZND theory [56].

Capturing this shock induced DDT behavior is a particular challenge for explosive hydrocodes and is completely dependent on accurately modeling the chemical reaction rate of the explosive material. Most hydrocodes, particularly those operating on the macro-scale level, rely on burn models to estimate the bulk reaction rate of an explosive. It will be shown in Chapter VI that, by incorporating an Arrhenius rate chemistry model, simulations using ARCIIST clearly depict the proper DDT behavior which is missed by common pressure-depended burn models.

2.3 Burn Models

One of the biggest challenges for explosive hydrocodes is how to handle the multiphase physics of these energetic materials. Some models get around this issue by

limiting their simulations exclusively to the unreacted solid explosive [11] [38] or the fully reacted gaseous products [2]. Simulations that strive to capture the multi-phase nature of an explosive undergoing detonation must include methods for capturing the exchange of mass, momentum, and energy between the phases.

Multiphase hydrocodes commonly use burn models to establish these exchange rates between phases. These burn models are designed to capture the bulk chemical reaction rate for a given explosive. Unfortunately, they are largely based on empirical data and must be recalibrated for every new material being simulated. While this may be suitable for well studied explosive compounds, any new explosive material would need to be experimented on extensively before a computational burn model could be established. Furthermore, since these burn models are based on experimentally measurable bulk material parameters, many end up averaging out or completely fail to capture some of the underlying physics of the reactions taking place.

Although numerous burn models are currently in use in continuum explosive hydrocodes, they all serve the same purpose. Namely, they are an expression for prescribing a bulk chemical reaction rate in HE simulations and govern the transition of mass, momentum and energy from one phase to another. Furthermore, although each is derived differently, all of the burn models used in modern HE simulations rely on parameters obtained from experimental data, statistical hot spot models, or a combination of both. Because of this data dependency, all of the existing burn models must be re-calibrated every time a new explosive needs to be simulated.

Pressure-dependent burn models are some of the earliest models developed for continuum simulation shock initiated explosives. These include the Forest Fire model [36] as well as those proposed by Baer and Nunziato [4] and Schwenderman et. al. [46]. In all of these models, the rate of decomposition is described as a function of the local pressure and is usually limited by a depletion term. These models typically

rely on some kind of prefactor term used to "tune" the decomposition rate in order to calibrate the model to existing Pop-Plot data obtained experimentally. Pop-Plots, named after Alphonse Popolato, relate the time or distance it takes for an explosive to transition from deflagration to full detonation against the initial pressure which started the reaction [56]. These plots are currently the best measure of DDT completion for a particular explosive substance under shock induced initiation. However, they do not provide any information on the complex physics that take place during DDT.

Pressure-dependent models assume that the reaction rate of the explosive is directly related to the strength of the shock wave itself. This assumption is in contradiction to the hot-spot formation and ignition process observed in numerous experiments and generally accepted as the initiation of DDT [54] [56]. Furthermore, there is a consensus in the explosives community that reaction rates are more dependent on temperature than pressure [9].

In an attempt to better capture the onset of chemical reactions due to hot spots, Lee and Tarver formulated an Ignition and Growth model. It has been established that shock induced detonation in an explosive can be broken up into two phases [54]. In the first, hot spots are created due to shock compression increasing the temperature in the solid medium, usually where a defect or gap in grains occurs. In the second phase, these hot spots grow and merge as the chemical reaction rate rapidly rises with increased temperature. The initial version of the Lee-Tarver Ignition and Growth model consisted of two terms, one governing the rate of reaction in the ignition phase and a single growth term that takes precedence in the second phase [34]. Based on their initial success, other researchers have created modified or simplified Ignition and Growth burn models [48][53]. While burn models of this form have done a better job capturing the physics behind hot spot induced detonation, they are still pressure-

dependent and rely on calibration to Pop-Plot data. Furthermore, these models often include multiple constants which must be tuned to make the simulation match a particular experimental set up.

The Computational Reaction Evolution dependent on Entropy(S) and Time (CREST) model is one of the most recent burn models developed for continuum based explosive simulations [27][54]. Unlike the previous models, CREST has an entropy-dependent burn model. However this model still relies on experimental calibration. In addition to using the run-to-detonation tests resulting in Pop-Plots, CREST is also calibrated to more recent experiments which incorporate the use of gas-gun particle velocity gauges designed to measure shock strength [28]. As with the previous models mentioned, CREST does not explicitly model hot spot formation, ignition and growth. However, it does show promise in being able to simulate a variety of different experiments without having to be recalibrated each time.

Notably absent from all of the reactive burn models designed for macro-scale continuum based simulations is the use of thermal decomposition which can be described through the use of Arrhenius rate equations. This absence is particularly concerning considering the aforementioned dependence of the reaction rate of explosives on temperature over pressure.

The Simple Pressure-Dependent (SPD) and Simplified Ignition and Growth (SIG) burn models were utilized throughout this research. These models served as points of comparison for the ARCIIST technique and will be explained in greater detail in Chapter V.

2.4 Arrhenius Rate Reactive Chemistry Models

Although hydrocode simulations of explosives have been in development since the late 1970's and early 1980's [54], only recently have chemists developed numerical

models to describe the comprehensive thermal decomposition of common HEs from condensed reactants to gaseous products. Most prominently, Prasad et. al. developed such a model for cyclotrimethylenetrinitramine (RDX) consisting of over 40 chemical species and 231 Arrhenius rate reaction equations [39][50][55]. A model of this magnitude would be rather unwieldy to integrate into a hydrocode. Fortunately, Dr. Igor Schweigert at the NRL developed a methodology to reduce Prasad's model to 7 critical reactions and 11 chemical species [44][45]. This reduced model was a critical component for establishing and testing the ARCIIST technique and will be discussed in detail in Chapter III.

The decomposition rates in Prasad's model, and by extension Schweigert's model, were largely identified through previous accomplished experimental methods. Thus, it should be noted that the accuracy of the RDX Arrhenius rate model is dependent on the temperature and pressure ranges observed during those experiments. Simulations conducted beyond those limitations run the risk of introducing extrapolation errors. In addition to these limitations, the use of a chemistry model in this research which was the result of fitting Arrhenius rate parameters to match experimental data limits the predictive nature of the overall explosive model. Although this consequence was not desirable, the RDX chemistry model still provided a temperature based decomposition model as opposed to the pressure based methods presented in the previous section. More importantly, it provided a means to test the feasibility of the ARCIIST technique.

Furthermore, since the chemistry model is not based on run-to-detonation experiments, it should be more broadly applicable to a wider range of simulations without recalibration. Additionally, Chakraborty et. al. showed that Prasad's model could be extended to create a unified decomposition model for RDX and cyclotetramethylenetetranitramine (HMX) through ab initio Density Functional Theory (DFT)

calculations [12]. It is therefore conceivable that chemistry models for theoretical explosive compounds can be created. It is even more plausible that Arrhenius rate chemistry models can be developed for new mixtures of existing explosive compounds and binders.

There have been some successful efforts to incorporate Arrhenius rate chemistry models in explosive hydrocodes. These simulations, however, were conducted at the meso-scale. At this scale, all gaseous porous regions are modeled distinctly separate from the regions of condensed explosive material [13][20].

2.5 Arrhenius Rate Chemistry Informed Inter-phase Source Terms (ARCIIST) Development

The purpose of this research is to replace the use of empirical burn models with ARCIIST for implementation in multi-phase continuum hydrocodes. The use of Arrhenius rate models is not new to the simulation of reacting flows. Models such as those developed by Gnoffo et. al. [25] have been used extensively in the simulation of flow fields around hypersonic reentry vehicles. These hypersonic simulations, however, only pertain to one phase of matter, namely gas. To date, such complex reacting chemistry models have not been applied to define the inter-phase interactions in macro-scale multi-phase simulations. By choosing to define inter-phase source terms with a finite-rate chemistry model, a more complete simulation of the thermophysics in an explosive event has been created. Thus, the ARCIIST method is a better tool for understanding the complexities of the DDT process compared to the more simplistic burn models.

As previously mentioned, Chakraborty et. al. demonstrated that Arrhenius rate reactions for explosive materials can be developed, at least in part, using theoretical ab initio DFT. By extension, the ARCIIST technique developed in this research

provides an avenue towards simulating the DDT properties for theoretical explosive compounds and mixtures before they are ever created in a laboratory. ARCIIST will not only save time and money from being spent pursuing explosives that do not show potential to meet requirements, but will also improve the safety measures that need to be put into place when creating and testing batches of the new explosive.

III. Computational Methodology

This chapter will examine two computational tools for evaluating explosive materials which form the foundation for the development and testing of ARCIIST. First, the choice of the MPEXS one-dimensional macro-scale finite volume hydrocode as the test bed for this research will be explained. Furthermore, the background information on the modified Baer and Nunziato (BN) governing equations that form the basis for MPEXS will be provided. This information includes a discussion of the inter-phase source terms which are the central object of this research. A description of the Equations of State (EOS) chosen to provide closure to the governing equations is also provided.

Secondly, the NRL's Arrhenius chemistry model for RDX will be examined. On its own, this non-dimensional model can be used to analyze the effects of temperature, pressure and density on the microscopic reactions that transform solid RDX into its gaseous reaction products. When combined with MPEXS through the ARCIIST method, the chemistry model forms the basis for determining the mass exchange rate between the condensed and gaseous phases.

3.1 MPEXS Hydrocode

MPEXS is a macro-scale finite volume hydrocode designed to simulate a mixture of condensed, granular explosive material immersed in reaction product gases in one dimension [15]. This system is acted on by a rigid piston moving at a constant velocity (u_p) which initiates a shock wave through the mixture. The shock wave sets off the chemical decomposition of the condensed explosive which rapidly transitions into its gaseous products in the reaction zone following the shock. The increased pressure from the confined gases strengthens the wave front, eventually forming a detona-

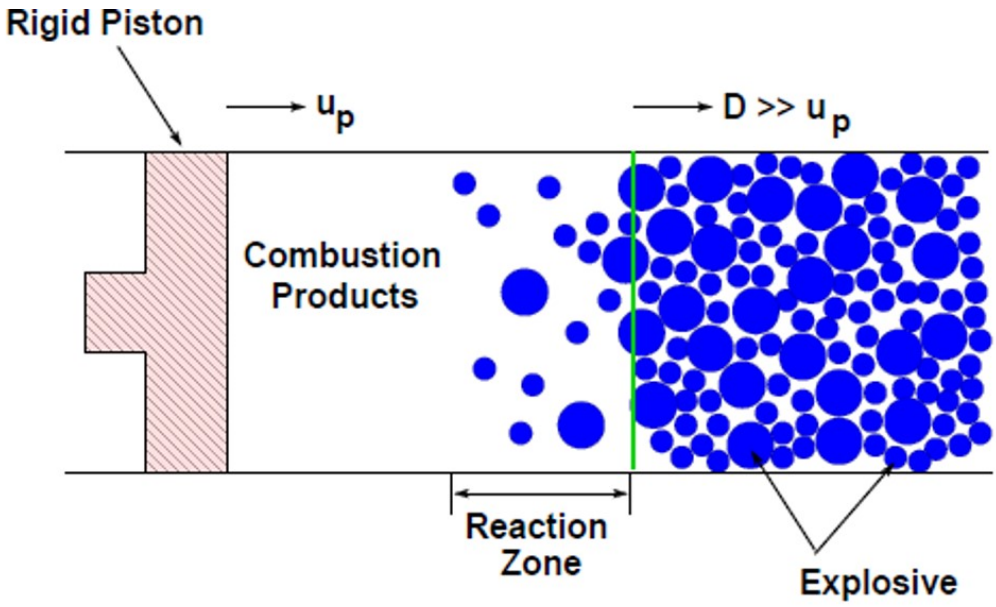

Figure 2. Schematic of piston induced detonation simulated by MPEXS

tion wave traveling through the unreacted explosive material at a steady detonation velocity (D). A graphical depiction of this system is shown in Figure 2.

MPEXS was chosen as the base code for this research for numerous reasons. First, it is a proven research hydrocode with the capability to clearly distinguish between the characteristics of condensed reactant phases and the final gaseous product phase. This capability is a significant advantage over more simplistic mixture-model hydrocodes as will be explained in Section 3.1.1. Secondly, MPEXS was written entirely in FORTRAN, a well-established programing language used extensively in basic research codes. Many other research software tools have FORTRAN interfaces built into them, allowing for great flexibility to easily incorporate new features into MPEXS. Furthermore, although MPEXS currently only has the capacity to distinguish between initial condensed phases and a single final gaseous phase, its modular nature provides the future potential to include intermediate phases. Inclusion of additional intermediate phases will be a natural extension of ARCIIST implementation. Fi-

nally, the MPEXS code is owned and maintained by the Munitions Directorate of the AFRL. The source code was made available in its entirety for use in this research along with direct support from Dr. Michael Crochet, MPEXS's developer.

MPEXS utilizes a Lagrangian reference frame attached to the piston face. Flexibility was built into the hydrocode, allowing the user to prescribe various EOSs, burn models, and other constitutive relationships needed to describe a particular explosive material, metal, or product gases. Once the system is defined, the user selects an initial piston speed, also referred to as initial particle velocity. The piston speed, in turn, establishes the strength of the initial shock wave in the condensed material and begins the shock-induced DDT process.

The following sections will summarize MPEXS's multi-phase model in order to highlight where it will be coupled with NRL's finite Arrhenius rate chemistry model for RDX via ARCIIST.

3.1.1 Single-Phase Mixture Models

Macro-scale continuum hydrocodes for explosives typically fall into one of two categories, single or multi-phase models. The more simplistic hydrocodes employ a single phase mixture model based on the Euler equations in classical fluid dynamics. The governing equations for this model are described by Equations 1–3 [16].

$$\frac{\partial \overline{\rho}}{\partial t} + \frac{\partial}{\partial x}(\overline{\rho}\,\overline{u}) = 0 \tag{1}$$

$$\frac{\partial}{\partial t}(\overline{\rho}\,\overline{u}) + \frac{\partial}{\partial x}\left(\overline{\rho}\,\overline{u^2} + \overline{P}\right) = 0 \tag{2}$$

$$\frac{\partial}{\partial t}\left(\overline{\rho}\,\overline{E}\right) + \frac{\partial}{\partial x}\left[\overline{\rho}\left(\overline{u}\overline{E} + \frac{\overline{u}\overline{P}}{\overline{\rho}}\right)\right] = 0 \tag{3}$$

In these equations x is position, t is time, $\overline{\rho}$ is mixture density, $\overline{u}$ is velocity, $\overline{P}$ is pressure, and $\overline{E}$ is total specific energy. The bar over some variables is used to annotate that they describe the properties of the entire mixture as opposed to an individual gas or condensed phase. This distinction is more important in the next section when discussing multi-phase models. The system is closed by a mixture EOS described in Equation 4.

$$\overline{e} = \overline{e}(\overline{\rho}, \overline{P}) \tag{4}$$

Such single-phase mixture models are severely limited. First, they cannot provide insight into the properties of interest in the individual components of the mixture. Secondly, and more critically, there is a significant challenge in determining an equation of state that can completely model the behavior of the explosive from its initial condensed state through its final gaseous products.

3.1.2 Multi-Phase Models

The MPEXS hydrocode addresses the shortcomings of single-phase mixture models by deriving mass, momentum, and energy equations for each component of the reactant-product mixture being simulated. Dr. Crochet developed MPEXS for the purpose of simulating metalized explosive behavior [15]. To do so, he expanded upon the two phase model developed by Baer and Nunziato to simulate homogeneous explosives [4]. Thus, MPEXS allows for the prescription of multiple condensed phase materials as an initial condition for a simulation. MPEXS only allows the user to prescribe a single component for the gaseous product phase. However, as previously noted, there is potential for this model to be expanded to include multiple intermediate and final product phases. The modified BN governing equations are described in Equations 5–11.

$$\frac{\partial}{\partial t}\left(\phi_i \rho_i\right) + \frac{\partial}{\partial x}\left(\phi_i \rho_i u_i\right) = \mathcal{C}_i \tag{5}$$

$$\frac{\partial}{\partial t}(\phi_g \rho_g) + \frac{\partial}{\partial x}(\phi_g \rho_g u_g) = \mathcal{C}_g \tag{6}$$

$$\frac{\partial}{\partial t}(\phi_i \rho_i u_i) + \frac{\partial}{\partial x}(\phi_i \rho_i u_i^2 + \phi_i P_i) = \mathcal{M}_i \tag{7}$$

$$\frac{\partial}{\partial t}(\phi_g \rho_g u_g) + \frac{\partial}{\partial x}(\phi_g \rho_g u_g^2 + \phi_g P_g) = \mathcal{M}_g \tag{8}$$

$$\frac{\partial}{\partial t}(\phi_i \rho_i E_i) + \frac{\partial}{\partial x}\left[\phi_i \rho_i u_i \left(E_i + \frac{P_i}{\rho_i}\right)\right] = \mathcal{E}_i \tag{9}$$

$$\frac{\partial}{\partial t}(\phi_g \rho_g E_g) + \frac{\partial}{\partial x}\left[\phi_g \rho_g u_g \left(E_g + \frac{P_g}{\rho_g}\right)\right] = \mathcal{E}_g \tag{10}$$

$$\frac{\partial \phi_i}{\partial t} + u_i \frac{\partial \phi_i}{\partial x} = \mathcal{F}_i + \frac{\mathcal{C}_i}{\rho_i} \tag{11}$$

In these equations, ϕ_i is i-th condensed volume fraction, ρ_i is i-th condensed density, u_i is i-th condensed particle velocity, P_i is i-th condensed pressure, and E_i is i-th condensed total specific energy. Other expressed symbols with a subscript i denote parameters of the solid components. Likewise, symbols with the subscript g refer to the properties of the gaseous products. The quantities $\mathcal{C}$, $\mathcal{M}$, and $\mathcal{E}$ are source terms indicating the mass, momentum, and energy exchange between the mixture components. The quantity $\mathcal{F}$ is the compaction source term associated with the inert pore collapse of the granular condensed phases.

This system of equations is closed with an EOS for each mixture component. The

choice of EOSs for this research will be further discussed in Section 3.1.4. Additionally, constraints are imposed on the inter-phase source terms and volume fractions as described in Equations 12–15. These constraints ensure the conservation of mass, momentum, and energy of the entire system is maintained even as the energetic material is transitioning from a condensed state to its gaseous products.

$$\mathcal{C}_g + \sum_{i=1}^{N} \mathcal{C}_i = 0 \tag{12}$$

$$\mathcal{M}_g + \sum_{i=1}^{N} \mathcal{M}_i = 0 \tag{13}$$

$$\mathcal{E}_g + \sum_{i=1}^{N} \mathcal{E}_i = 0 \tag{14}$$

$$\phi_g + \sum_{i=1}^{N} \phi_i = 1 \tag{15}$$

In addition to the constraints above, definitions of mixture properties and mass fractions (λ) are required. These parameters are defined in Equations 16–23. These equations ensure the information on the overall mixtures status cam be obtained through the proportional summation of the parameters from the individual phases. The definitions for mixture density ($\overline{\rho}$), temperature ($\overline{T}$), and pressure ($\overline{P}$) are particularly important for comparisons with experimental data which is not capable of distinguishing between the contributions of particular phases. It should be noted that, through use of Equations 12–23, the single-phase mixture Equations 1–3 can be recovered by summing the mass, momentum and energy equations in MPEXS's multi-phase model [16].

$$\overline{\rho} = \phi_g \rho_g + \sum_{i=1}^{N} \phi_i \rho_i \tag{16}$$

$$\overline{T} = \phi_g T_g + \sum_{i=1}^{N} \phi_i T_i \tag{17}$$

$$\overline{P} = \phi_g P_g + \sum_{i=1}^{N} \phi_i P_i \tag{18}$$

$$\overline{u} = \lambda_g u_g + \sum_{i=1}^{N} \lambda_i u_i \tag{19}$$

$$\overline{u^2} = \lambda_g u_g^2 + \sum_{i=1}^{N} \lambda_i u_i^2 \tag{20}$$

$$\overline{uP} = \lambda_g u_g P_g + \sum_{i=1}^{N} \lambda_i u_i P_i \tag{21}$$

$$\overline{uE} = \lambda_g u_g E_g + \sum_{i=1}^{N} \lambda_i u_i E_i \tag{22}$$

$$\lambda = \frac{\phi \rho}{\overline{\rho}} \tag{23}$$

The focus of this research effort was not to further evaluate the utility of simulating the detonation of multiple condensed phase materials. Rather, it was to develop a technique to describe the bulk rate of reaction of a single condensed phase explosive to its gaseous products based on an Arrhenius rate chemistry model. Thus, to simplify the remaining discussion of MPEXS governing equations, the i subscripts will be replaced with s, referring to a single condensed or "solid" phase. The subscript i will be used again in Section 3.2 to reference a particular chemical species. Although

MPEXS's capacity to simulate multiple condensed phase materials will not be utilized, it should be noted that it has been successfully used for such simulations [15][37]. In doing so, it proved the ability of its numerical integration methods, both temporal and spatial, to handle an arbitrary number of governing equations. That capacity was required to handle the additional equations needed to track the advection of individual chemical species in order to implement ARCIIST. This feature further justified the choice of MPEXS as the test bed for ARCIIST. Discussion on these new governing equations will take place in Section 4.3.

3.1.3 Inter-phase Source Terms

As mentioned in the previous section, $\mathcal{C}$, $\mathcal{M}$, $\mathcal{E}$ and $\mathcal{F}$ are source terms indicating the mass, momentum, and energy exchange between phases and the compaction source term respectively. Properly defining these terms is critical to ensuring that conservation of mass, momentum and energy of the entire system is maintained. The relationships for $\mathcal{M}$, $\mathcal{E}$ and $\mathcal{F}$ used by MPEXS were derived by Bdzil et al. [5] and are described by Equations 24–26.

$$\mathcal{F} = \frac{1}{\mu_{sg}} \phi_s \phi_g (P_s - \beta_s - P_g) \tag{24}$$

$$\mathcal{M} = P_g \frac{\partial \phi_s}{\partial x} + \left[\frac{1}{2}(u_s + u_g) - \alpha_{sg}(u_g - u_s) \right] \mathcal{C} - \delta_{sg}(u_s - u_g) \tag{25}$$

$$\begin{aligned} \mathcal{E} = {} & u_s \mathcal{M} - [c_{sg}(P_s - \beta_s) + (1 - c_{sg}) P_g] \mathcal{F} - \left[\frac{1}{2} \alpha_{sg} (u_s - u_g)^2 + \frac{u_s^2}{2} \right] \mathcal{C} \\ & + \left\{ \xi_{sg} e_s + (1 - \xi_{sg}) \left[e_g + P_g \left(\frac{1}{\rho_g} - \frac{1}{\rho_s} \right) \right] \right\} \mathcal{C} + \alpha_{sg} \delta_{sg} (u_s - u_g)^2 \\ & + \mathcal{H}_{sg}(T_g - T_s) \end{aligned} \tag{26}$$

In these equations, μ_{sg} is the compaction viscosity, δ_{sg} is the drag coefficient, H_{sg} is the heat transfer coefficient, α_{sg} is the drag partitioning function, c_{sg} is the compaction partitioning function, ξ_{sg} is the chemical reaction partitioning function, β_s is the inter-granular stress from particles, T_s is the solid temperature, T_g is the gas temperature. The subscript sg indicates the relaxation process between the condensed and gas phases. These parameters are designed to account for the dissipaton effects of viscosity, stress, and drag on the momentum and energy exchanges between the phases. The need for these partitioning and relaxation parameters stem from the BN model's implicit assignment of all dissipation energies to either the condensed or gas phase [16].

The choices made by Bdzil et al. to express these parameters were obtained from empirical relations identified in various explosives engineering and modeling literature [5]. Since these parameters all describe macroscopic interactions such as drag and stress, they are not directly related to the various chemical reaction rates that could be obtained from an Arrhenious rate chemistry model. Thus, the development of ARCIIST presented in this research did not impact the choice of partitioning and relaxation parameters. The formulation of the source terms described in Equations 24–26 were not modified during the implementation of ARCIIST.

The one inter-phase source term that is not included in Equations 24–26 is $\mathcal{C}$, the mass exchange rate between the condensed and gas phase. This term is used to model the bulk chemical decomposition rate of the condensed explosive to its final products and is determined by the choice of burn model. As such, developing a definition for $\mathcal{C}$ based on a finite Arrhenius rate chemistry model was the primary goal of this research effort. Furthermore, it should be noted that $\mathcal{C}$ is an intricate part of the definitions of the other inter-phase source terms. It should be noted that at the pressures and velocities observed in this research, the value of $\mathcal{C}$ dominates the computation of $\mathcal{M}$

and $\mathcal{E}$. Therefore, deriving $\mathcal{C}$ using ARCIIST directly impacts all of the source terms. Details on the methods to obtain a value of $\mathcal{C}$ from NRL's chemistry model for RDX will be provided in Section 4.3.

3.1.4 Equations of State

The correct choice of EOSs is critical to ensure any simulation of an energetic material is actually representative of the explosive compound the user desires to study. Early in this research, a scoping study [41] [42] was conducted to determine the feasibility of using the finite chemistry model of HMX proposed by Chakraborty et. al. [12]. MPEXS already contains multiple EOSs to describe HMX, two for the condensed phase and two for its gaseous products. Thus, four possible EOS combinations are possible to simulate HMX. The scoping study determined the chemistry model for HMX was too complex for use in the initial development of ARCIIST. It did, however, show that simulations of HMX using MPEXS had the best results using the combination of the Mie-Gruneisen (MG) and Jones-Wilkins-Lee (JWL) EOSs for the condensed and gas phases respectively.

The decision to swap Chakraborty et. al.'s HMX model for NRL's RDX model required defining EOSs for RDX and its products in MPEXS. Given the similarities between RDX and HMX, MG and JWL forms of the EOSs were chosen for RDX. These EOSs described by Equations 27 and 28.

$$P_s = \Gamma \rho_s C_v (T_s - T_o) + f(\rho_s) \tag{27}$$

$$P_g = \mathcal{A}\left(1 - \frac{\omega\rho_g}{R_1}\right) e^{\left(\frac{-R_1}{\rho_g}\right)} + \mathcal{B}\left(1 - \frac{\omega\rho_g}{R_2}\right) e^{\left(\frac{-R_2}{\rho_g}\right)} + \omega\rho_g E_g \tag{28}$$

The MG EOS described by Equation 27 relates the pressure of the condensed phase (P_s) to the condensed phase density (ρ_s) and the difference in current condensed phase temperature (T_s) and the initial temperature (T_o). The first term in Equation 27 includes the Gruneisen coefficient (Γ) and ratio of specific heat (C_v) for non-reacting RDX. The second term is a function relating ρ_s to the initial density of the condensed phase ($\rho_{o,s}$) and includes the Hugoniot constants c_o and s describing non-reacting RDX. The exact form of this function depends on whether on not ρ_s is greater than $\rho_{o,s}$. A more detailed description of the MG EOS can be found in [15].

The JWL EOS is described by Equation 28 and relates the pressure of the gaseous phase (P_g) to the gas specific energy (E_g) and gas density (ρ_g). This EOS was calibrated to match experimental detonation velocity and pressure for RDX through the use of five tunable constants: $\mathcal{A}$, $\mathcal{B}$, R_1, R_2, and ω [2].

The parameters required for these EOSs were obtained from studies conducted by Amar et. al. [2] and Dobratz et. al. [21]. These parameters are presented in Tables 1 and 2. Verification studies conducted on these EOS choices will be discussed in Chapter IV.

Table 1. Mie-Gruneisen EOS Constants for RDX Reactants

Γ	$c_o[km/s]$	s	$\rho_{o,s}[g/cm^3]$	$C_v[J/Kg/K]$
1.29	2.78	1.9	1.799	924

Table 2. JWL EOS Constants for RDX Products

$\mathcal{A}[GPa]$	$\mathcal{B}[GPa]$	R_1	R_2	ω
989.0848	11.11902	5.167	1.0458	0.396143

3.1.5 MPEXS Solution Process

In order to understand how ARCIIST was implemented in MPEXS, it is important to identify the major processes being conducted throughout an MPEXS simulation. Figure 3 is a flow chart of MPEXS's major functions. MPEXS begins by loading all of the initial conditions supplied by the user into their appropriate variables. These initial conditions consist of items such as ambient pressure and temperature, initial densities of the condensed and gaseous phases, initial volume fractions for the phases, and the piston speed.

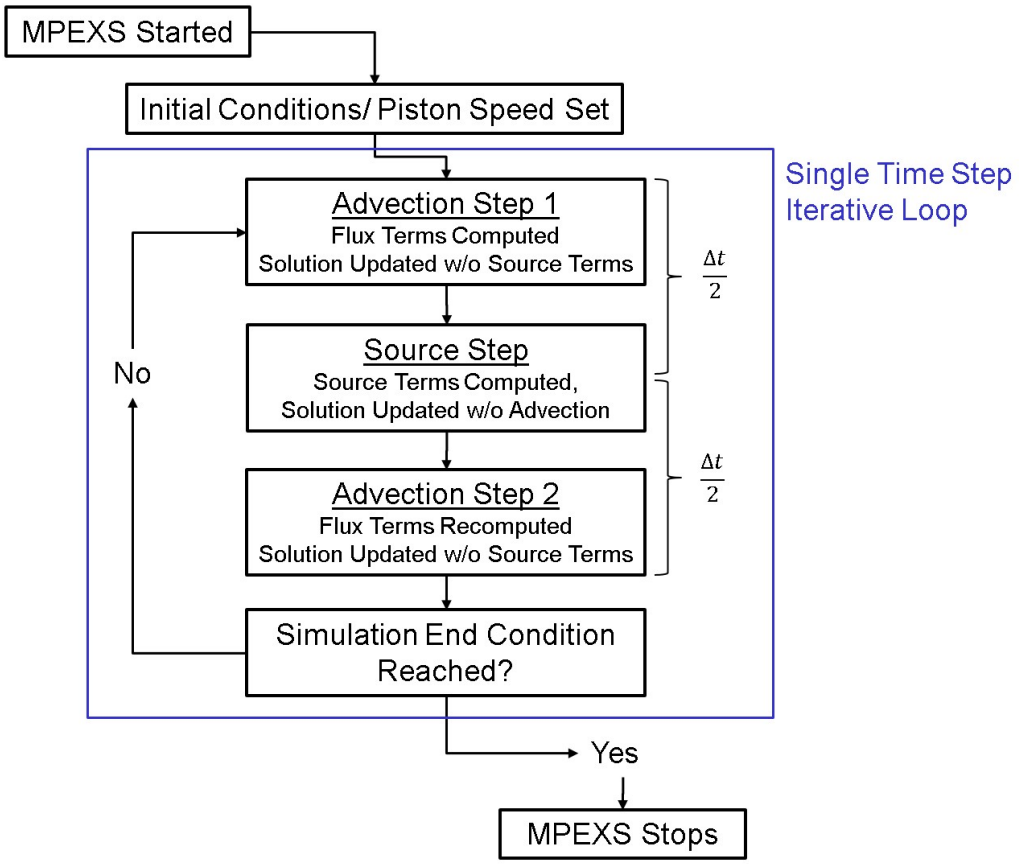

Figure 3. Flow chart of the major processes conducted during an MPEXS simulation

Once the initial conditions are established, MPEXS employs the Strang splitting method [8] [49] to iteratively integrate the solution in time. The components of a single time step iteration are shown within the blue box in Figure 3. The Strang

method consist of three steps, in which the solution from the previous step becomes the initial conditions for the next step. This method is globally second order accurate in time [15].

The first step in the Strang method is an advective step. Here the solution is updated by solving the system of equations from Section 3.1.2 after setting the inter-phase source terms to zero. This step utilizes the Kurganov-Noelle-Petrova (KNP) spacial discretization scheme [32] [33] to extrapolate the solution from the cell centers, compute the fluxes, and update the solution. The KNP scheme is a higher-order accurate central differencing scheme whose accuracy can be varied depending on the polynomial chosen for the solution extrapolation [15]. Per the Strang method, the first advection step uses half of the iteration time step ($\Delta t/2$) for the current iteration when updating the solution.

The second Strang method step is the source step. Using the result of the first step as an initial condition, this step updates the solution again. This time, the source terms are kept and the advective terms are set to zero. Without advection, the system is converted into a set of Ordinary Differential Equations (ODE). Using the open source ODE solver LSODE [40], MPEXS integrates the solution over the full time step (Δt).

The third Strang method step is another advection step. It is same as the first step in the iteration except the initial conditions come from the output of the second step. If the desired simulation end time is reached at the end of the third step, the MPEXS program ends, otherwise the next time step iteration begins.

3.2 Arrhenius Rate Chemistry Model for RDX

As mentioned in Chapter I, Dr. Schweigert from the NRL has developed an Arrhenius rate chemistry model of RDX consisting of 7 reactions and 11 chemical

species [44][45]. The NRL model is a reduction of the model developed by Prasad et. al. [39], itself a combination of Thynell et. al.'s characterization of RDX's condensed phase decomposition [50] and Yetter et. al.'s characterization of the gaseous phase combustion [55]. The list of species used by NRL's RDX model are enumerated in Table 3.

The Arrhenius rate coefficient, k, can be found for each reaction using Equation 29. The 7 reactions in the NRL model, their corresponding preexponential parameters (A and n), and activation energy (E_a) are listed in Table 4.

$$k = AT^n e^{(\frac{-E_a}{RT})} \tag{29}$$

Dr. Schweigert has formatted his RDX model as an input file for Cantera [26], an open source software tool for simulating chemical kinetics and thermodynamics. Cantera maintains a FORTRAN interface. In implementing ARCIIST, MPEXS was modified to call upon Cantera's subroutines through this interface. Properties such as the density, temperature and the mass ratio of each species in each grid cell in MPEXS can be provided as input to Cantera. In this manner, the net rates of production for each species, $\dot{\omega}_i$, are computed using Equations 30–32. As mentioned previously, the subscript i is an index related to the species number in Table 3. The subscript r is an index referring to the reaction number in Table 4. In these equations, $R_{b,r}$ and $R_{f,r}$ refer to the backward and forward reaction rates for reaction r, $\alpha_{i,r}$ and $\beta_{i,r}$ refer to the reactant and product stoichiometric coefficients for species i in reaction r, X_i is the molar ratio of each species, and M_i is the molecular weight of each species.

$$\dot{w}_i = M_i \sum_{r=1}^{N_r} (\beta_{i,r} - \alpha_{i,r}) (R_{f,r} - R_{b,r}) \tag{30}$$

$$R_{f,r} = k_{f,r} \prod_{i=1}^{11} X_i^{\alpha_{i,r}} \tag{31}$$

$$R_{b,r} = k_{b,r} \prod_{i=1}^{11} X_i^{\beta_{i,r}} \tag{32}$$

ARCIIST has been developed such that the phase densities, temperatures, and a vector of species mass ratios (Y_i) computed by MPEXS in each grid cell can be passed to Cantera every iteration. In doing so, a concurrent multi-scale simulation interface has been created. Each grid cell, in essence, becomes a Zero-Dimension (0-D) reactor conducting a Constant Volume Thermal Explosion (CVTEX) simulation based on the macro-scale parameters from MPEXS. The vector of $\dot{\omega}_i$ resulting from these CVTEX simulations can then be used to inform the bulk chemical reaction rate, $\mathcal{C}$. By creating this interface, ARCIIST transforms MPEXS into a concurrent multi-scale simulation tool. The new formulation of $\mathcal{C}$ using ARCIIST will be further discussed in Section 4.2.

Table 3. List of Chemical Species

No.	Species
1	RDX
2	CH_2O
3	N_2O
4	HCN
5	NO_2
6	NO
7	H_2O
8	CO_2
9	CO
10	N_2
11	H_2

Table 4. NRL's RDX Reaction Mechanism

No.	Reaction	$A[s^{-1}]$	n	$E_a[kcal/mol]$
1	$RDX \rightarrow 3CH_2O + 3N_2O$	6.00E+13	0.0	36
2	$RDX \rightarrow 3HCN + \frac{3}{2}NO_2 + \frac{3}{2}NO + \frac{3}{2}H_2O$	2.50E+16	0.0	44
3	$CH_2O + NO_2 \rightarrow NO + H_2O + CO$	2.00E+15	0.0	31
4	$HCN + NO_2 \rightarrow NO + \frac{1}{2}N_2 + \frac{1}{2}H_2 + CO$	0.50E+14	0.0	38
5	$HCN + NO \rightarrow N_2 + \frac{1}{2}H_2 + CO$	1.20E+14	0.0	63
6	$N_2O + CO \rightarrow N_2 + CO_2$	1.00E+18	0.0	140
7	$NO + CO \rightarrow \frac{1}{2}N_2 + CO_2$	1.00E+18	0.0	130

IV. Development of Arrhenius Rate Chemistry Informed Inter-phase Source Terms (ARCIIST)

The purpose for creating the ARCIIST method is to base the inter-phase source terms on more fundamental principles of physics and chemistry. Until now, macro-scale continuum simulations of explosive material have relied predominantly on empirically based burn models to govern the rate of mass exchange between the condensed and gaseous phases. This chapter will discuss in detail how ARCIIST can be used to garner the mass exchange rate from Arrhenius rate chemistry models instead. Furthermore, it will discuss the derivation of new governing equations required to implement ARCIIST into MPEXS. Although the ARCIIST technique can conceivably be utilized in numerous hydrocodes with any Arrhenius rate chemistry model, the methods in this chapter are developed in the context of connecting the NRL chemistry model of RDX to MPEXS.

4.1 Chemical Species Allocation

The interface between MPEXS and NRL's RDX chemistry model through ARCIIST makes it possible to obtain the net mass production rate, $\dot{\omega}_i$, for each of the 11 chemical species in the model. In order to implement ARCIIST, MPEXS was modified to track the mass ratios of each chemical species as additional conserved variables. While the chemistry model distinguishes between reactant, intermediate, and product species, MPEXS can only distinguish between condensed and gaseous phase material. As mentioned in Chapter III, all parameters in the BN model must be assigned to either the condensed or gaseous phase [16]. Since MPEXS is based on the BN model, each chemical species had to be defined as falling into into either the condensed or gaseous category.

In Section 3.2, it was stated that the NRL chemistry model was a simplification

and combination of two larger characterizations of the condensed and gaseous phase reaction mechanisms. Looking again at Table 4, the first two reactions were derived from Thynell et. al.'s study on the condensed phase of RDX [50]. The remaining five reactions were derived from Yetter et. al's work characterizing the reactions in the gaseous products of RDX [55]. From this, six of the species can be easily classified. Intuitively, the species RDX only appears as a reactant in the first two reaction equations in Table 4. Clearly, RDX must be classified as part of the condensed phase. Similarly, in all seven reactions, the species H_2O, CO_2, CO, N_2, and H_2 only appear as products. These five species, therefore, must be classified as part of the gaseous phase.

Dividing the remaining intermediate species into either the condensed or gaseous phase is much more arbitrary. These decisions should largely be based on the features of the chemistry model being integrated into the macro-scale hydrocode. The most logical place to start is to analyze where each reaction in the chemistry model came from. As previously mentioned the NRL model for RDX, the first two reactions in Table 4 came from studies focused on the condense phase. This makes CH_2O, N_2O, HCN, NO_2, and NO candidates for being included in the condensed phase. It should be noted that CH_2O in particular stands out from the rest. Unlike most of the other species, it only appears in two reactions. The first appearance of CH_2O is as a product of the first RDX decomposition mode which occurs early in the reaction sequence when the temperature of the system is lower. It then appears as a reactant in reaction 3, the first reaction that does not involve RDX. Thus, by assigning CH_2O to the condensed phase with RDX, a clear separation point between the two phases can be made between reactions 3 and 4. The final allocation of the chemical species used in this research is depicted in Figure 4.

The species allocation was verified by conducting a 0-D CVTEX simulation of

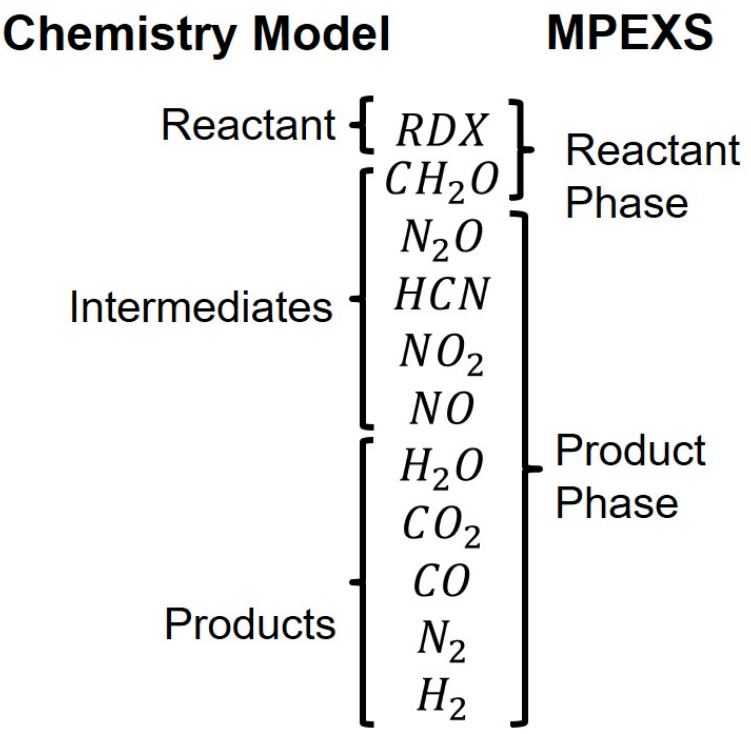

Figure 4. Diagram of species classification across the interface between NRL's chemistry model and MPEXS

RDX. A simple reactor was created in Cantera using the NRL chemistry model as input. A mixture temperature ($\overline{T_o}$) of 900 K and mixture density ($\overline{\rho_o}$) of 1.8 g/cm^3 [14] were used as initial conditions. The mixture initially contained only RDX such that the mass ratio (Y_i) of RDX was 1. Y_i for all other species was set to 0. The evolution of the mass fractions of each species over time is shown in Figures 5 - 7. Each of these figures is also overlaid with the temperature profile of the system throughout the simulation. These overlays allow for the identification of key transition points in the decomposition of RDX.

Figure 5 shows the progression of the mass ratios for the three chemical species designated as part of the condensed phase. By the time the temperature in the system has increased to approximately 1200 K, all of the RDX and CH_2O has been depleted. Referring again to Table 4, one can conclude that reactions 1 - 3 are completed at

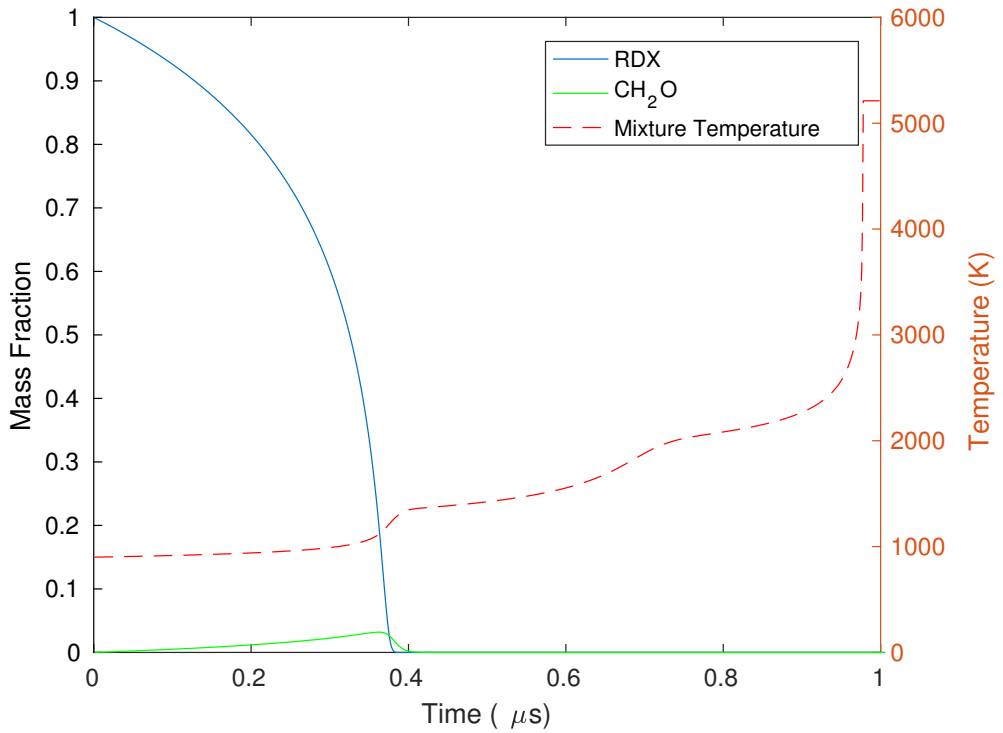

Figure 5. 0D CVTEX simulation of RDX with initial conditions $\overline{T}_o = 900\ K$ and $\overline{\rho}_o = 1.8\ g/cm^3$: mass fraction evolution of RDX and condensed phase intermediate species CH_2O (left axis); mixture temperature profile (right axis).

approximately the same time. It appears that 1200 K is a transition point at which the condensed phase reactions have completed and the gaseous phase reactions take off. It also closely correlates with the fizz zone observed in the experiments conducted by Prasad et. al. on RDX propellants [39]. This fizz zone exists at the interface between the condensed liquid RDX propellant and gaseous products, and marks the transition point between the two phases. This fizz zone was seen to begin around 478 K (the melting point of RDX) and 1500 K. Thus, it is reasonable to assume that all condensed phase material should be completely transformed into gaseous phase species by the time the system reaches 1500 K. These observation lends validity to the decision to put CH_2O in with RDX in the condensed phase.

It should also be noted that as the temperature in the CVTEX simulation ap-

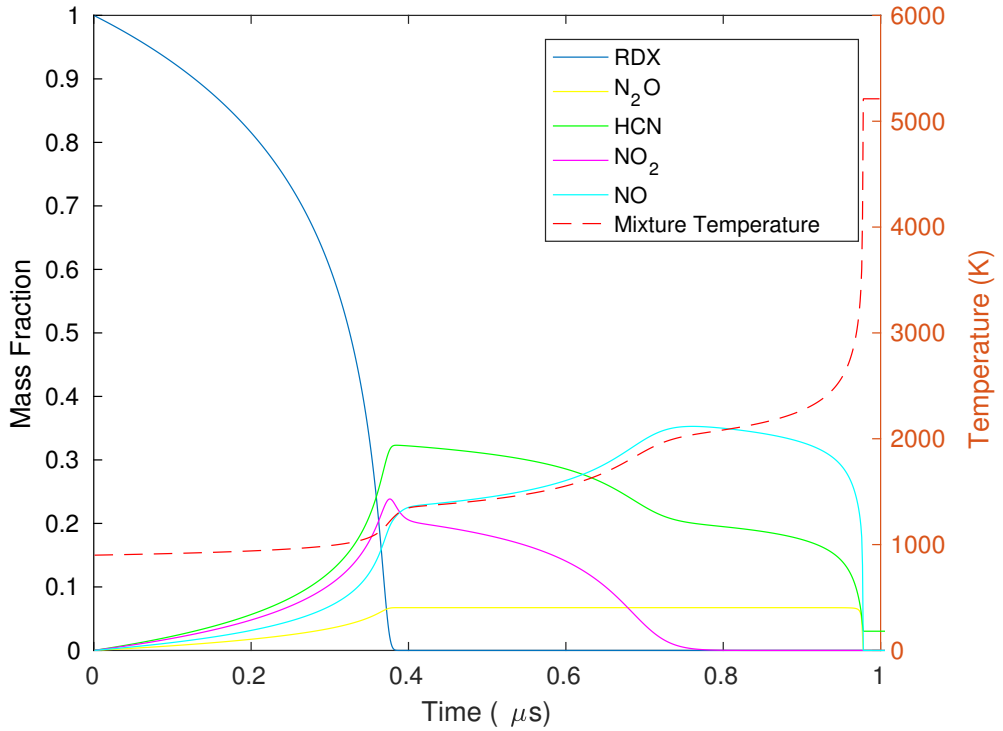

Figure 6. 0D CVTEX simulation of RDX with initial conditions $\overline{T}_o = 900\ K$ and $\overline{\rho}_o = 1.8\ g/cm^3$: mass fraction evolution of RDX and gaseous phase intermediate species N_2O, HCN, NO_2, and NO (left axis); mixture temperature profile (right axis).

proached 1200 K, the destruction rate of RDX and CH_2O grows exponentially. These destruction rates have consequences in the way $\mathcal{C}$ is computed and will be discussed in Section 4.2.

Figures 6 and 7 show the mass ratio progression of the gaseous intermediate and final gaseous products respectively. In both figures, the mass ratio of RDX was also plotted as a reference to show approximately where the condensed phase reactions were completed and how quickly those reactions were occurring. As expected from an examination of Table 4, all of the HCN is produced in reaction 2. Figure 6 shows that HCN begins to disappear when the system gets above 1200 K, indicating the onset of reactions 4 and 5. All of the HCN is depleted by the time the system reaches 2000 K. Coincidently, this is also the point at which NO stops being produced and

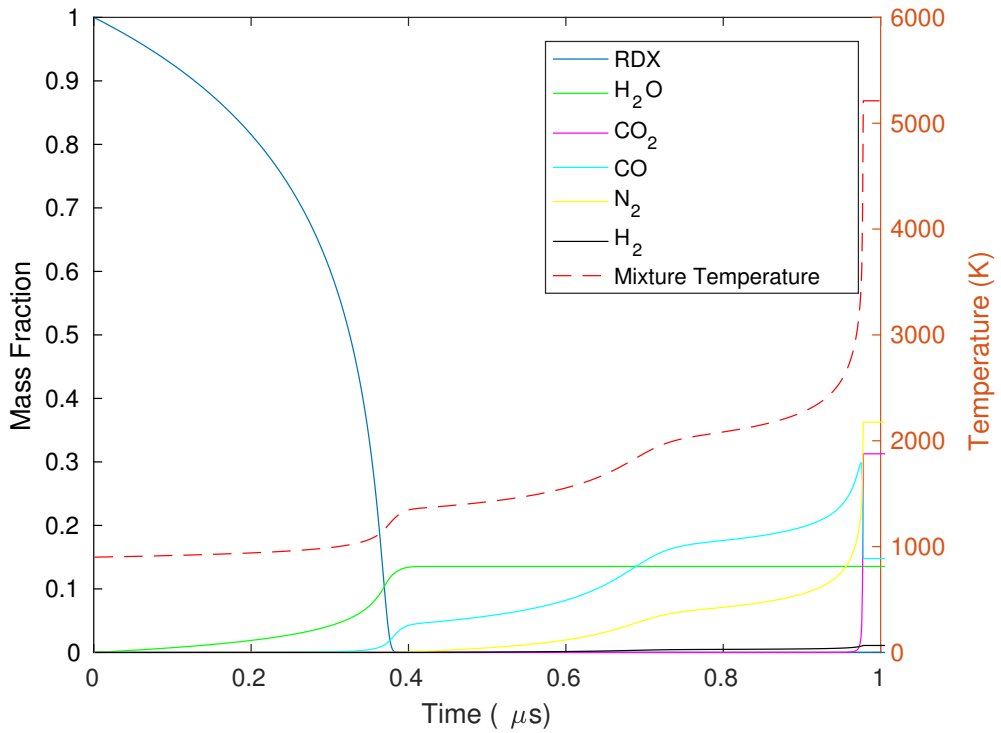

Figure 7. 0D CVTEX simulation of RDX with initial conditions $\overline{T}_o = 900\ K$ and $\overline{\rho}_o = 1.8\ g/cm^3$: mass fraction evolution of RDX and final gaseous phase products H_2O, CO_2, CO, N_2 and H_2 (left axis); mixture temperature profile (right axis).

starts to be utilized more rapidly as a reactant, indicating the onset of reaction 7. In Figure 7, the onset of reaction 6 and the acceleration of reaction 7 can be observed in the production rate of CO_2 as the system rises above 2200 K. All reactions are completed shortly thereafter leaving nothing but the final products H_2O, CO_2, CO, N_2, and H_2. Figures 6 and 7 clearly show that reactions 4 - 7 all begin after the system reaches 1200 K, further reinforcing the choices made in allocating the species between the condensed and gaseous phases.

It should be noted that the process of allocating species between the phases would have to be redone if the ARCIIST technique were to be used with any Arrhenius rate model other than the NRL model. Although the CVTEX simulation conducted and the observations of Prasad et al. [39] helped verify the choices made in Figure 4,

the allocation of species was arbitrary. It is conceivable that the brackets in Figure 4 could be adjusted such that any number of intermediate species could be included in either the condensed reactant or gaseous product phase. Doing so could increase or decrease the impact of certain reactions on determining the inter-phase source terms. Ideally, a third intermediate phase should be added to MPEXS. However, it is ambiguous what EOS should be used to define an intermediate phase. In fact, the development of EOSs for energetic materials is a full area of research itself [56]. Thus, this research is focused on proving the merits of the ARCIIST technique within the constraints of a two phase model. Incorporating an intermediate phase would be a logical extension of this research.

4.2 Defining the Inter-Phase Source Terms

With the chemical species divided between condensed and gas phases, it is now possible to define the new mass rate exchange, $\mathcal{C}$. The purpose of $\mathcal{C}$ in MPEXS is to govern the bulk chemical reaction rate, determining how much mass is transformed from condensed to gaseous material. This term balances Equations 5 and 6 so that mass is conserved between the two phases. Since MPEXS uses a finite volume integration method and since the spatial discretization remains constant in the simulation, each cell in the computational domain can be considered a constant volume. Properties such as temperature, density, and the mass ratios of the chemical species present in that cell can be used as input to the NRL chemistry model to determine the net production rate ($\dot{w}_i$) of each species. Given that $\dot{w}_i$ is the mass exchange rate of each individual species, computing $\mathcal{C}$ becomes a simple matter of adding the net production rates of the condensed phase species.

This relationship, defined in Equation 33, is the main component of ARCIIST and therefore is the primary focus of this research. In this equation, N_s refers to the

number of species in the condensed phase.

$$\mathcal{C} = \sum_{i=1}^{N_s} \dot{w}_i \tag{33}$$

As discussed in Section 3.1.3, the formulation for the other source terms, $\mathcal{M}$, $\mathcal{E}$ and $\mathcal{F}$, are not directly impacted by any parameters that can be calculated using the NRL chemistry model. All three source terms, however, largely rely on the value calculated for $\mathcal{C}$. Thus, using the NRL model to compute the mass exchange rate via ARCIIST also impacts the value of the momentum, energy, and compaction source terms as well.

4.3 ARCIIST Implementation in MPEXS

Since the main goal of ARCIIST is to compute a mass exchange rate ($\mathcal{C}$) based on an Arrhenius rate model, the majority of the implementation took place within the Source Step of MPEXS as shown in Figure 3. This section will expand upon the subprocesses in the Source Step to explain how Cantera, the NRL chemistry model, and Equation 33 come together to form the core of the ARCIIST technique.

During the course of this research, two methods for implementing ARCIIST were devised. Figure 8 outlines the subprocess within the Source Step when ARCIIST Implementation Method 1 is used. As previously mentioned, the primary goal of ARCIIST is the computation of $\mathcal{C}$. Method 1 accomplishes this by using the mixture temperature ($\overline{T}$), mixture density ($\overline{\rho}$), and an array of chemical species mass ratios ($[Y_i]$) as input to the Cantera subroutines. These subroutines then use the Arrhenius rate information from the NRL chemistry model to compute the net production rate of each species ($[\dot{w}_i]$). With this new information, it is then possible to compute $\mathcal{C}$ via Equation 33. From there, the source terms $\mathcal{M}$, $\mathcal{E}$, and $\mathcal{F}$ are computed for each cell via Equations 24–26 using the original MPEXS processes. Finally, LSODE is called

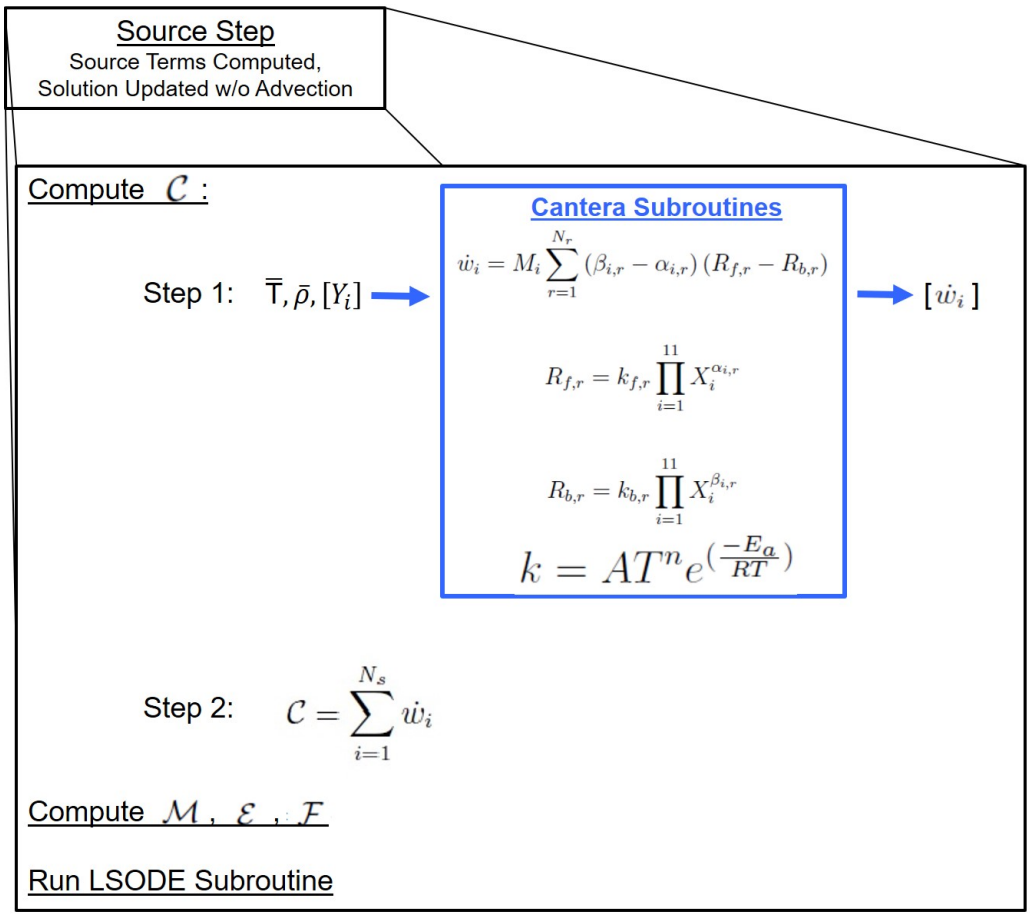

Figure 8. ARCIIST Implementation Method 1: mixture temperature and density used as input to Arrhenius rate computations

to update the solution for each cell and conclude the Source Step.

Since the BN equations on which MPEXS is built on are ultimately designed to simulate fluid mixtures, ARCIIST Implementation Method 1 would appear to be a logical choice. However, Method 1 can be severely limited in its application depending on the Arrhenius rate chemistry model being used. The NRL chemistry model of RDX used in this research created limitations that had to be addressed for any simulation to be successful.

Early studies were conducted during this research to determine the feasibility of the ARCIIST technique using a form of Implementation Method 1 [41] [43]. These studies were conducted before a method for tracking the mass ratios of each species in

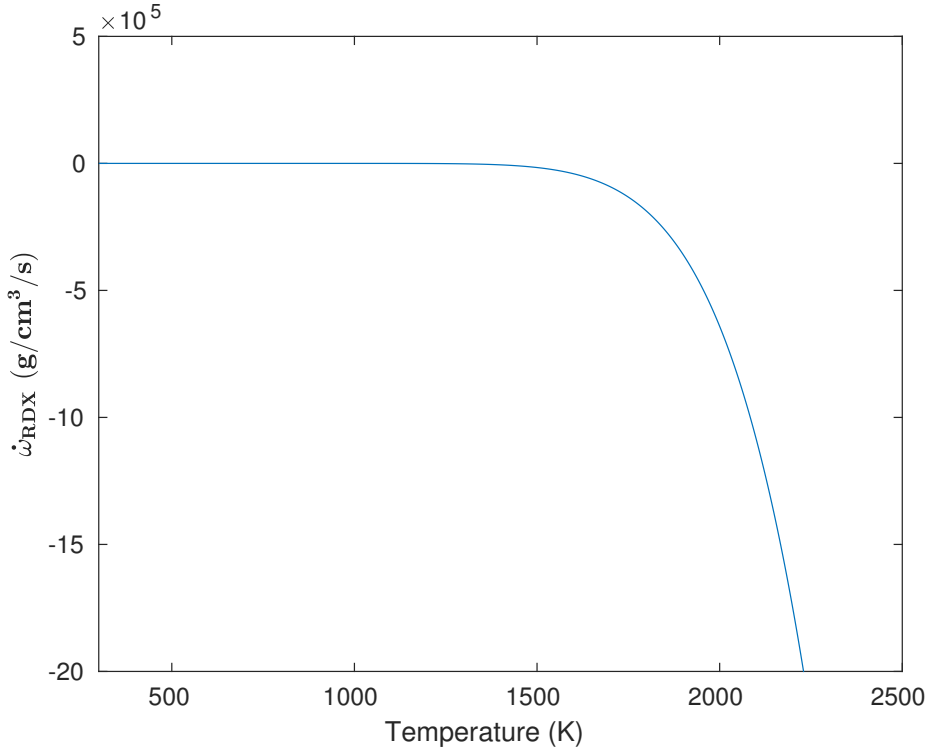

Figure 9. Maximum destruction rate of RDX as a funtion of temperature

the system had been developed and implemented. Because of this, RDX was the only species allocated to the condensed phase and $\mathcal{C}$ was based entirely on the destruction rate of RDX. Furthermore, each time the Cantera subroutines were called the mass ratio of RDX was set to 1 while Y_i for all other species was set to 0. This choice resulted in maximizing $\dot{\omega}_{RDX}$ for a given temperature and density. Furthermore, it removed the requirement to know the mass ratio of each species to determine $\mathcal{C}$.

It was found in these early studies that $\dot{\omega}_{RDX}$ in the NRL model grew exponentially with temperature, quickly reaching an asymptotic limit as $\overline{T}$ rose above 1200 K. This trend of RDX's destruction rate towards infinity as temperature increases can be clearly seen in Figure 9. It should also be noted that, due to numerical restrictions within MPEXS, ϕ_s reduces to nearly zero, but can never actually reach zero during the course of a simulation. The combination of a very large $\mathcal{C}$ occurring at the same

time that ϕ_s was extremely small resulted in numerical instabilities which would cause the simulation to crash before completion. This problem was solved in those early studies by capping the mixture temperature sent to the Cantera subroutines at 1200 K, effectively capping $\mathcal{C}$. The temperature cap of 1200 K is not unreasonable, especially considering that experimental thermogravimetric analysis shows RDX reaching a maximum decomposition rate at approximately 500 K [21] [23].

Even after the mass fraction tracking of individual chemical species was solved and CH_2O was added to condensed phase, the destruction rate of RDX still dominated the computation of $\mathcal{C}$. This condition resulted in the requirement that the temperature cap must be kept to maintain numerical stability. The temperature cap, however, also created an unfortunate side effect. As shown in Figures 6 and 7 in the CVTEX study from Section 4.1, most of the later reactions in the NRL chemistry model do not initiate until the system is well above 1200 K. The inclusion of the later reactions is not necessary to accurately compute $\mathcal{C}$ and get macro-scale properties from the system. However, this restriction limits the ability to use the NRL chemistry model within MPEXS to its full potential. Without triggering the later reaction, the user would not be able to gain accurate information on the formation of species over time and space throughout the simulation.

ARCIIST Implementation Method 2 was developed to keep the stability gained from the temperature cap on the condensed phase reactions while still allowing the NRL model to progress through all of the gaseous phase reactions. A depiction of the steps involved to compute $\mathcal{C}$ using Method 2 is shown in Figure 10.

Implementation Method 2 breaks down the process of computing $\mathcal{C}$ between the two phases. In Step 1, the condensed phase properties of temperature (T_s) and density (ρ_s) are used as input to the Cantera subroutines along with the mass ratios for the condensed phase species (Y_1 and Y_2). Since reaction 3 was determined to be part of

the condensed phase reactions, the mass ratio for NO_2 (Y_5) is also included as an input to Cantera in Step 1. This ensures that reaction 3 has information on both of its reactants and can be computed properly. The condensed phase temperature (T_s) is capped at 1200 K to prevent the destruction rate of RDX from creating numerical instabilities. By only providing Y_i for RDX, CH_2O, and NO_2, Method 2 ensures Cantera is only using the first three reactions in the NRL model, which coincidently are the reactions primarily associated with the condensed phase. The result is an array of ω_i for all chemical species resulting from the first three reactions.

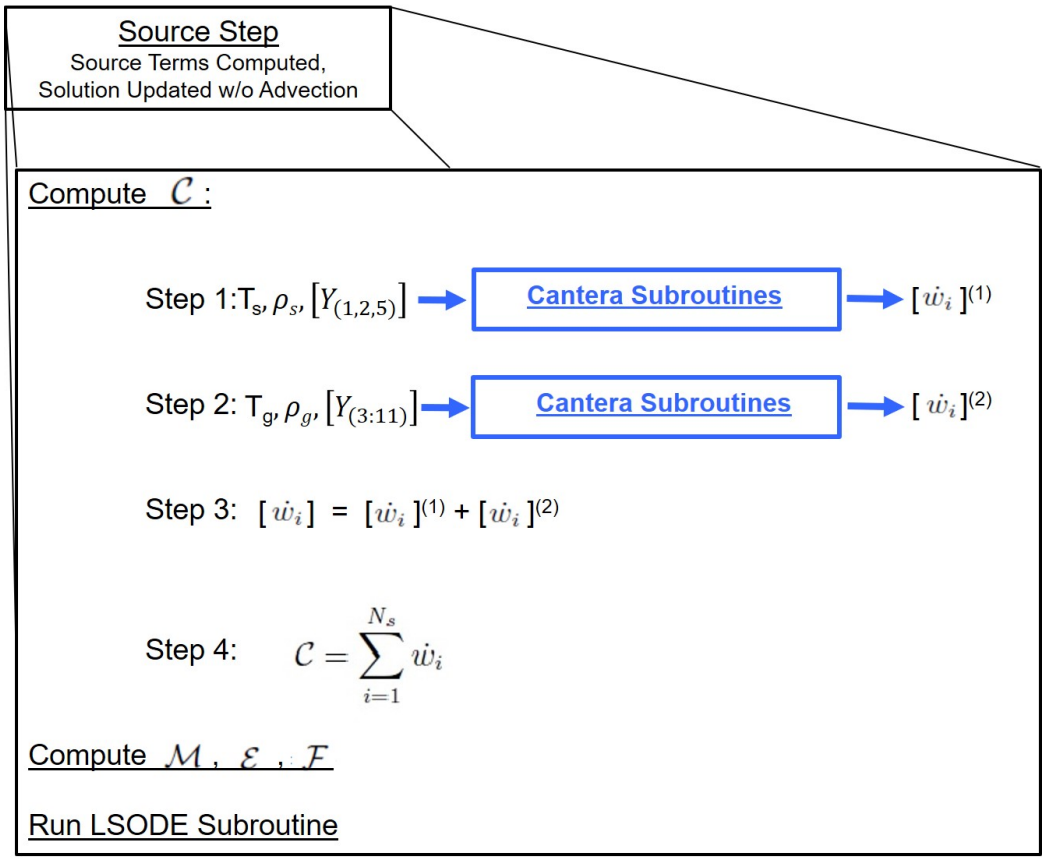

Figure 10. ARCIIST Implementation Method 2: temperature and density properties from the condensed and gaseous phases used as input to Arrhenius rate computations separately

In a similar fashion, Step 2 computes an array of ω_i for all chemical species resulting from the gaseous phase reactions. This time, the gaseous phase properties

of temperature (T_g) and density (ρ_g) are used as input to the Cantera subroutines. An array of mass ratios for all gaseous phase species ($Y_{(3:11)}$ is also required as an input for this step. T_g is not capped, ensuring that all gaseous phase reactions may be initiated and run to completion.

It should be noted that the use of the NO_2 mass ratio in both the condensed and gaseous phase is limited to the reaction computations within Cantera and does not directly factor into the macro-scale computations within MPEXS. While this does create a slight double counting of NO_2 within the Cantera subroutines, it did not appear to have much impact on the macro-scale results. These results will be discussed in greater detail in Chapter VI.

Step 3 sums the resultant ω_i arrays from the first two steps to get the total net production rates of each species for the current time step. Finally, $\mathcal{C}$ is again computed via Equation 33 using the summed array from Step 3.

The concept of splitting properties, particularly temperature, in order to model the chemical reactions within energetic materials is not unprecedented. Tringe et. al. successfully modeled thermal detonation of LX-10 and PBX 9501 using Arbitrary-Lagrangian-Eulerian Three Dimentional Finite Element Code (ALE3D) with a Multi-Phase Convective Burn Model (MCBM). Within the initiation zone of their simulation, the gas phase was initialized at 3900 K while the condensed phase was set to 750 K [51].

Arguably, Method 1 presents a simpler and more physically correct model. However, the necessity to cap the destruction rate of RDX makes Method 1 implausible for this research. This shortfall of the NRL model has been addressed with Dr. Schweigart. It was suggested that converting the model to an extended Arrhenius rate format could provide a solution. In this format, a maximum net production rate is built into the model, thus preventing the need to artificially cap the rate by limit-

ing the temperature input to Cantera. Unfortunately, a new RDX model using the extended Arrhenius rate format was not developed during the course of this research and must be left for future efforts to improve the ARCIIST technique.

4.4 Derivation of Species Mass Fraction Advection Equations

As mentioned in Section 4.3, a vector of Y_i's is required as an input into Cantera. This vector is a critical item towards obtaining the $\dot{\omega}_i$'s required for ARCIIST implementation. MPEXS originally had no means of tracking and advecting the mass fractions of each chemical species. Thus, additional governing equations were required in addition to Equations 5–11.

To ensure the mass of the system is conserved, the mass of each individual species present in a cell must be conserved. Therefore, these new governing equations will take on the general form described by Equation 34. However, the implementation of ARCIIST relies on the mass fraction of each chemical species, not their individual densities. By using the definition of mass fraction in Equation 35, Equation 34 can be converted into a more useful form shown in Equation 36.

$$\frac{D\rho_i}{Dt} = \dot{w}_i \tag{34}$$

$$\rho_i = \overline{\rho} Y_i \tag{35}$$

$$\frac{D(\overline{\rho} Y_i)}{Dt} = \dot{w}_i \tag{36}$$

It should be noted that Cantera defines Y_i slightly differently than MPEXS. Cantera's definition is shown in Equation 37. In this equation m_i and $\overline{m}$ are the mass of the ith species and total mixture mass in a constant volume respectively. MPEXS's

definition is shown in Equation 38. It is possible to derive the definition of mass fraction used by MPEXS starting from Cantera's definition as shown in Equation 39.

$$Y_i = \frac{m_i}{\overline{m}} \tag{37}$$

$$Y_i = \frac{\phi_i \rho_i}{\overline{\rho}} \tag{38}$$

$$Y_i = \frac{m_i/V}{m/V} = \frac{(m_i/V_i)(V_i/V)}{m/V} = \frac{\phi_i \rho_i}{\overline{\rho}} \tag{39}$$

Within MPEXS, the mass fractions of the condensed and gas phases (λ_s and λ_g) are defined by Equations 40–41.

$$\lambda_s = \frac{\phi_s \rho_s}{\phi_s \rho_s + (1 - \phi_s)\rho_g} = \frac{\phi_s \rho_s}{\overline{\rho}} \tag{40}$$

$$\lambda_g = 1 - \lambda_s \tag{41}$$

Since each species is allocated to either the condensed or gas phase, it is possible to derive dependencies between the mass fractions of the individual species and the mass fractions of the phases. These relationships are shown in Equations 42–43. Here N_s and N_g refer to the number of species in the condensed and gas phases respectively.

$$\sum_{i=1}^{N_\mathrm{s}} Y_i = \lambda_s \tag{42}$$

$$\sum_{i=N_\mathrm{s}+1}^{N_\mathrm{s}+N_\mathrm{g}} Y_i = \lambda_g. \tag{43}$$

The expressions in Equations 42–43 eliminate the need to include an additional

advection equation for Y_i for every species in the chemistry model. Instead, the system of equations that needs to be added to MPEXS's original multiphase model are described in Equations 44–47. It should be noted that this is consistent with the system of equations used by Gnoffo et. al. and Blazek in single-phase reacting hypersonic flow simulations [25] [7].

$$\frac{D(\overline{\rho}Y_i)}{Dt} = \dot{w}_i, \quad i = 1 \; to \; N_s - 1 \tag{44}$$

$$Y_{N_s} = \lambda_s - \sum_{i=1}^{N_s-1} Y_i \tag{45}$$

$$\frac{D(\overline{\rho}Y_i)}{Dt} = \dot{w}_i, \quad i = N_s + 1 \; to \; N_s + N_g - 1 \tag{46}$$

$$Y_{N_s+N_g} = \lambda_g - \sum_{i=N_s+1}^{N_s+N_g-1} Y_i \tag{47}$$

By expanding Equations 44 and 46, the expressions in Equations 48 and 49 are obtained.

$$\frac{D(\overline{\rho}Y_i)}{Dt} = \frac{\partial(\overline{\rho}Y_i)}{\partial t} + u_s \frac{\partial(\overline{\rho}Y_i)}{\partial x} = \dot{w}_i, \quad i = 1 \; to \; N_s - 1 \tag{48}$$

$$\frac{D(\overline{\rho}Y_i)}{Dt} = \frac{\partial(\overline{\rho}Y_i)}{\partial t} + u_g \frac{\partial(\overline{\rho}Y_i)}{\partial x} = \dot{w}_i, \quad i = N_s + 1 \; to \; N_s + N_g - 1 \tag{49}$$

The addition of Equations 48 and 49 to MPEXS completed the changes required to interface MPEXS's macro-scale multiphase model with a finite Arrhenius rate chemistry model, forming a concurrent multi-scale explosive hydrocode.

V. Simulation Parameters and Test Setup

Before full testing of the new ARCIIST technique could be conducted, a substantial amount of preliminary simulations had to be conducted to ensure the major parameters chosen for the simulation were appropriate. This necessity primarily stemmed from the fact that MPEXS had never been used to simulate RDX before. As mentioned in Chapter III, MPEXS already had the JWL and MG EOSs programmed in. Although the coefficients required to represent RDX for those EOSs were well established, some initial testing was conducted to validate that they worked appropriately within the MPEXS system. These tests will be discussed in Section 5.1. Similarly, the two traditional burn models chosen as a basis for comparison were also preprogrammed into MPEXS. Neither, however, had been calibrated to compute the bulk chemical reaction rate of RDX. Section 5.2 provides a detailed description of the two burn models as well as the simulations conducted to ensure they were calibrated appropriately for this research.

With any numerical simulation, the amount of spatial and temporal discretization used is critical to the accuracy of the results. A full refinement study was conducted to ensure the grid spacing and time step size were set appropriately while using ARCIIST. Additionally, since the two traditional burn models had not been used within MPEXS to simulate RDX, a full refinement study was conducted on them as well. The results of these studies are discussed in Section 5.3.

The final section in this chapter discusses the testing plan for ARCIIST. This section establishes the test matrix of MPEXS simulation conducted with both ARCIIST as well as the two traditional burn models. Furthermore, it discusses the experimental data that was also used as a source of comparison to the ARCIIST results.

5.1 Equation of State Validation

As mentioned in Section 3.1.4, when the choice was made to base ARCIIST on RDX instead of HMX, new EOSs for the condensed reactant and gaseous product phases for RDX needed to be added as options into MPEXS. An initial validation study of the RDX EOSs was conducted in [41] and [43], in which MPEXS was run utilizing the Simple Pressure-Dependent (SPD) burn model developed by Schwendeman [46]. Although these studies showed evidence that EOS parameters chosen correctly modeled RDX, SPD was found to be an unreliable burn model for the piston speeds used in this research. The reliability of SPD will be further discussed in Section 5.2 and Chapter VI. To ensure the fault was with the burn model and not the EOSs, the validation study was reaccomplished using the Simplified Ignition and Growth (SIG) burn model developed by Stewart, Yoo, and Wescott [48].

The simulations for the new EOS validation study were conducted concurrently with those used for the burn model calibration study and the spatial and temporal refinement study discussed in Sections 5.2 and 5.3 respectively. The results presented here were found using the optimal refinement levels from those studies. For these one-dimensional simulations using SIG, the domain was discretized into 400 cells per mm and a Courant-Friedrichs-Lewy (CFL) condition of 1.0 were used. The initial conditions for these simulations are listed in Table 5. The initial pressure, temperature, and piston speed (u_p) are identical in both the condensed and gaseous phases at the start of the simulation, thus the subscripts for these parameters have been left off. Four simulations were conducted, each with a different piston speed.

Table 5. Initial Conditions for RDX EOS Validation Simulations

ρ_s $[g/cm^3]$	ϕ_s	$\overline{\rho}$ $[g/cm^3]$	P $[GPa]$	T $[K]$	u_p $[km/s]$
1.8	0.9	1.6	1.013E-4	300	0.5, 0.75, 1.0, 1.5

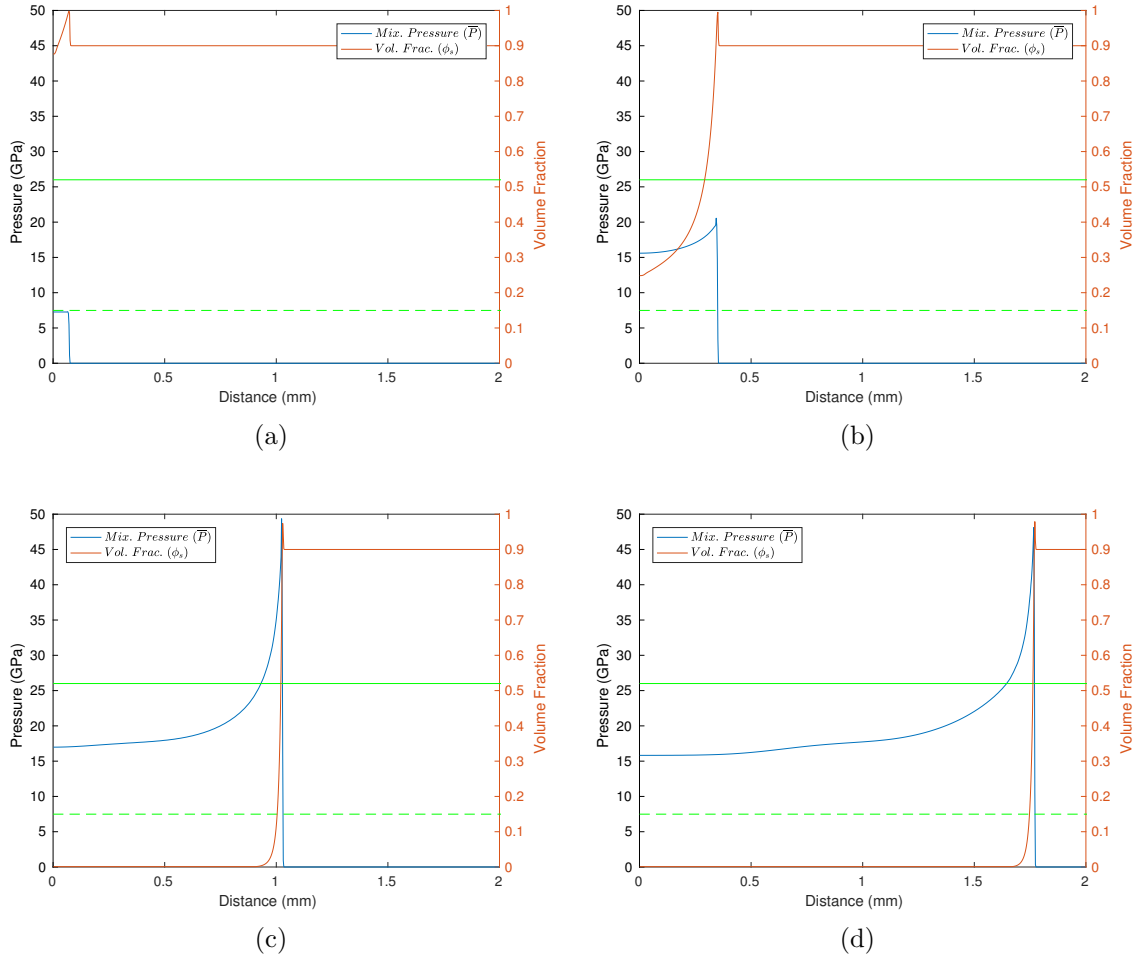

Figure 11. RDX mixture pressure ($\overline{P}$) and condensed phase volume fraction (ϕ_s) profiles using the SIG burn model and 1 km/s piston at (a) 0.025, (b) 0.1, (c) 0.2, and (d) 0.3 μs. The dashed green line (- - -) represents expected response from the non-reacting RDX Hugoniot and the solid green line (—) represents RDX CJ pressure.

Figure 11 shows the evolution of the pressure and volume fraction profiles for the simulation run with a 1 km/s piston speed. The solid green line (—) in these figures represents the P_{CJ} for RDX with an initial density of 1.6 g/cm^3. The dashed green line (- - -) shows the expected post-shock pressure from analysis of the non-reacting RDX Hugoniot [14]. Since MPEXS uses a piston attached reference frame, the distances in this figure represent the position in front of the piston at a snapshot in time.

Subfigure 11a shows that early in the simulation (0.025 μs), the chemical reaction has not yet taken off and the pressure response overall is very close to the non-reacting Hugoniot lines. This subfigure suggests that the parameters chosen for the Mie-Gruneisen EOS are valid. As time progresses, the other Subfigures 11b through 11d show the pressure at the wave front building towards and eventually surpassing P_{CJ}.

In final frames, the leading shock front has stabilized. As expected, the pressure at the shock front jumps up past P_{CJ}, capturing the magnitude of the Von Neumann spike. Behind the front pressure rapidly relaxes down through P_{CJ} at the point where the volume fraction of condensed RDX is approximately zero; the end of the reaction zone. This observation suggests that the parameters chosen for the JWL EOS are also behaving properly.

The results from the 0.5, 0.75, and 1.5 km/s piston simulations can be found in Appendix A. The same trends observed in the 1.0 km/s simulation above are also seen in these three runs as well. The major differences between the runs consist of the early, non-reacting pressure response and the time and distance it takes for a steady state detonation to be reached. As anticipated, the initial pressure response is proportional to the piston speed while the time to reach steady state is inversely proportional. These observations further cement the validity of the EOS parameters chosen to represent RDX in this research.

5.2 Comparison Burn Model Calibration

As with the EOSs, MPEXS did not have any burn models built in that had been calibrated for RDX at the start of this research. Although the goal of this research was to remove the reliance on empirically based burn models in macro-scale hydrocodes, they were still required in order to validate the EOSs and to provide a

point of comparison for the ARCIIST technique. Of the three traditional burn models built into MPEXS, the SPD and SIG were the most straight forward to recalibrate to represent RDX.

5.2.1 Simple Pressure-Dependent Burn Model

The SPD burn model, shown in Equation 50, was proposed by Schwendeman et. al. for a generic PBX [46]. Dr. Crochet had adapted Schwendeman's burn model to be more representative of pure HMX within MPEXS. Since most PBXs are either HMX or RDX based, this model was a logical choice to further adapt for use in simulating pure RDX.

$$\mathcal{C} = \begin{cases} -\sigma \phi_s \rho_s \frac{(P_g - P_{ign})}{P_{CJ}} & P_g > P_{ign} \\ 0 & P_g \leq P_{ign} \end{cases} \tag{50}$$

In the simple pressure dependent burn model, P_{CJ} is the CJ pressure, P_{ign} is the ignition pressure, and σ is the reaction rate prefactor used to "tune" the burn model to match experimental run-to-detonation data. It should be noted that the value for P_{ign} suggested by Schwendeman is very small compared to the pressures which rapidly develop within the simulations. Thus, P_{ign} is negligible for the piston speeds used in this research. Since this burn model had not previously been calibrated for RDX, σ was set to 4, 10, and 15 for these simulations. Three initial piston velocities were tested for each σ, resulting in a total of nine simulations to calibrate SPD for RDX. A summary of the piston speeds and burn model parameters used in the simulations to calibrate SPD is shown in Table 6. The other initial conditions for these simulations are identical to those used in the EOS validation study, found in Table 5.

MPEXS tracks the position of the leading wave front. From this information, the distance at which the wave speed sharply increases, or the run-to-detonation point,

Table 6. Piston Speeds, Initial Impact Pressures and Burn Model Parameters for SPD Calibration Simulations

u_p $[km/s]$	P_{impact} $[GPa]$	P_{CJ} $[GPa]$	P_{ign} $[GPa]$	σ
0.5	2.98			
0.75	5.04	26	2.982 x 10^{-4}	4, 10, **15**[*]
1.0	7.49			

[*] Prefactor value found to best calibrate SPD to represent RDX.

was found. The Pop-Plot was designed specifically for shock initiated detonations. It correlates the observed run-to-detonation distance with the initial pressure jump experienced by the condensed explosive when it is impacted by a flier or a piston. The initial pressure response is directly proportional to the flier or piston speed at the time of impact. Through analysis of the non-reactive Hugoniot for RDX [14], the expected initial pressure for each of the piston speeds in Table 6 was calculated. These impact pressures are enumerated in Table 6 next to their associated piston speeds.

Figure 12 shows the run-to-detonation data from the nine SPD calibration simulations plotted against experimental data for PBX-9405 (93.7% RDX) and PBX-9407 (94% RDX) [21]. Since there was no experimental Pop-Plot data available for pure RDX, these two RDX based explosives provided the best comparative data for the MPEXS simulations of RDX. The data series for PBX-9405 and PBX-9407 both show that run-to-detonation distance decreases as the initial shocked pressure of the explosive is increased. This correlation appears nearly linear when plotted on a log-log scale. It should be noted that the slope of both data sets appears to be nearly identical. This observation seems intuitive since both PBXs are RDX based, thus both depend on the same chemical decomposition rates to accelerate the shock front until detonation is reached. The downward shift of PBX-9407 to shorter run-to-detonation distances compared to PBX-9405 can be explained by their respective ratios of binder

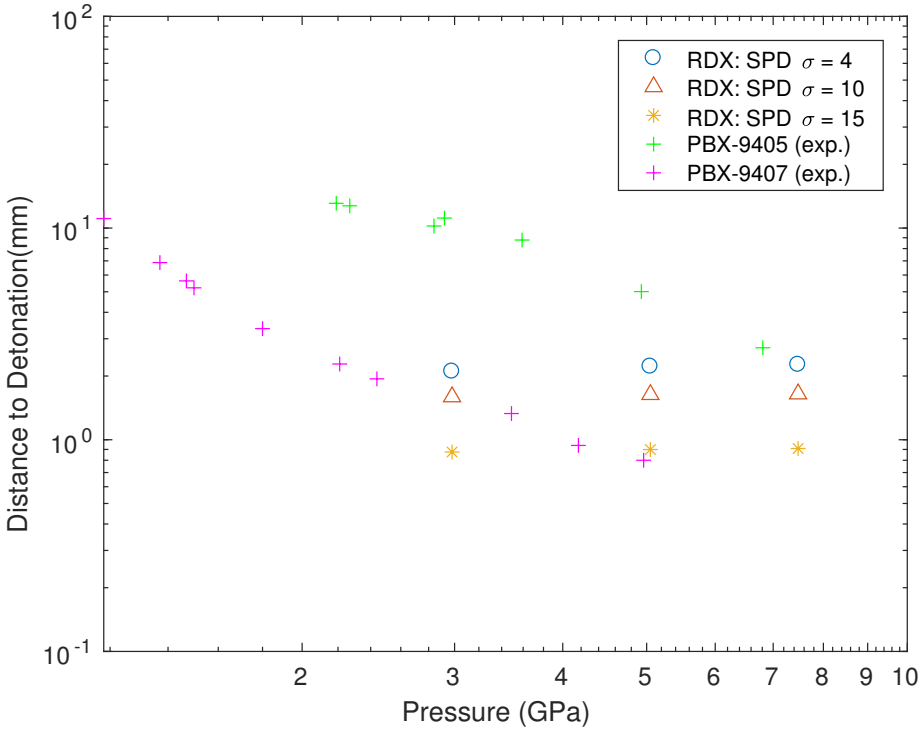

Figure 12. Pop-Plot comparison of MPEXS RDX simulations using the SPD burn model with experimental data for PBX-9405 and PBX-9407

material to RDX. Since PBX-9407 has a greater percentage of explosive in its composition, it should be no surprise that it reaches detonation earlier than PBX-9405 under the same initial pressure. It can be extrapolated, therefore, that simulations of pure RDX should result in a data set with a similar slope as these two PBXs and should fall near, or slightly below, the data set for PBX-9407.

The data from the SPD calibration study in Figure 12 did not line up well with either of the PBX data sets. Unlike the experimental data, the MPEXS simulations using SPD showed no variation in the computed run-to-detonation distance as the piston speed, and corresponding initial pressure, was increased. The data does show a downward shift in the run-to-detonation distance as the SPD prefactor σ increased. Since σ was the only tunable parameter in the SPD burn model, it was impossible to adjust the slopes of the data sets to better align with the experimental data. For the

simulated input pressures, the series using a σ of 15 came the closest of the three SPD series to matching run-to-detonation distances of PBX-9407 for the range of piston speeds tested. Thus, SPD with the conditions in Table 6 and a prefactor of 15 was considered calibrated to RDX for the purpose of making comparisons with ARCIIST. For this research, SPD was utilized as a point of comparison with the simplest class of burn models.

5.2.2 Simplified Ignition and Growth Burn Model

The Ignition and Growth burn model developed by Lee and Tarver is one of the most widely used burn models in macro-scale hydrocodes like MPEXS [34] [54]. Not only have the methods to calibrate the burn model from experimental measures become well established, but it is also the model most used for comparison when developing new burn models. Unfortunately, as mentioned in Section 5.2.1, the run-to-detonation data required to calibrate the Ignition and Growth model for RDX was not readily available and the model had too many tunable parameters for trial and error to be effective.

In addition to Lee and Tarver's burn model, MPEXS also had a simplified version of the Ignition and Growth model available. The SIG burn model, shown in Equation 51, was developed by Stewart et. al. to retain many of the Ignition and Growth model features with fewer parameters requiring calibration [48]. In Equation 51, κ is the burn rate constant, ν is the depletion exponent, and N is the pressure exponent. These three constants can be adjusted to match the run-to-detonation and detonation velocity curvature data for a given explosive.

$$\mathcal{C} = \kappa\overline{\rho}\,(1-\lambda_g)^{\nu}\left(\frac{\overline{P}}{P_{CJ}}\right)^{N} \tag{51}$$

Table 7. Piston Speeds, Initial Impact Pressures and Burn Model Parameters for SIG Calibration Simulations

$u\ [km/s]$	$P_{impact}\ [GPa]$	$P_{CJ}\ [GPa]$	$k\ [\mu s^{-1}]$	ν	N
0.5	2.98				
0.75	5.04	26	110	0.8	2.5
1.0	7.49				

The SIG burn model had previously calibrated within MPEXS to simulate PBX-9501, an HMX based explosive [37]. Given that RDX and HMX are both cyclonitramine explosives which have been shown to exhibit similar properties, the PBX-9501 values for κ, ν, and N were used as a starting point for calibrating SIG for RDX. The value of P_{CJ} was adjusted to 26 GPa. These SIG parameters along with the three piston speeds tested are summarized in Table 7.

The run-to-detonation results from the three simulations which used the param-

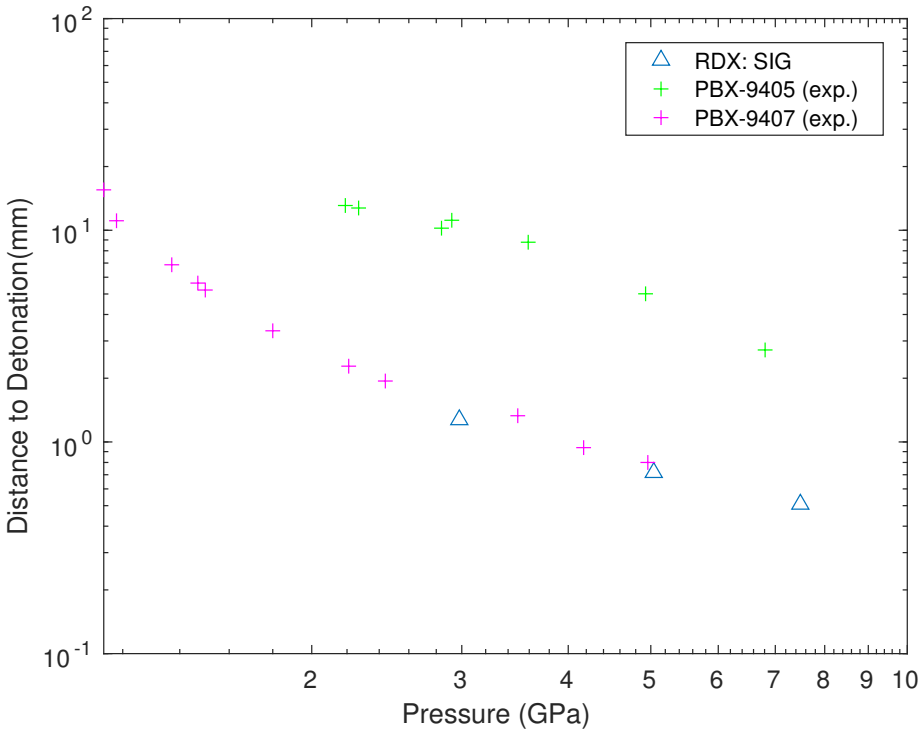

Figure 13. Pop-Plot comparison of a MPEXS RDX simulation using a the SIG burn model with experimental data for PBX-9405 and PBX-9407

eters in Table 7 are plotted in Figure 13 and compared to the experimental data for PBX-9405 and PBX-9407. Fortunately, the computed results using SIG aligned very well with the Pop-plot data for PBX-9407, particularly at the higher initial pressure ranges where the majority of the simulations in this research were conducted. No further adjustments to the SIG calibration parameters were carried out.

5.3 Spatial and Temporal Refinement Studies

The use of MPEXS to simulate explosive materials is well established [15] [17] [18] [19] [37], however it had never been used in the configurations needed for this research. Although MPEXS was already programmed with the MG and JWL EOS as well as the SPD and SIG burn models, the parameters chosen to represent RDX had never been tested together in MPEXS. Even more critical to this research, using ARCIIST to integrate the NRL chemistry model into a macro-scale continuum hydrocode had not been tested using MPEXS or any other platform. For these reasons, temporal and spatial refinement studies were conducted to ensure the appropriate discretization levels were chosen in order to conduct accurate and efficient simulations.

5.3.1 Temporal Refinement

MPEXS dynamically chooses a time step size (Δt) for each iteration based on the maximum wave propagation speed (a_x) and cell length (Δx). The time step is limited by the CFL number ($\breve{c}$) chosen by the user and is computed using Equation 52. Since a set Δt cannot be chosen directly in MPEXS, temporal refinement studies were conducted by testing various CFL numbers while holding all other simulation parameters constant.

$$\Delta t = \frac{\breve{c}}{2\left(\frac{a_x}{\Delta x}\right)} \tag{52}$$

Table 8. Initial Conditions for Temporal Refinement with ARCIIST

ρ_s $[g/cm^3]$	ϕ_s	$\overline{\rho}$ $[g/cm^3]$	P $[GPa]$	T $[K]$	u_p $[km/s]$
1.8	0.9	1.6	1.013E-4	300	1.0

Table 9. CFL Conditions for Temporal Refinement with ARCIIST

CFL	$Average\ \Delta t$ $[\mu s]$
0.2	1.2 x 10^{-5}
0.5	3.0 x 10^{-5}
1.0	5.7 x 10^{-5}
2.0	11.0 x 10^{-5}

The temporal refinement study conducted with ARCIIST used the initial conditions and parameters shown in Table 8. Four simulations were run, each with a different CFL condition. These conditions are shown in Table 9 along with the corresponding average time step size from each simulation. The results of this study are shown in Figures 14 - 17. These figures show the profiles for mixture pressure ($\overline{P}$), mixture temperature ($\overline{T}$), mixture density ($\overline{\rho}$) and the condensed phase volume fraction (ϕ_s) at two snapshots in time. The snapshots were chosen to show the state of the simulation before and after detonation is reached.

In all four cases tested, the profiles of the key variables shown in Figures 14 - 17 were remarkably similar. Notably, the profiles for the 2.0 CFL case appear shifted and further advanced through DDT process when compared to the other three cases. In fact, all four cases have practically identical profiles for all key variables with minimal differences in magnitude when the leading shock waves are in the same position relative to the piston face. The difference is in the time it takes for those waves to reach a particular position. These differences were all dependent on when the NRL chemistry model initiated the mass exchange between the two phases. The smaller the time step size, the longer ignition was delayed and the longer it took to transition to full detonation. Thus, the detonation parameter most impacted by

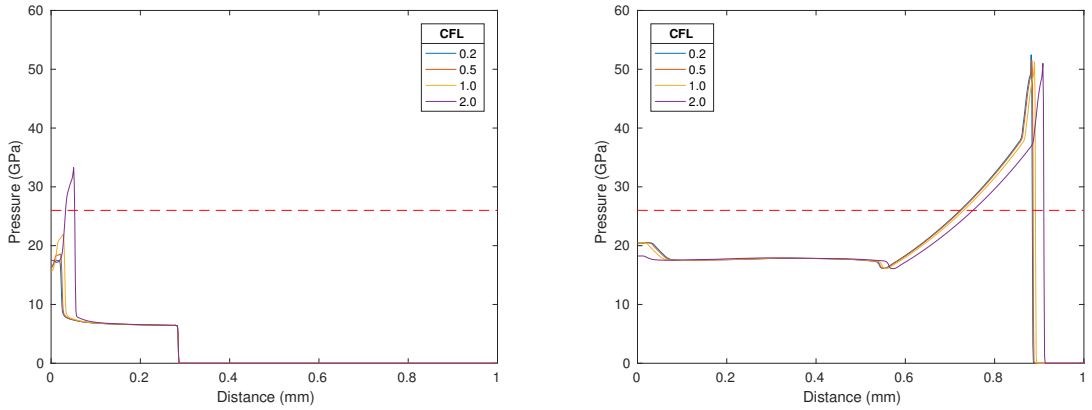

Figure 14. Temporal Refinement of MPEXS with ARCIIST: Mixture pressure ($\overline{P}$) profiles at (a) $0.1\mu s$ and (b) $0.2\mu s$. The dashed red line (- - -) represents RDX CJ pressure. Piston speed of 1 km/s used in all cases.

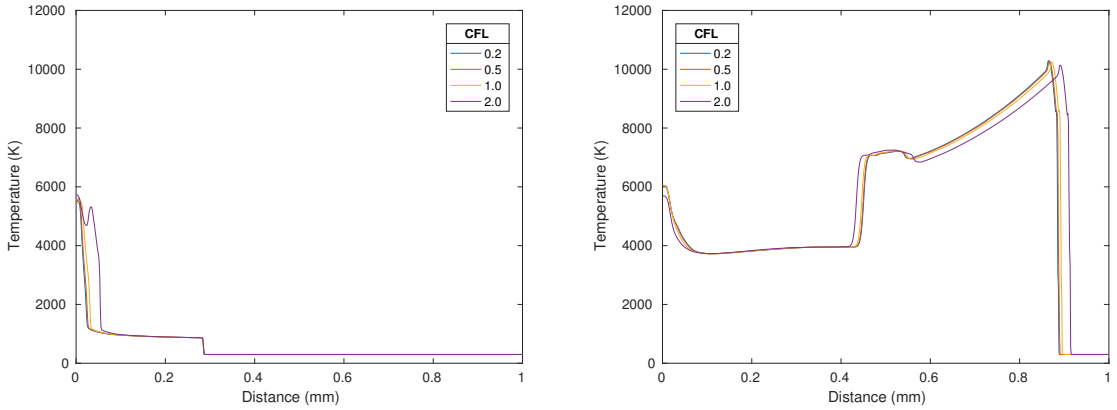

Figure 15. Temporal Refinement of MPEXS with ARCIIST: Mixture temperature ($\overline{T}$) profiles at (a) $0.1\mu s$ and (b) $0.2\mu s$. Piston speed of 1 km/s used in all cases.

the choice of time step size is the run-to-detonation distance, and not the four key variables shown in the figures.

In Figures 14 - 17, the overall differences between the 0.2 and 0.5 CFL cases are very minute. Thus the choice of temporal refinement was narrowed down to the 0.5 and 1.0 CFL cases. Looking at the run-to-detonation distances, there was only a 5% difference (0.02 mm) between the two cases. The computational effort required

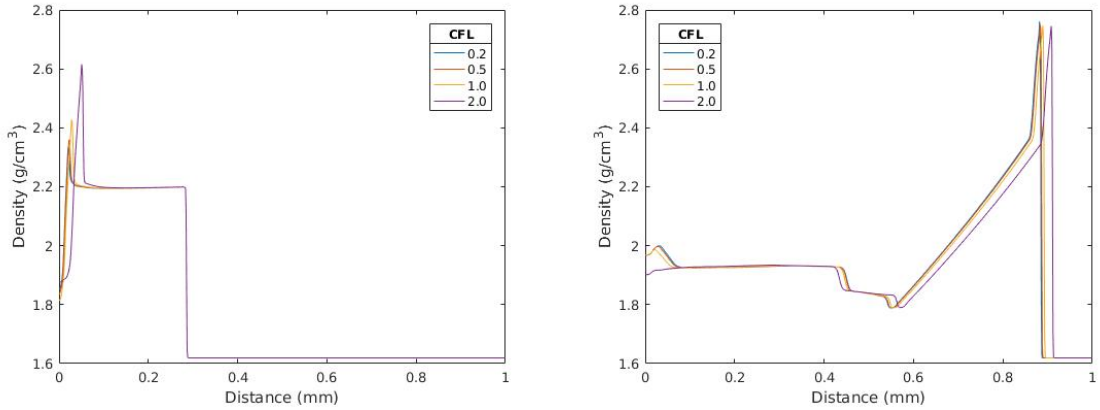

Figure 16. Temporal Refinement of MPEXS with ARCIIST: Mixture density ($\overline{\rho}$) profiles at (a) $0.1\mu s$ and (b) $0.2\mu s$. Piston speed of 1 km/s used in all cases.

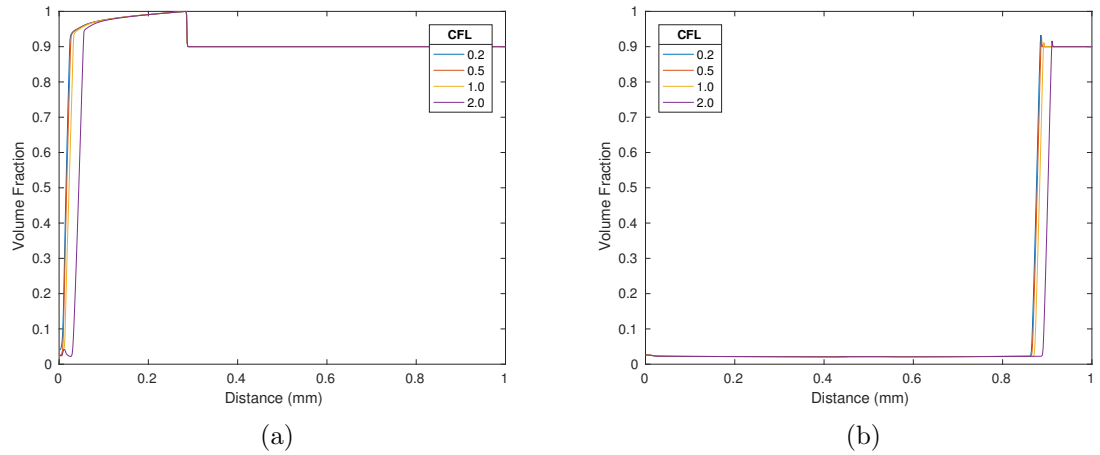

Figure 17. Temporal Refinement of MPEXS with ARCIIST: Condensed phase volume fraction (ϕ_s) profiles at (a) $0.1\mu s$ and (b) $0.2\mu s$. Piston speed of 1 km/s used in all cases.

to complete the simulations, however, was far more significant. The 1.0 CFL case took half as much time to complete as the 0.5 CFL case. Furthermore, it was six times faster than the 0.2 CFL case. Given the uncertainty of how many simulations would need to be conducted, the choice was made to use a CFL number of 1.0 for all simulations using ARCIIST.

A similar series of temporal refinement simulations were conducted using SIG burn

model instead of ARCIIST. The results are included in Appendix B. There were no distinguishable differences observed in the profiles of the four primary variables or the run-to-detonation distance. It was decided that a CFL of 1.0 would be used for all tests using SIG to be consistent with ARCIIST runs.

Like SIG, the SPD burn model is also pressure dependent and operates in a similar manner within MPEXS. Thus, a CFL of 1.0 was also chosen for all SPD simulations based on the results of the SIG study. It should be noted that a small refinement study had been conducted with SPD during the early phases of this research when the feasibility of ARCIIST was being determined [41] [42] [43]. These early studies further supported the decision to use a CFL of 1.0.

5.3.2 Spatial Refinement

Once the temporal refinement was completed, the spatial discretization level was determined by conducting a spatial refinement study. In MPEXS, the spatial domain is divided into numerous cells of equal length. The user defines the cell length by choosing the length of the domain and the number of cells the domain is to be divided into. To keep the cell lengths consistent regardless of the domain length, spatial refinement (N_x) was determined in terms of number of cells per mm.

Table 18 shows initial conditions and refinement levels tested for the spatial refinement study conducted using ARCIIST. This study was conducted in similar fashion as the temporal refinement study. The only major difference was the decision to run these simulations with a piston speed of 1.2 km/s. It had been observed that, when a 1.0 km/s piston speed was used, the chemistry initiation point varied drastically

Table 10. Initial Conditions for Spatial Refinement with ARCIIST

ρ_s $[g/cm^3]$	ϕ_s	$\overline{\rho}$ $[g/cm^3]$	P $[GPa]$	T $[K]$	u_p $[km/s]$	N_x $[cells/mm]$
1.8	0.9	1.6	1.013E-4	300	1.2	400, 800, 1600

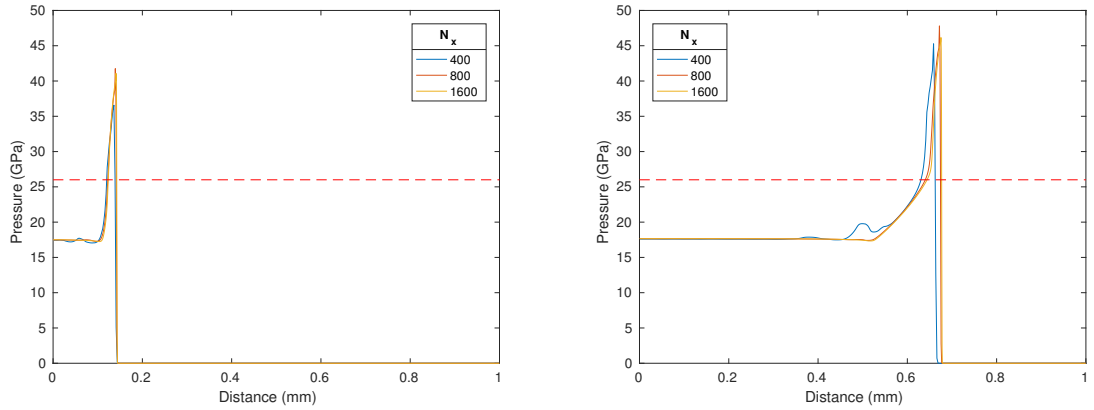

Figure 18. Spatial Refinement of MPEXS with ARCIIST: Mixture pressure ($\overline{P}$) profiles at (a) $0.025\mu s$ and (b) $0.1\mu s$. The dashed red line (- - -) represents RDX CJ pressure. Piston speed of 1.2 km/s used in all cases.

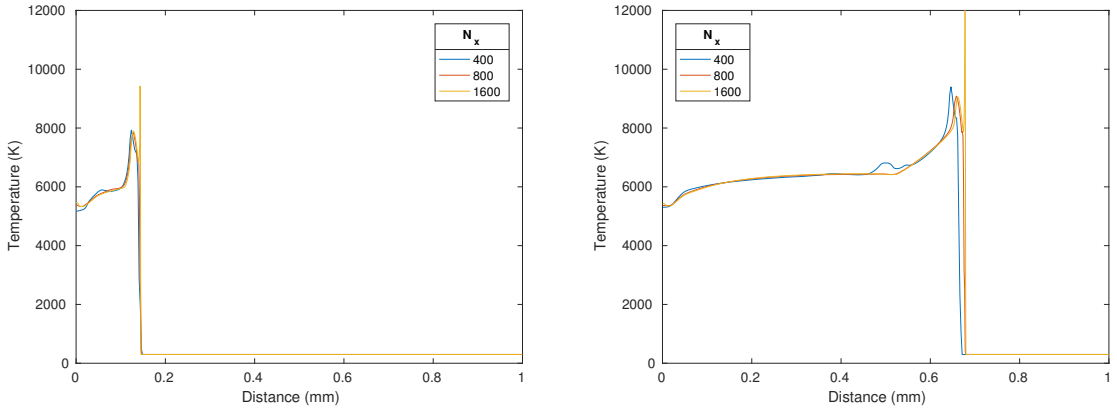

Figure 19. Spatial Refinement of MPEXS with ARCIIST: Mixture temperature ($\overline{T}$) profiles at (a) $0.025\mu s$ and (b) $0.1\mu s$. Piston speed of 1.2 km/s used in all cases.

depending on the choice of N_x. Refinement beyond 1600 cells per mm resulted in prohibitively large computation times and there was seemingly no convergence to a solution up to that point. Thus, the piston speed was increased to 1.2 km/s where the run-to-detonation distance was less than 1.0 μm and detonation occurred nearly instantaneously when the simulation was started. The use of the 1.2 km/s piston resulted in a far more stable simulation to compare the impact of spatial refinement

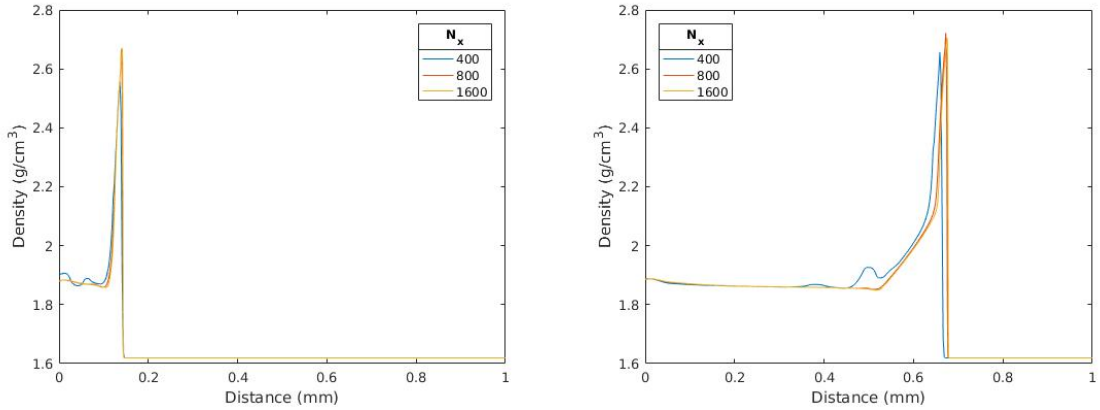

(a) (b)

Figure 20. Spatial Refinement of MPEXS with ARCIIST: Mixture density ($\overline{\rho}$) profiles at (a) $0.025\mu s$ and (b) $0.1\mu s$. Piston speed of 1.2 km/s used in all cases.

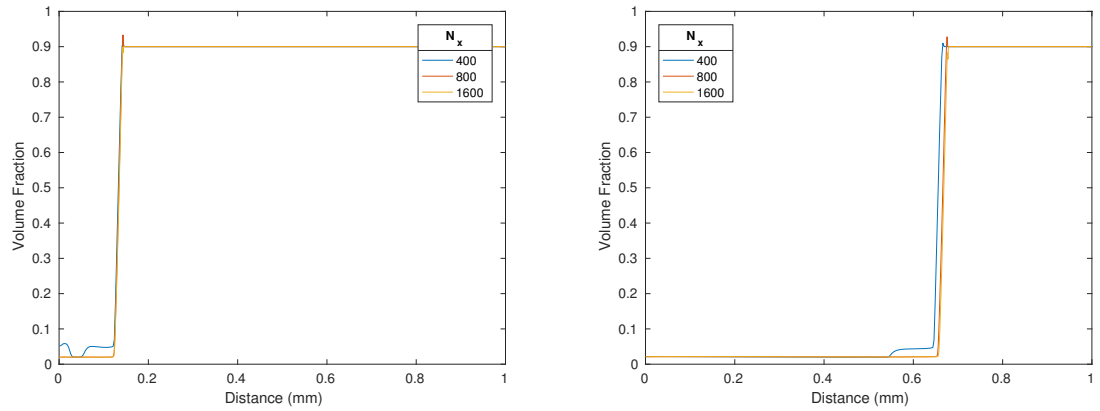

(a) (b)

Figure 21. Spatial Refinement of MPEXS with ARCIIST: Condensed phase volume fraction (ϕ_s) profiles at (a) $0.025\mu s$ and (b) $0.1\mu s$. Piston speed of 1.2 km/s used in all cases.

on the system.

Results from the spatial refinement study using ARCIIST are shown in Figures 18 - 21. There was very little deviation between 800 and 1600 N_x cases. The 400 N_x case, however, showed significant fluctuations in all four primary variables post shock. These fluctuations were not present in the higher resolution cases, proving that an N_x of 400 was not refined enough for ARCIIST simulations.

The biggest difference between the 800 and 1600 N_x cases occured in the temperature profiles, shown in Figure 19. The 1600 N_x cases has a large spike in temperature right at the detonation front which is not present in the 800 N_x case. The rest of the temperature profile is the same for these cases, suggesting that 1600 N_x is too refined and is resulting in a numerical error due to lack of dissipation. Because of this, a N_x value of 800 cell per mm was chosen for all ARCIIST simulations.

A similar series of spatial refinement tests were conducted using SIG with a 1.0 km/s piston speed. These results are presented in Appendix B. As with the temporal refinement study, there were few distinguishable differences observed in the profiles of the four primary variables or the run-to-detonation distance. For this reason, a N_x of 400 cell per mm was chosen for all SIG simulations. Refinement levels for SPD were set identical to SIG for the same reasons explained in Section 5.3.1.

5.4 ARCIIST Test Plan

Once the validation and verification of all the simulation components and refinement levels were completed, thorough testing was conducted in order to prove that the ARCIIST technique developed in this research could be used to create a simultaneous multi-scale simulation of explosive material. In addition to the MPEXS simulations of RDX using ARCIIST, simulations were also conducted using the SPD and SIG burn models for comparison purposes. Table 11 is a four part table summarizing all of the parameters used as input to MPEXS to conduct these simulations. The initial conditions and EOS parameters were common to all simulations run in MPEXS. The third section of Table 11 shows the specific parameters specified for each burn or chemistry model to calculate the mass exchange rate between the condensed and gaseous phases. Finally, the last section notes the differences in spacial refinement between the simulations using traditional burn models and those using ARCIIST.

Table 11. ARCIIST Testing Simulation Parameters

Initial Conditions

ρ_s $[g/cm^3]$	ϕ_s	$\overline{\rho}$ $[g/cm^3]$	P $[GPa]$	T $[K]$
1.8	0.9	1.6	1.013E-4	300

EOS Parameters

Condensed Phase:	MG[1]
Gaseous Phase:	JWL[2]

Burn/Chemistry Modeling Parameters

SPD	P_{CJ} $[GPa]$ = 26; P_{ign} $[GPa]$ = 2.982 x 10^{-4}; σ = 15
SIG	P_{CJ} $[GPa]$ = 26; k $[\mu s^{-1}]$ = 110; ν = 0.8; N = 2.5
ARCIIST	NRL's RDX Model[3]: Condensed Phase: Species 1 and 2; Gaseous Phase: Species 3-11

Refinement Parameters

Burn/Chem. Model	N_x [cells per mm]	CFL
SPD	400	1.0
SIG	400	1.0
ARCIIST	800	1.0

[1] Ref. Table 1
[2] Ref. Table 2
[3] Ref. Tables 3 & 4

Other than the choice between burn models or ARCIIST, the only variation between simulations was the piston speed used to initiate the shock wave in the system. Table 12 shows the various piston speeds used with each of the burn models and ARCIIST. It also annotates the initial impact pressures associated with each piston speed tested. It should be noted that speeds of 0.5, 0.75, 1.0, and 1.5 km/s were common to all models. Additional points were added during testing in the series of ARCIIST simulations to verify the run-to-detonation trends that were observed. Furthermore, in the 0.5 and 0.75 km/s cases ARCIIST, the simulation was terminated before detonation was observed.

Results of the MPEXS simulations using ARCIIST were compared with those using SPD or SIG by capturing the profiles of key variables such as temperature and pressure at set times in the simulations. The velocity profiles from the ARCIIST simulations were also compared to those of the HMX based explosive LX-14, which were obtained experimentally by Jones et. al. [29]. Furthermore, the run-to-detonation data from all of the MPEXS simulations were compared against the experimental data for PBX-9405 and PBX-9407, similar to the analysis conducted in Section 5.2. All of these results are presented with detailed discussion in Chapter VI

Table 12. ARCIIST Test Matrix

Burn/Chemistry Model	u_p $[km/s]$	P_{impact} $[GPa]$
SDP and SIG	0.5	2.98
	0.75	5.04
	1.0	7.49
	1.5	13.51
ARCIIST	0.5**	2.98
	0.75**	5.04
	0.96*	7.07
	0.97*	7.18
	0.98*	7.28
	0.99*	7.38
	1.0	7.49
	1.01*	7.59
	1.02*	7.7
	1.03*	7.81
	1.04*	7.92
	1.05*	8.02
	1.1*	8.57
	1.2*	9.72
	1.5	13.51

* Simulations added during testing process.

** Simulations did not reach detonation.

VI. Results and Analysis

This chapter presents the results and analysis from the test plan outlined in Section 5.4. The first section analyzes the key physical features that were captured by MPEXS as a result of using of the ARCIIST method. Section 6.2 compares the results of the simulations using ARCIIST with those using the SPD and SIG burn models. In Section 6.3, the results of the MPEXS simulations are qualitatively compared to empirical results from LX-14 experiments. This comparison proves that the ARCIIST results capture actual DDT phenomenon which can be missed when using common pressure-dependent burn models. Section 6.4 analyzes the run-to-detonation computations for all of the simulations series in Table 12. This data is plotted against the experimental results for PBX-9405 and PBX-9407 for reference. Finally, it was discovered that the ARCIIST configuration described in the previous chapters resulted in a model of RDX which is uncharacteristically insensitive to shock initiated detonation. Section 6.5 presents the theory on why the use of ARCIIST resulted in this insensitivity. It also provides a modification to the ARCIIST model to artificially increase the sensitivity of the explosive. This modification and its corresponding tests were accomplished and demonstrated the need to properly model the influence of hot-spots, voids, and crystal damage mechanisms on DDT initiation in macro-scale continuum explosive hydrocodes.

6.1 Analysis of ARCIIST Results

Fifteen separate simulations of RDX were conducted with MPEXS using the ARCIIST technique. As shown in Table 12, most of these runs were added to the test matrix during testing to confirm the run-to-detonation distance trends being observed. These observations will be discussed more in Sections 6.4 and 6.5. Profiles

of four primary variables were observed during these simulations in the same manner as the the temporal and spatial refinement studies. The evolution over time of the mixture pressure ($\overline{P}$), mixture temperature ($\overline{T}$), mixture density ($\overline{\rho}$), and condensed phase volume fraction (ϕ_s) gave a clear indication of whether the use of ARCIIST reasonably simulated a shock initiated detonation of RDX. The profiles of these primary variables are shown in Figures 22 - 25 for the case where the piston speed (u_p) was set to 1.0 km/s. Similar sets of figures for the 0.96 km/s and 1.2 km/s piston cases are provided in Appendix C. Each figure shows a sequence of profiles over time. When viewing these profiles, it is important to remember that MPEXS operates on a piston attached reference frame. As such, the left side of the domain is always associated with the solid, impervious piston face and the distances in the figures represent the distance in front of the moving piston.

Examining the 1.0 km/s piston case, there are some key features and critical transition points captured in the profiles of the four primary variables. In the first few frames of the sequence (0 to 0.05 μs), a step function is observed in all four variables. This behavior is expected from a shock wave passing through any condensed material. It should be noted that as the shock wave passes, the pressure raises to approximately 6 GPa. This response is just under the expected 7 GPa pressure rise from analysis of the non-reacting Hugoniot for RDX and is a good indication that the early behavior of the RDX system was correct in the simulations. There is also a sharp rise in density and the mixture becomes compacted to the point where the volume fraction of the condensed phase is nearly 1. Thus, there is almost no gaseous material near the piston face at the far left side of the domain early in the simulation. Although barely noticeable, there was a slow, gradual temperature rise in the system closer to the piston face. By the second frame (0.05 μs), portions of the domain had risen above 800 K, the threshold for the NRL chemistry model to initiate reactions

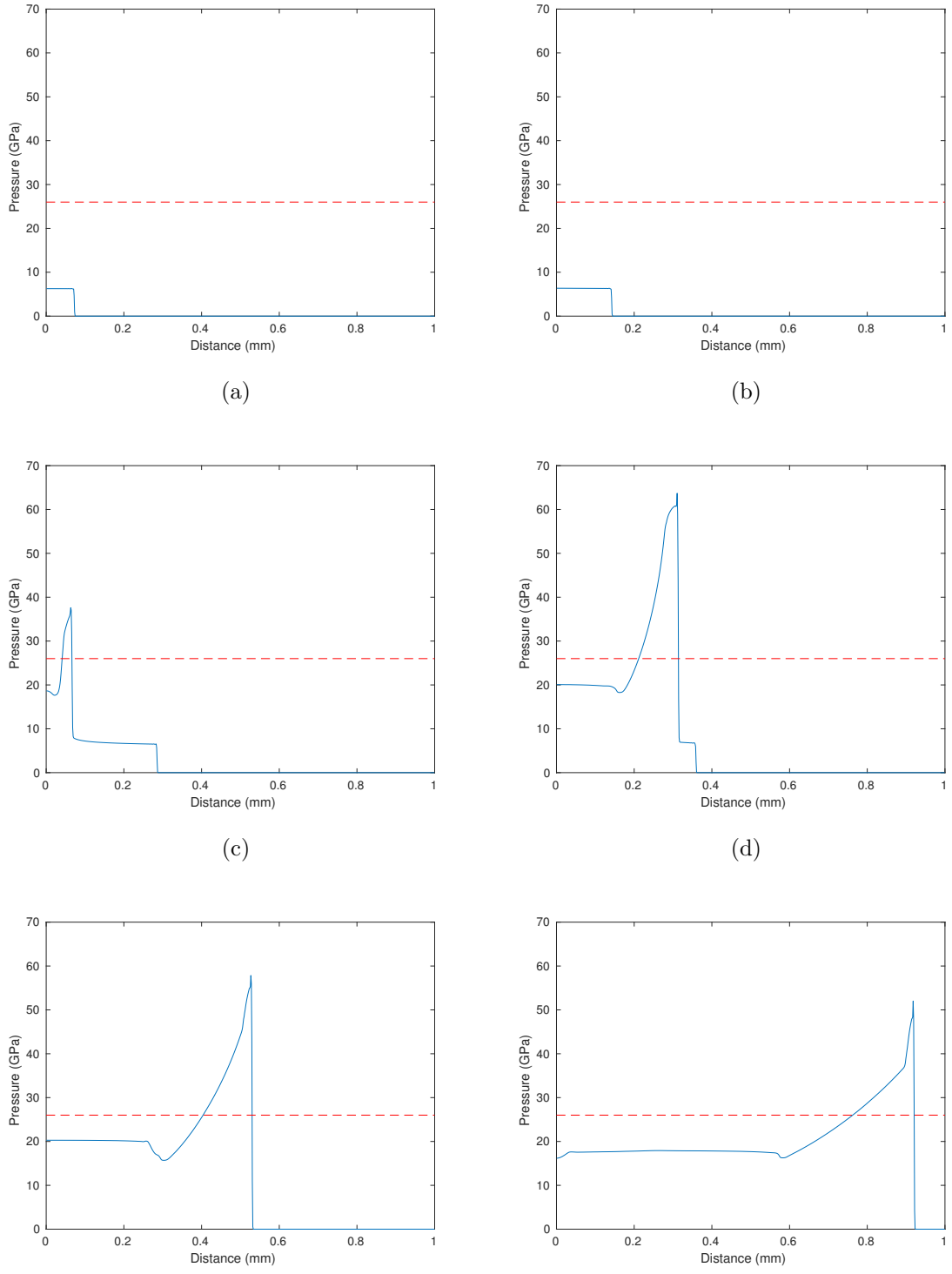

Figure 22. RDX mixture pressure ($\overline{P}$) profiles using ARCIIST with a 1.0 km/s piston at (a) 0.025, (b) 0.05, (c) 0.1, (d) 0.125, (e) 0.15, and (f) 0.2 μs. The dashed red line (- - -) represents RDX CJ pressure.

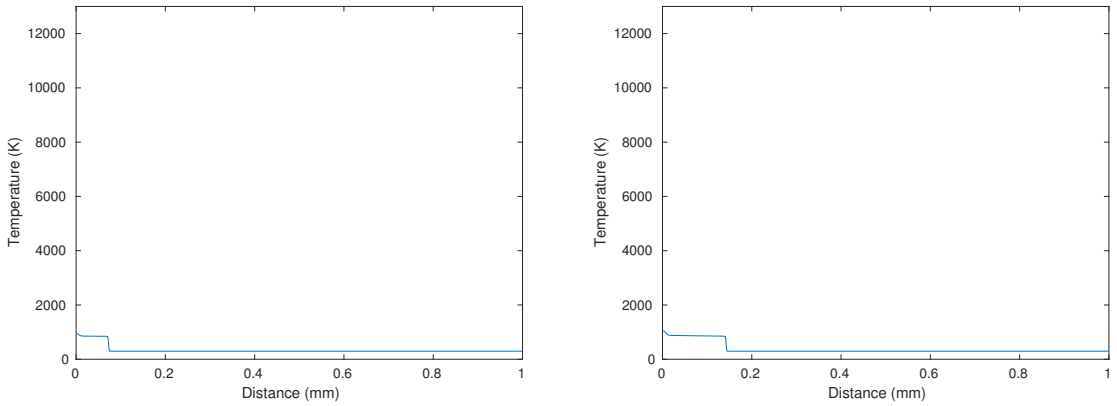

(a)

(b)

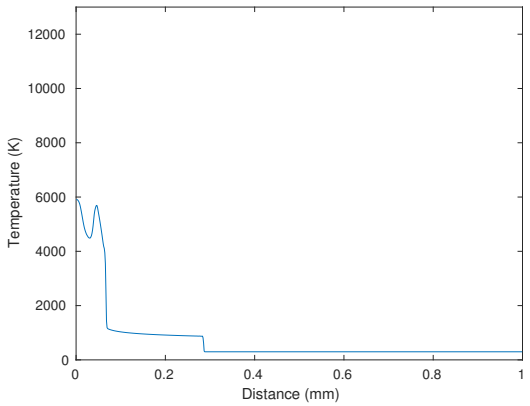

(c)

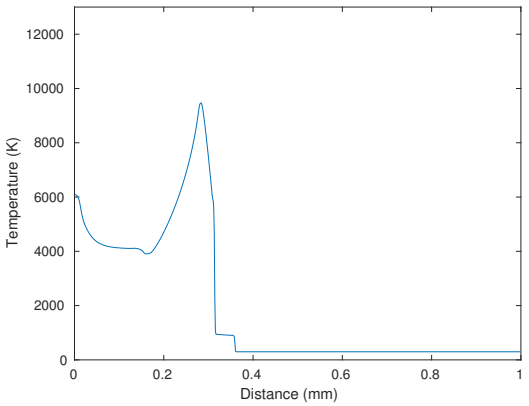

(d)

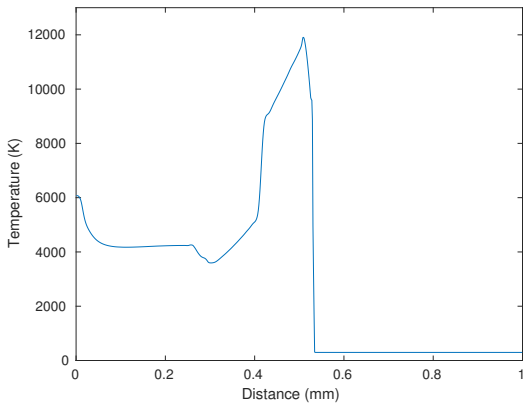

(e)

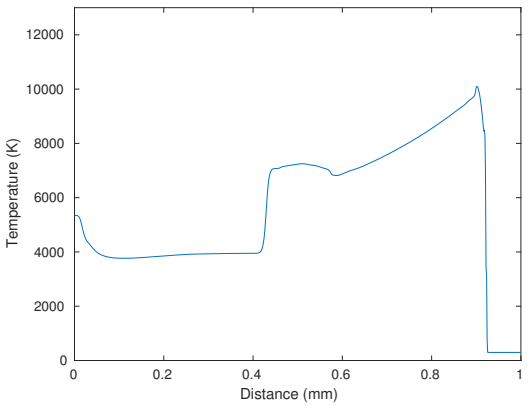

(f)

Figure 23. RDX mixture temperature ($\overline{T}$) profiles using ARCIIST with a 1.0 km/s piston at (a) 0.025**, (b)** 0.05**, (c)** 0.1**, (d)** 0.125**, (e)** 0.15**, and (f)** 0.2 μs**.**

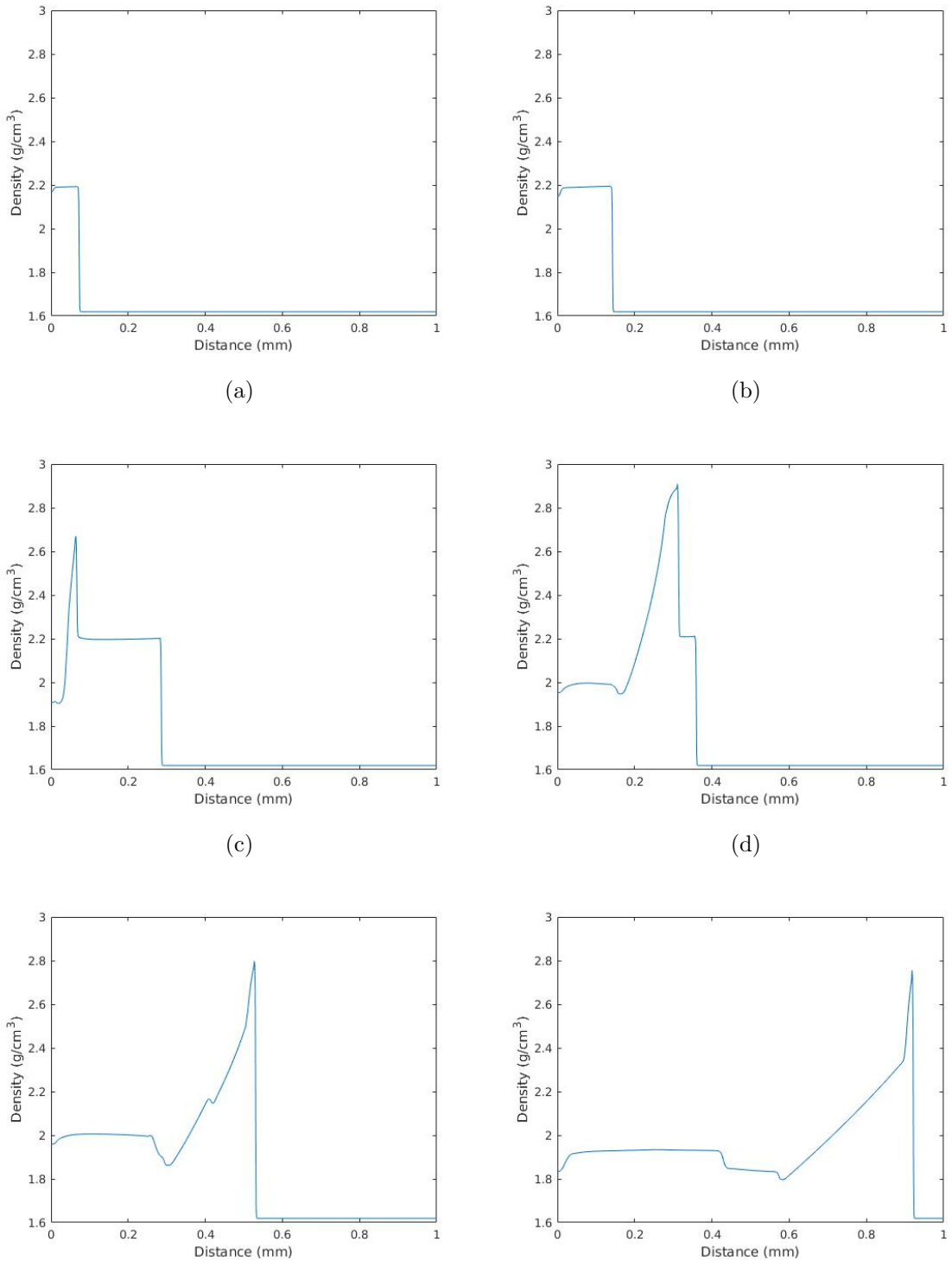

Figure 24. RDX mixture density ($\overline{\rho}$) profiles using ARCIIST with a 1.0 km/s piston at (a) 0.025**, (b)** 0.05**, (c)** 0.1**, (d)** 0.125**, (e)** 0.15**, and (f)** 0.2 μs**.**

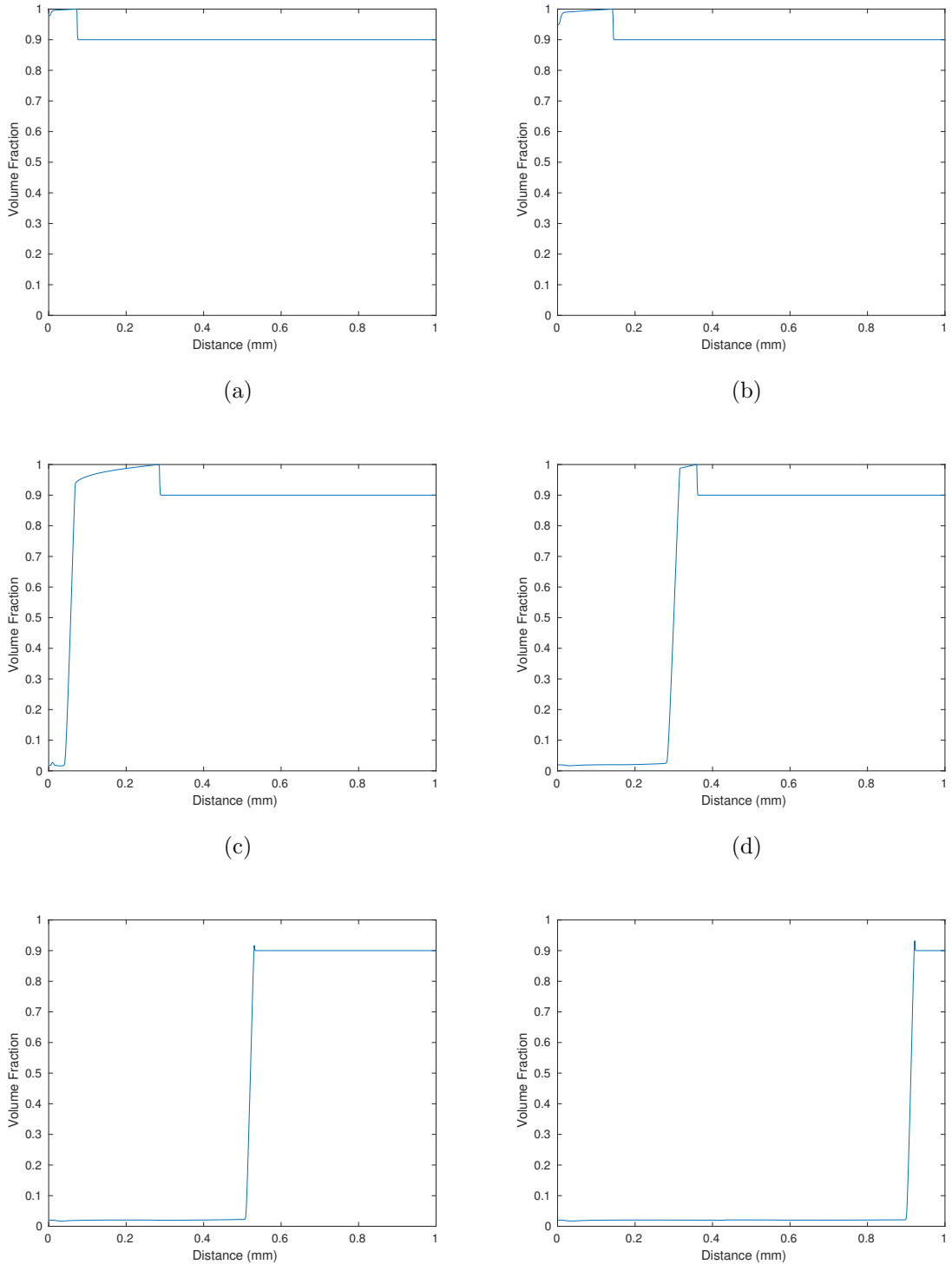

Figure 25. RDX condensed phase volume fraction (ϕ_s) profiles using ARCIIST with a 1.0 km/s piston at (a) 0.025**, (b)** 0.05**, (c)** 0.1**, (d)** 0.125**, (e)** 0.15**, and (f)** 0.2 μs**.**

in RDX to a significant degree. There is a corresponding drop in density and condensed volume fraction in these regions as well.

By the third frame (0.1 μs), parts of the domain have had temperatures rise above the 1000 K threshold. At this point, the reaction rate of RDX jumps dramatically, as indicated by the near vertical drop in the condensed volume fraction. The initiation of a runaway chemical reaction results in a secondary wave front. Behind this front, the pressure and temperature of the system spiked up. Density was momentarily increased, but then dropped off rapidly as the material behind the second wave was converted to gaseous products. The secondary wave front accelerated to a velocity greater that that of the initial shock wave for two reasons. First, the secondary wave was traversing through material that had been compacted by the initial shock wave and is much denser. Secondly, the rapid creation of gaseous products from the runaway chemical reactions behind the second wave front continually strengthened the second wave. As shown in the fourth and fifth frame (0.125 to 0.15 μs), the secondary wave catches up to, and merges with the initial shock front. This phenomenon is the very definition of detonation. The formation of the secondary wave and its role in DDT has been observed experimentally and will be discussed further in Section 6.3. However, capturing this phenomenon in a macro-scale continuum simulation is unique to ARCIIST simulations. It will be shown in Section 6.2 that simulations using common pressure-dependent burn models fail to capture this key feature of DDT.

Once the detonation front formed, it traversed through porous RDX with the initial system density of approximately 1.6 g/cm^3. In this transition there was a sudden drop in density from the compacted material the secondary wave had been traveling through. This also meant there was less condensed material available to react from this point forward. As such, the strength of the detonation wave gradually

diminishes, as seen in the last frame (0.2 μs). Eventually, the simulation levels off in a steady state condition.

Once detonation has been reached, key features developed in the pressure profiles which resemble the ideal detonation model developed by ZND [14]. In Figure 22f, the pressure underwent a huge jump at the detonation front. This jump was followed by a steep reduction in pressure behind the detonation front. This peak in the pressure profile corresponds with the Von Neumann spike from ZND theory. When cross referenced with Figure 25f, it was observed that the width of the spike correlates with the width of the reaction zone. This correlation is also consistent with ZND theory.

As the detonation wave reaches steady state, the pressure at the end of the reaction zone approaches the expected CJ pressure for RDX. This steady state condition was more clearly observed in the 1.2 km/s piston case (Figure 60f in Appendix C). Behind this point, the pressure underwent a more gradual relaxation as expected from the rarefaction wave which follows any strong shock. The striking resemblance of the computed post-detonation profiles to those from ZND theory is a strong indication that the ARCIIST technique improves MPEXS' ability to simulate shock initiated DDT.

In both simulations and experiments designed to capture DDT processes, the point of detonation is usually determined by finding the point where the leading wave front changes speed and then stabilizes on the steady detonation wave velocity. This run-to-detonation is most clearly seen by creating a pressure contour map of the results over space and time as seen in Figure 26. In this figure, there are two concentrated sets of pressure contours. The first begins from the start of the simulations (bottom of the plot) and marks the location of the leading shock wave caused the piston's initial impact. The steep, linear slope of this line shows that this wave front was

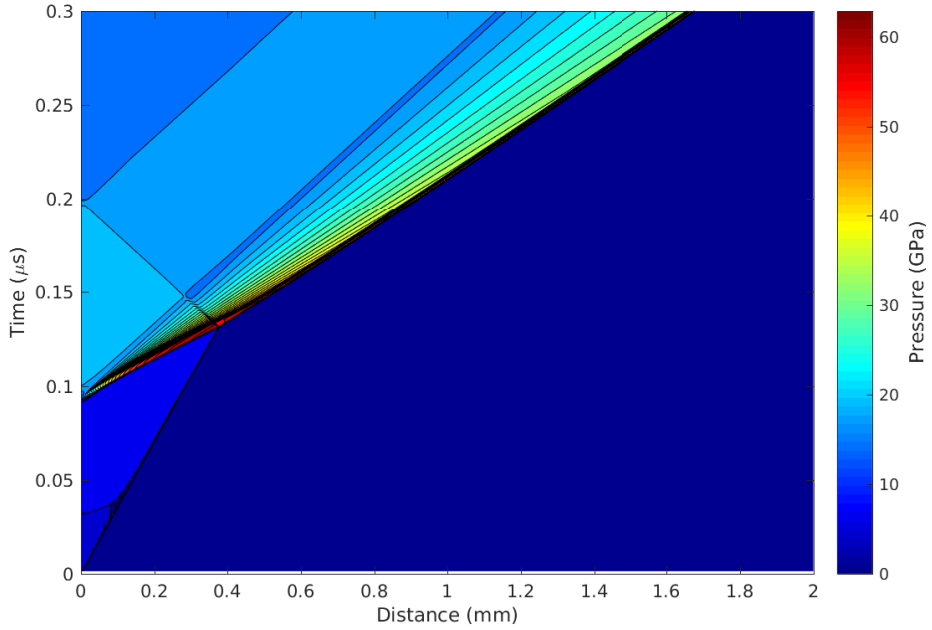

Figure 26. Pressure contour plot from an MPEXS simulation of RDX using ARCIIST. Piston speed was set to 1.0 km/s.

moving at a constant velocity ahead of the piston. The RDX ignited near the piston face in just under 0.1 μs, forming a second, stronger wave front. Unlike the first wave front, this secondary front had a slight curve, indicating that it was accelerating. The average velocity of this second wave was much greater than the initial shock wave and the two fronts eventually merged. After the two fronts merged, the new wave front quickly stabilized. The slope of this new front is clearly linear in form and indicates that the new front continued to propagate at a much faster velocity than the initial shock wave. Because the final wave front was stable, it became clear that full detonation has occurred. The run-to-detonation distance can be established as the point in which the initial shock wave and the secondary wave front merged, approximately 0.38 mm ahead of the piston face. When the distance the piston has traveled is taken into account, the total run-to-detonation distance from the point

of impact was calculated as 0.49 mm. Furthermore, the final detonation velocity for the simulation was found to be 8.7 km/s, only slightly higher than the detonation velocity of 8.13 km/s observed experimentally in RDX samples of similar density [14].

The same features described for the 1.0 km/s case were observed in all of the cases tested. The primary difference between cases was the time it took for ignition of the RDX to occur and, consequently, the run-to-detonation distance computed as a result. The cases with lower piston speeds took longer for ignition to develop. The secondary wave, therefore, had more distance to traverse in order to catch the leading shock wave and the run-to-detonation distance was longer. Because the secondary wave moved through more of the compacted RDX, it was observed that the pressure and temperature peaks of the secondary waves for lower piston speeds tended to be larger than those in the higher piston speed cases. Conversely, the higher piston speed cases had a stronger initial shock and reached ignition temperatures sooner. Thus, the secondary waves in these cases had less compacted material to traverse and reached detonation sooner. By the time the piston speed was increased to 1.1 km/s, the initial shock was strong enough to start ignition almost immediately after the initial piston impact. Detonation for the three highest piston speed cases showed near instantaneous detonation. As a consequence, the detonation wave had to strengthen and grow to steady state pressures instead of diminish as seen in the 1.0 km/s case. To show the differences between the various piston speeds tested, sets of primary variable profile plots and pressure contour plots for the 0.96 km/s and 1.2 km/s piston cases are provided in Appendix C.

In addition to producing output profiles which conform to ZND theory, the integration of ARCIIST added an additional capability to the MPEXS hydrocode. In addition to common variables of interest such as pressure and temperature, MPEXS simulations can now provide information on the formation and destruction of indi-

vidual chemical species during the explosive's decomposition process. Figures 27 - 29 show the mass fractions of condensed phase species, gaseous intermediate species and gaseous phase final species respectively for the 1.0 km/s piston speed case. The frames in these figures show two different instances in time, before and after detonation is reached.

While these profiles do provide an additional level of detail not previously available, the figures provide much of same information which can be gained from the volume fraction profiles from Figure 25. In particular, they confirm that there is a very thin reaction zone in these simulations. When combined with the fact that the NRL chemistry model for RDX has a relatively small number of reactions and chemical species, the thin reaction zone resulted in species profiles with very little dynamics even when other variables in the simulation had more drastic transitions. It is conceivable that if the ARCIIST technique is used with a more complex Arrhenius rate chemistry model, the resulting species mass fraction profiles could show more significant transition points. Inclusion of a third, intermediate phase within MPEXS could also potentially enhanced the significance of these transition points.

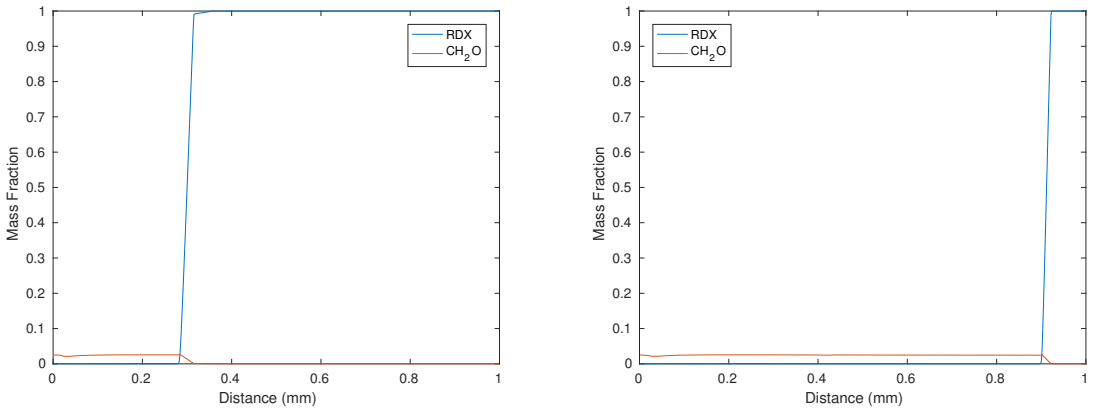

(a) (b)

Figure 27. Condensed phase species RDX, CH_2O, and N_2O mass fraction (Y_i) profiles using ARCIIST with a 1.0 km/s piston at (a) 0.125 **and (b)** 0.2 μs**.**

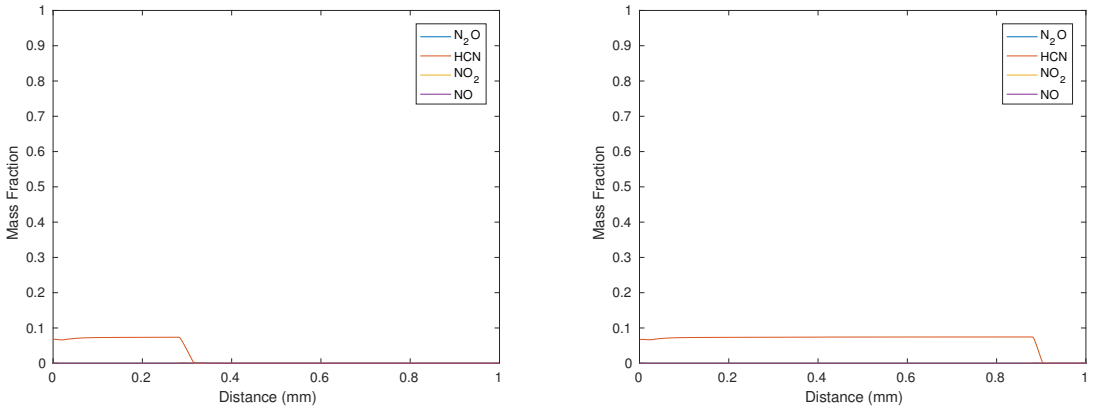

Figure 28. Gaseous phase intermediate species HCN, NO_2, and NO mass fraction (Y_i) profiles using ARCIIST with a 1.0 km/s piston at (a) 0.125 and (b) 0.2 μs.

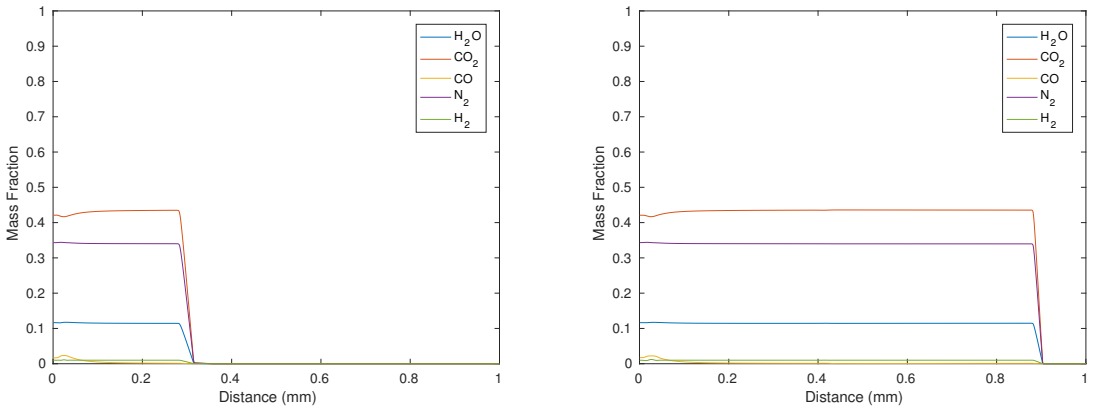

Figure 29. Final gaseous phase products H_2O, CO_2, CO, N_2 and H_2 mass fraction (Y_i) profiles using ARCIIST with a 1.0 km/s piston at (a) 0.125 and (b) 0.2 μs.

Most of the chemical species simply showed a rapid, linear production rate through the reaction zone followed by a level steady state. There are a few species, however, which showed some interesting developments. First, it is notable that before detonation is reached (0.125 μs), RDX has two distinct destruction rate slopes. The

shallower slope appeared immediately behind the leading shock wave. The sudden increase in destruction rate coincided with the location of the secondary wave front. It can be concluded that this location also marked the onset of Reaction 2 from Table 4. After detonation (0.2 μs), only the steeper destruction rate of RDX remained, indicating that both reaction mechanisms for RDX are instantly triggered by the detonation front. Furthermore, the trends present in the RDX mass fraction profiles directly correlate with those of the condensed phase volume fraction profiles. As expected, this indicates that the RDX destruction rate was the predominant factor in the phase transition process.

The behavior of HCN and CH_2O was more surprising. Unlike the CVTEX study conducted in Section 4.1, there was still HCN and CH_2O remaining after all of the reactions were completed. This behavior can be attributed to the dynamics present in MPEXS' one dimensional, shock driven simulation that were absent in the zero dimensional, thermally driven CVTEX study. In the CVTEX study, the rise in temperature was entirely caused by the exothermic reactions in the system. In MPEXS, changes in temperature were also affected by the hydrodynamics and shock interactions present in the system. The shock dynamics resulted in far more rapid increases in temperature and allowed the later reactions in the NRL model to initiate sooner.

Reviewing Table 4, NO_2 interacts with both HCN and CH_2O in Reactions 3 and 4. Examining the mass ratio profile of NO_2, it remained at approximately zero throughout the entire simulation. This observation indicates that NO_2 was being used at the same rate that it was created. Knowing that the system is being shocked to high temperatures, the remaining CH_2O suggests that Reaction 4 has dominated the system, using up all of the NO_2 before reactions with CH_2O could occur. Similarly, Reaction 7 becomes dominant over Reaction 5 and utilizes all of the NO before it

can react with HCN.

Since CH_2O was allocated to the condensed phase, the unreacted remainder had the unfortunate effect of halting the complete transition of the condensed phase to the gaseous phase within the MPEXS simulations. This consequence is clearly visible in the volume fraction profiles in Figure 25. Having any remaining part of the condensed phase post-detonation is a distinct difference from the simulations conducted using the SPD and SIG burn models, as will be shown in Section 6.2. However, since the condensed phase only takes up approximately 2% of the mixture volume in the region after following the reaction zone, the remaining CH_2O appears to have little effect on the other principle variables such as mixture temperature and pressure.

6.2 Comparison of ARCIIST to SPD and SIG

In Section 6.1, it was observed that the use of the ARCIIST technique in MPEXS resulted in simulations of RDX which properly captured the major features of shock initiated DDT. Furthermore, the steady detonation condition reached in these simulations resembled the ideal steady detonation from ZND theory and achieved the appropriate CJ conditions at the end of the reaction zone. Finally, the point of ignition, run-to-detonation distance, and magnitudes of the DDT features observed directly correlated to the initial impact pressure, determined by the choice of piston speed.

While these observations proved that ARCIIST was consistent within itself, it was important to compare the ARCIIST method with the common pressure-dependent burn models it was designed to replace. Figures 30 - 33 compare the profiles of the four primary variables for MPEXS simulations of RDX using ARCIIST, SPD, and SIG. The results compared in these figures were all taken from the 1.0 km/s piston speed cases. Of all the cases run, the run-to-detonation distance computed by all

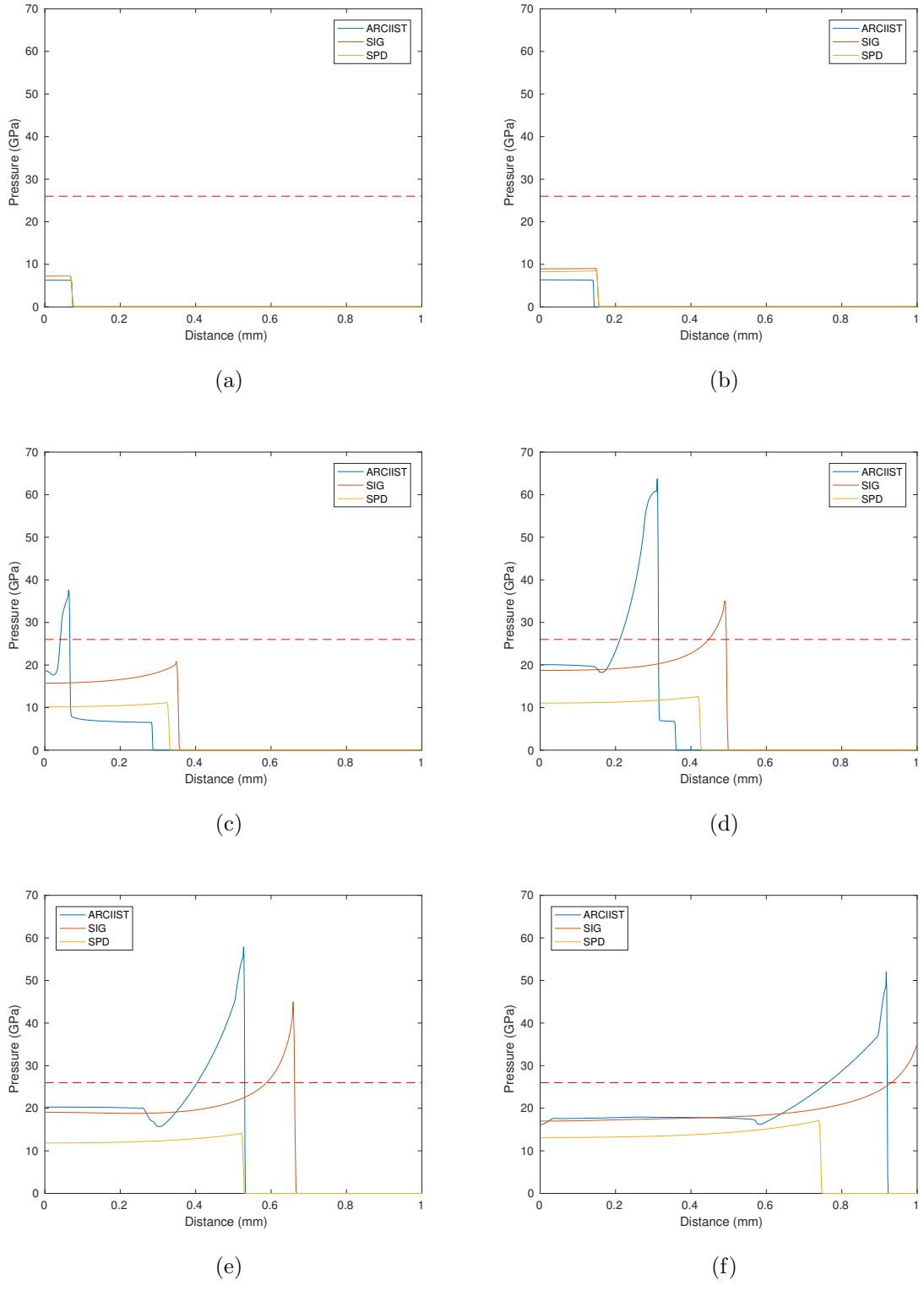

Figure 30. Comparison of RDX mixture pressure ($\overline{P}$) profiles using SPD, SIG, and ARCIIST with a 1.0 km/s piston at (a) 0.025**, (b)** 0.05**, (c)** 0.1**, (d)** 0.125**, (e)** 0.15**, and (f)** 0.2 μs**.**

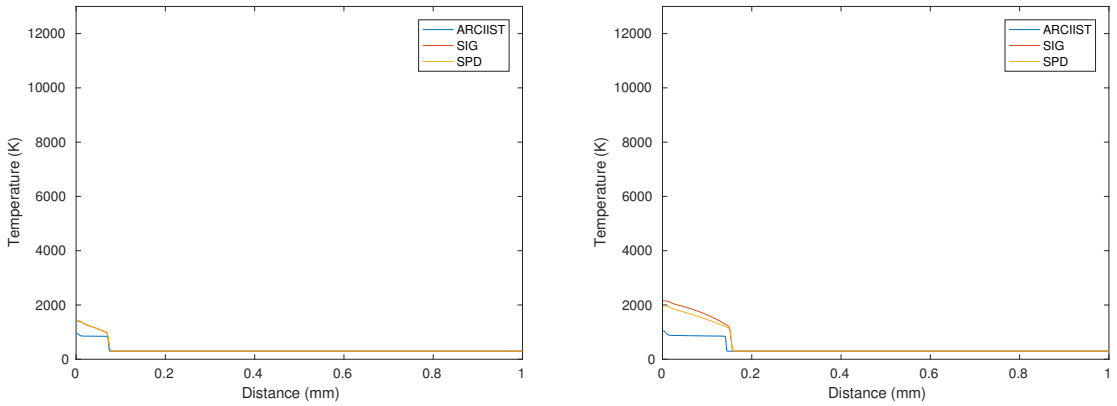

(a)

(b)

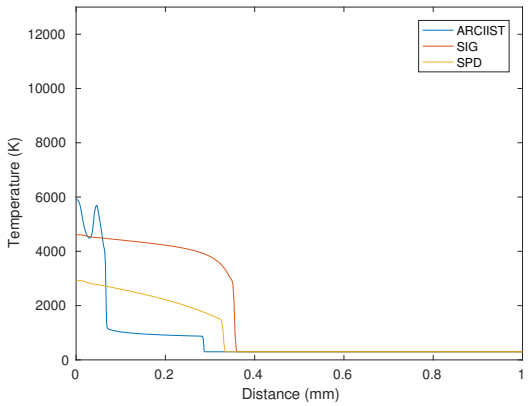

(c)

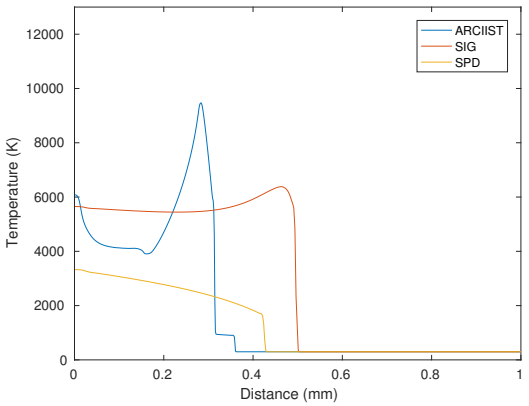

(d)

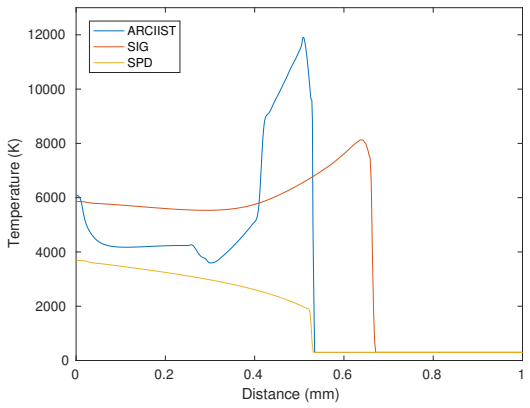

(e)

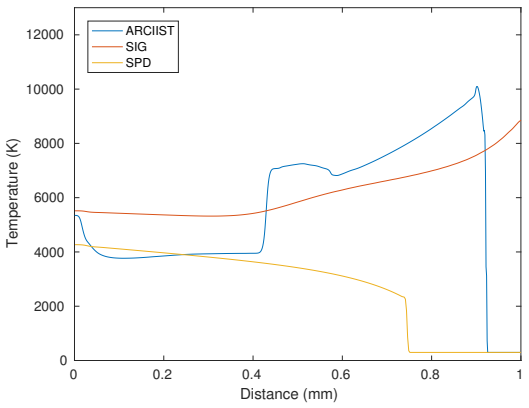

(f)

Figure 31. Comparison of RDX mixture temperature ($\overline{T}$) profiles using SPD, SIG, and ARCIIST with a 1.0 km/s piston at (a) 0.025**, (b)** 0.05**, (c)** 0.1**, (d)** 0.125**, (e)** 0.15**, and (f)** 0.2 μs**.**

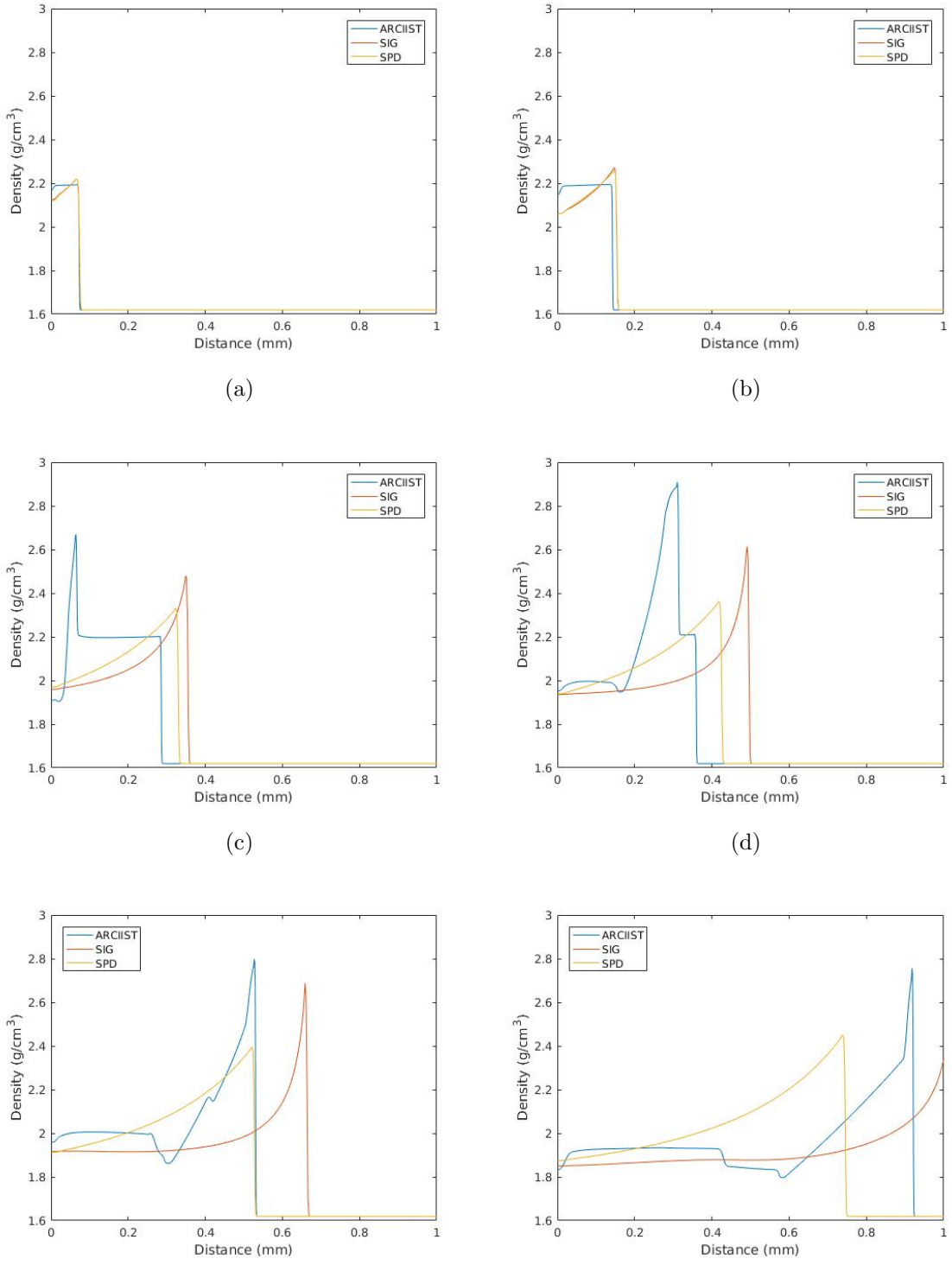

Figure 32. Comparison of RDX mixture density ($\overline{\rho}$) profiles using SPD, SIG, and ARCIIST with a 1.0 km/s piston at (a) 0.025**, (b)** 0.05**, (c)** 0.1**, (d)** 0.125**, (e)** 0.15**, and (f)** 0.2 μs**.**

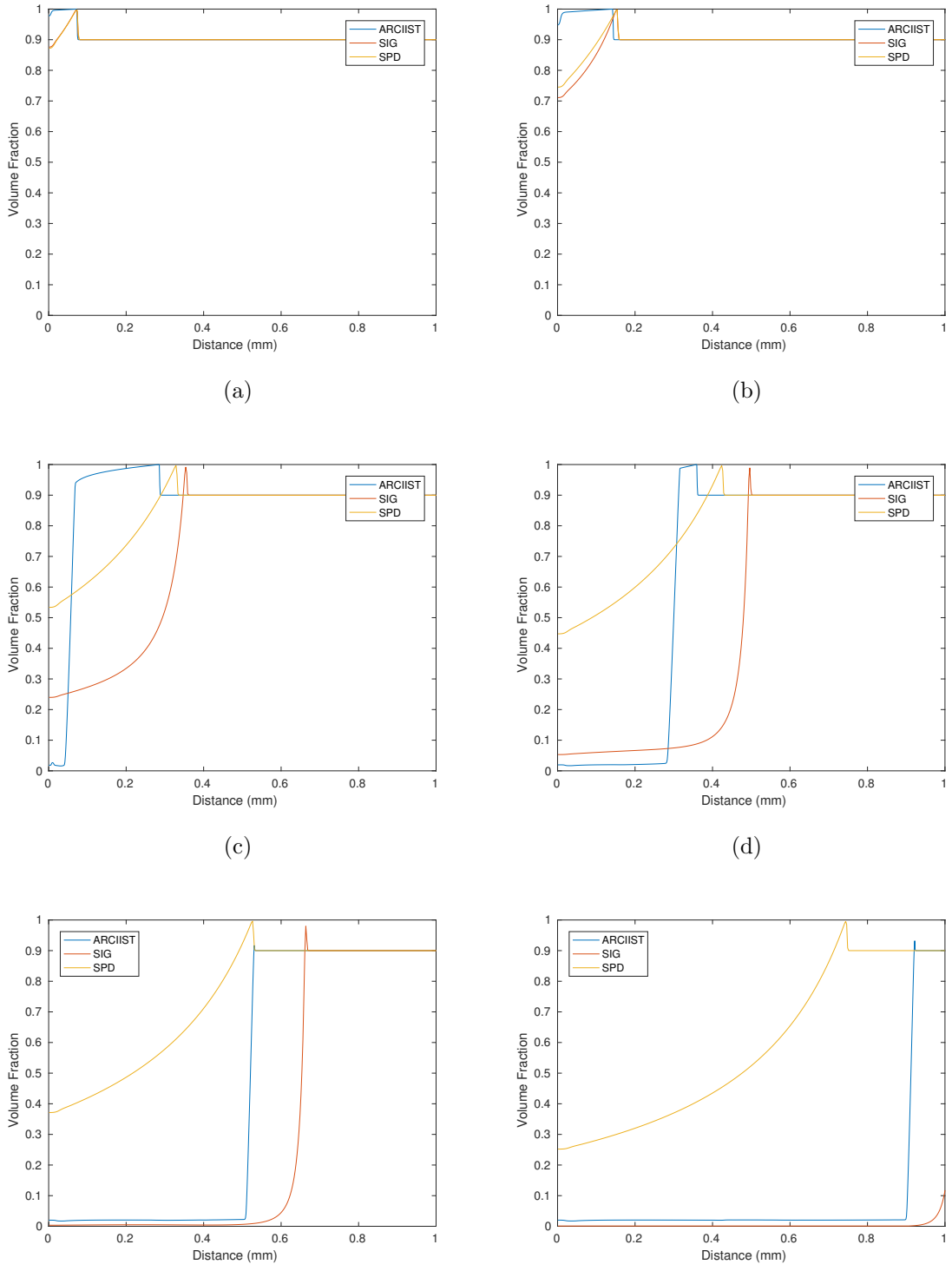

Figure 33. Comparison of RDX condensed phase volume fraction (ϕ_s) profiles using SPD, SIG, and ARCIIST with a 1.0 km/s piston at (a) 0.025**, (b)** 0.05**, (c)** 0.1**, (d)** 0.125**, (e)** 0.15**, and (f)** 0.2 μs**.**

three methods (particularly ARCIIST and SIG) were the closest to matching each other at this piston speed. Therefore, this was the best condition to compare the results of the three methods to each other.

In the first frame of the pressure profiles (0.025 μs), all three methods show a step function response in pressure from the initial shock wave. However, unlike ARCIIST, the results from the two burn models show bulk chemical reactions are already taking place. These reactions are visible in the steady increase of temperature, decrease in density, and decrease in condensed phase volume fraction seen behind the leading shock in the first frames of Figures 31 - 33.

Stepping through time, both the SPD and SIG show the leading shock front growing in strength. The SIG burn model shows this growth occurring exponentially until it reaches the steady state detonation condition visible in the fifth frame (0.15 μs). On the other hand, SPD shows this growth to be far slower. Furthermore, it should be noted that the SPD burn model has no upper limit and will continue to show growth of the leading shock strength for as long as the simulation is continued.

The key difference between the two burn models and the ARCIIST method is the lack of a secondary wave front. Because the two burn models are primarily based on the magnitude of the local system pressure, they simulate ignition as occurring as soon as the initial shock wave passes through condensed RDX. This also means that all of the simulated bulk chemical reactions and phase changes will always coincide with the location of the leading shock caused by the initial piston impact. Although this leading front is allowed to grow in strength, there is no clear point at which full detonation occurs. On the other hand, ARCIIST depends on thermal initiation of the NRL Arrhenius rate chemical model. This thermal dependence results in a delayed ignition followed by the rapid propagation of the secondary front until full detonation is reached. It will be shown in Section 6.3 that the delayed ignition modeled by

ARCIIST is a better representation of what has been observed in experimental data from shock initiated DDT in explosive samples. Thus, by basing the mass exchange rate on temperature dependent Arrhenius rate chemistry, ARCIIST has more accurately captured true DDT phenomenon which are missed by pressure-dependent burn models.

The pressure contour plots from the three methods are shown in Figure 34. The curvature in the plots for SPD and SIG indicate a gradual acceleration of the leading shock front. There is no distinct detonation point visible. In order to determine the

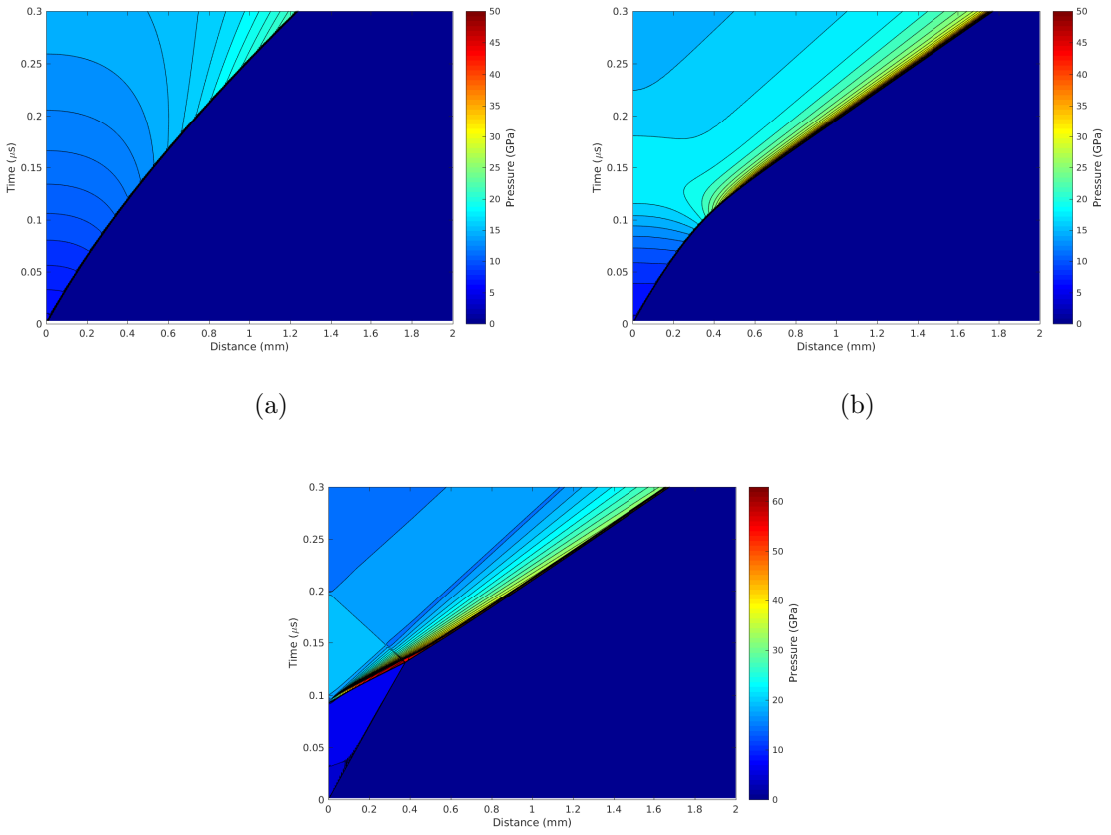

Figure 34. Pressure contour plot from an MPEXS simulation of RDX using (a) SPD, (b) SIG, and (c) ARCIIST. Piston speed was set to 1.0 km/s for all cases.

run-to-detonation location, a linear fit for the leading wave location was made for the earliest data points in the simulation. A linear fit was also made for the last data points in the simulation. The intersection of these two lines determined the run-to-detonation distance. Although the detonation point is more distinguishable using ARCIIST, use of the linear fit and intersection method further reinforced that the merging of the initial and secondary wave fronts simulated with ARCIIST was indeed the run-to-detonation location.

It should be noted that both ARCIIST and SIG eventually settled into steady state detonation waves of similar magnitude and velocity. The burn model simulations, however, concentrated all chemical reactions and inter-phase transitions at the location of the leading shock front. As a result, the use of pressure-dependent burn models washes over key DDT features. On the other hand, the use of ARCIIST demonstrated the ability to capture these critical phenomena for the first time in a macro-scale continuum hydrocode simulation.

6.3 Qualitative Comparisons with Experimental Data

In order to verify that the DDT features being captured using the ARCIIST technique were realistic, the results from the MPEXS simulations were compared to experimental data. Ideally, this comparison would have been made with empirical results using samples of either pure RDX or an RDX based PBX. Unfortunately, such data was not readily available. As an alternative, the simulations were compared to a study conducted by the Los Alamos National Laboratory (LANL) on the HMX based explosive LX-14 (95.5% HMX, 4.5% estane binder) [29]. Since both RDX and HMX are cyclonitramine exposives, their detonation behavior is similar even if the magnitudes of the individual variables is different.

Jones et. al. conducted their study by creating cylindrical samples of LX-14 with

an embedded electromagnetic particle velocity gauge package. An impactor was then shot into the samples at varying velocities. The LANL team recorded the evolving particle velocity changes at 10 discrete locations within the samples during shock induced DDT. The purpose of their experiment was to calibrate their Scales Uniform Ractive Front (SURF) inspired reactive burn scheme, a pressure dependent burn model which is calibrated based on the leading shock pressure instead of the local pressure like SPD and SIG. Their results are used here a means of verifying that the DDT features observed in the MPEXS simulations using ARCIIST are truly present in actual explosive detonations. Comparisons were also made to the simulated results using SIG to further identify the differences between the ARCIIST technique and pressure-dependent burn models.

The results of the LANL study have been reproduced with permission in Figure 35. Each colored line in the subfigures represents the data captured by a single velocity gauge. The noisy lines are experimental data, while the smooth, solid lines are numerical simulations using a SURF based numerical model calibrated for HMX explosives. The gauge locations relative to the initial impact location for each subfigure are listed in Table 13. In this table, u_p for the experimental data refers to the impactor velocity instead of piston velocity.

The particle velocity profiles in Figure 35 show the typical build up to detonation response in a pressed granular explosive sample. These profiles are characterized by a leading shock followed by a hump. In these experiments, both the hump and the shock increased in magnitude as they progressed deeper into the explosive. In all cases, the hump moved faster than the leading shock and eventually overtook it, marking the onset of detonation [29].

A post-processing tool was developed for MPEXS to display the output of a chosen variable as if it had been observed from a gauge in a set location relative to the

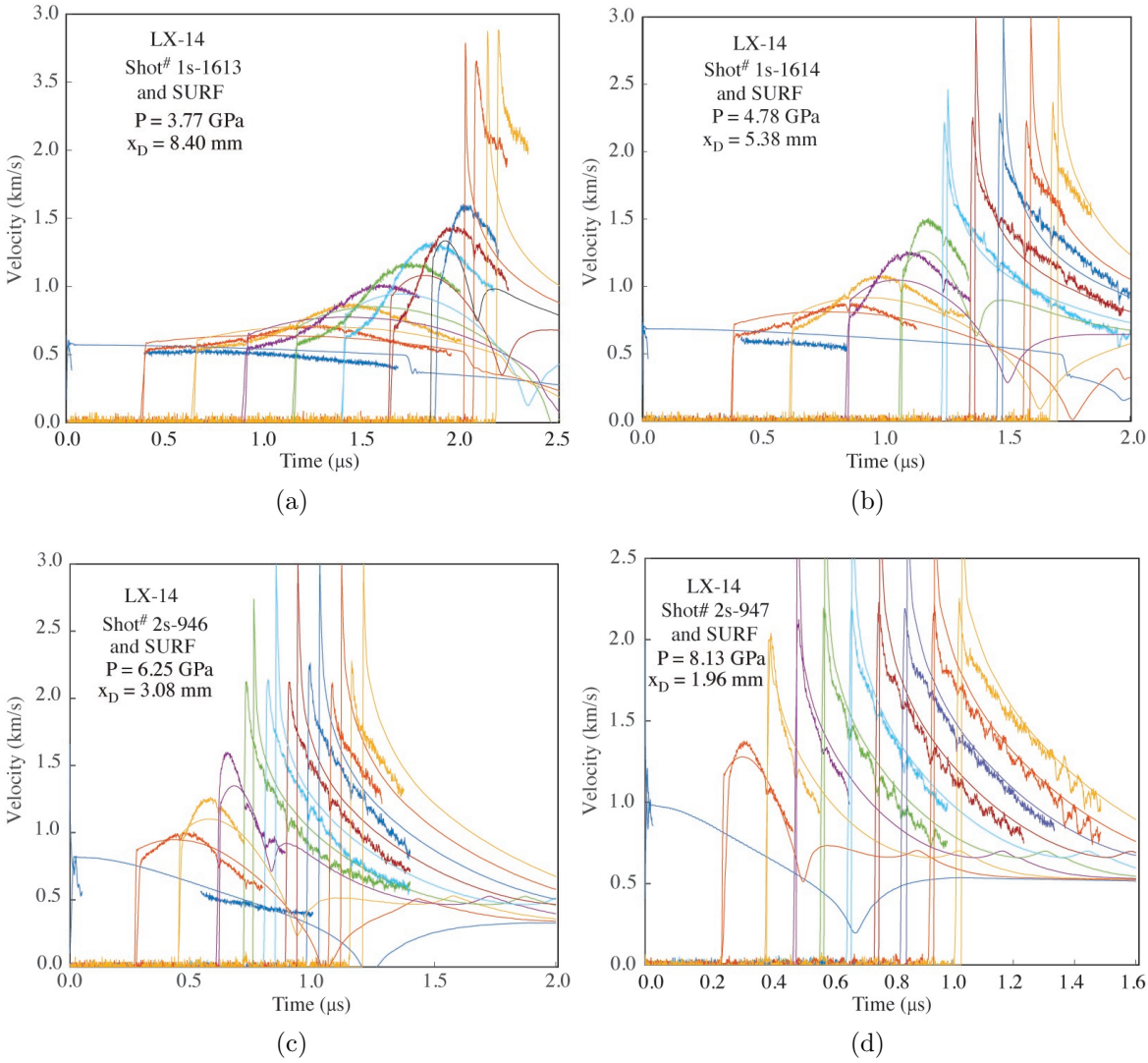

Figure 35. Particle velocity profiles for LANL LX-14 shock initiated experiments. The shot number, impact pressure, and measured run-to-detonation distance are listed on each corresponding set of profiles. Noisy lines are experimental data. Smooth, solid lines are numerical simulations using the SURF model. Gauge positions are listed in Table 13. These images are reproduced from [29].

piston's initial position. Figures 36 and 37 show the condensed phase particle velocity profiles for some of the MPEXS simulations using ARCIIST and SIG respectively. The piston speeds (u_p) and gauge locations for each subfigure are listed in Table 13. The simulated gauge locations were chosen to capture the critical DDT features.

The RDX simulations using ARCIIST, like the LX-14 experiments, showed an

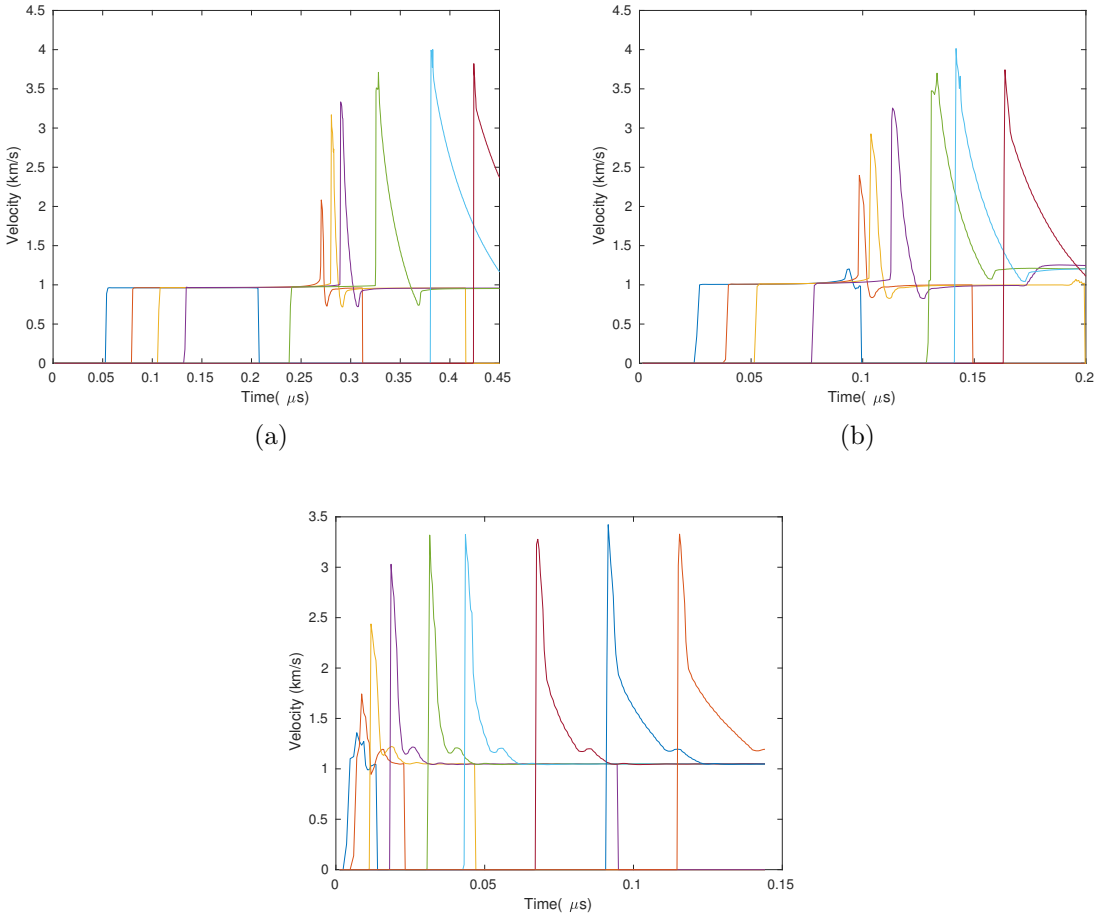

Figure 36. Particle velocity profiles for RDX simulated with MPEXS using ARCIIST. Gauge positions are listed in Table 13.

initial plateau in the particle velocity as the leading shock wave passes through the explosive. Also mirroring the experiments, the ARCIIST simulations showed the formation of a hump behind the shock front. While this hump was much more delayed and formed into a sharper peak, it must be remembered that this is a qualitative comparison of two different explosives over different time and length scale. Furthermore the long ignition delay and development of such a steep hump is strongly correlated to the small temperature band (800 - 1200 K) within the NRL chemistry model in which RDX transitions from ignition to its maximum decomposition rate. The 1.05

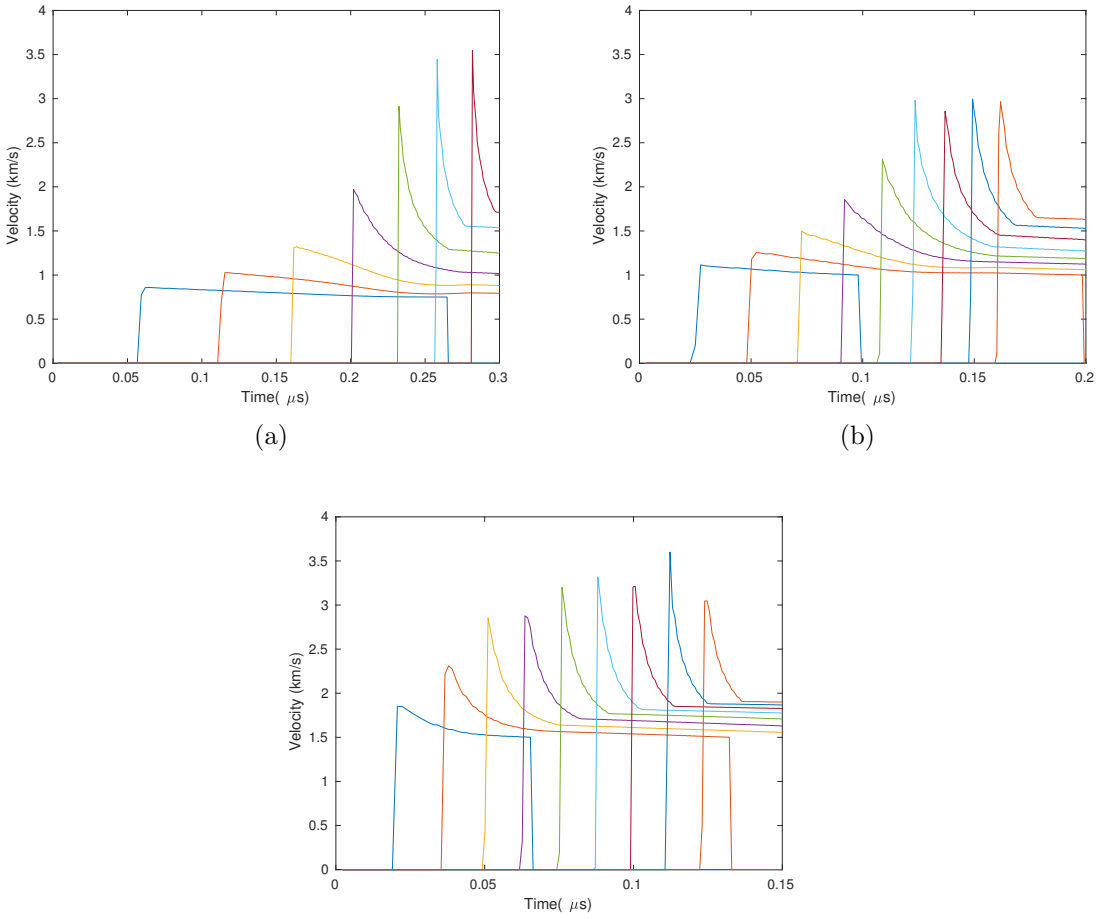

Figure 37. Particle velocity profiles for RDX simulated with MPEXS using SIG. Gauge positions are listed in Table 13.

km/s piston case appears to have the most similarities to the experimental results due to the relatively short delay between the passing of the initial impact shock and the start of ignition. The biggest difference between the features in the ARCIIST simulations and the LX-14 experiments is the lack of growth in the shock front itself.

The RDX simulations using SIG, on the other hand, showed far fewer similarities to the LX-14 experiments. Unlike ARCIIST, the SIG simulations did show a steady increase in the magnitude of the velocity profiles at the leading shock front. However, they completely failed to capture any development of a hump feature which

eventually overtakes the leading shock. As discussed in Section 6.2, this makes the identification of the run-to-detonation distance much more challenging when using common pressure-dependent burn models.

Although comparing simulations and experimental results for two different explosives is not ideal, this analysis does indicate that the incorporation of ARCIIST

Table 13. Gauge Positions Relative to Initial Impact Location

Test Method	Figure	u_p [km/s]	P_{impact} [GPa]	Gauge Position [mm]
LX-14: LANL Experiment	35a	0.646	3.77	0.0, 1.46, 2.44, 3.43, 4.41, 5.39, 6.38, 7.36, 8.35, 9.33
	35b	0.776	4.78	0.0, 1.48, 2.46, 3.45, 4.44, 5.43, 6.41, 7.40, 8.39, 9.38
	35c	1.661	6.25	0.0, 1.15, 1.94, 2.73, 3.52, 4.31, 5.09, 5.88, 6.67, 7.46
	35d	1.996	8.13	0.0, 1.18, 1.96, 2.75, 3.54, 4.32, 5.11, 5.90, 6.68, 7.47
RDX: MPEXS-ARCIIST	36a	0.96	7.07	0.2, 0.3, 0.4, 0.5, 0.9, 1.5, 1.9
	36b	1.0	7.49	0.1, 0.15, 0.2, 0.3, 0.5, 0.6, 0.8
	36c	1.05	8.02	0.015, 0.025, 0.05, 0.1, 0.2, 0.3, 0.5, 0.7, 0.9
RDX: MPEXS-SIG	37a	0.75	5.04	0.2, 0.4, 0.6, 0.8, 1.0, 1.2, 1.4, 1.6, 1.8
	37b	1.0	7.49	0.1, 0.2, 0.3, 0.4, 0.5, 0.6, 0.7, 0.8, 0.9
	37c	1.5	13.51	0.1, 0.2, 0.3, 0.4, 0.5, 0.6, 0.7, 0.8, 0.9

significantly improved the ability of MPEXS to capture realistic DDT features missed by more common burn models. Future work following this research should use the ARCIIST technique to simulate an explosive with a more extensive experimental data set. These efforts would help to further refine the accuracy of both the hydrocodes and chemistry models connected through the use of the ARCIIST technique.

6.4 Run-to-Detonation Analysis

In addition to verifying that using ARCIIST can properly capture the profiles of the key parameters during DDT, a study was conducted to see if the ARCIIST implementation in this research could capture the proper run-to-detonation characteristics of RDX. This study was accomplished by plotting the run-to-detonation distances for all of the ARCIIST simulations on a Pop-Plot in the same manner used in Section 5.2 during the SPD and SIG burn model calibration. Figure 38 displays the ARCIIST results along with the run-to-detonation from the SPD and SIG. Experimental data for PBX-9405 and PBX-9407 are also included to compare the simulated trends with those of actual RDX based explosive samples.

As observed in Section 5.2, the SIG simulations did a far better job than SPD of matching the slopes of PBX-9405 and PBX-9407. In fact, the SPD shows no correlation between input shock pressure and run-to-detonation distance when such a correlation is known to exist in all explosive compounds. Combined with its limited potential to correctly simulate the profiles of the key parameters as shown in Section 6.2, the SPD burn model appears to be of little utility in simulating DDT processes in RDX. While the SIG simulations nearly match the results of PBX-9407, it should also be remembered that it was calibrated in order to achieve that effect.

In Sections 6.2 and 6.3 the ARCIIST technique proved to be better than the two pressure-dependent burn models in capturing realistic DDT features in the key

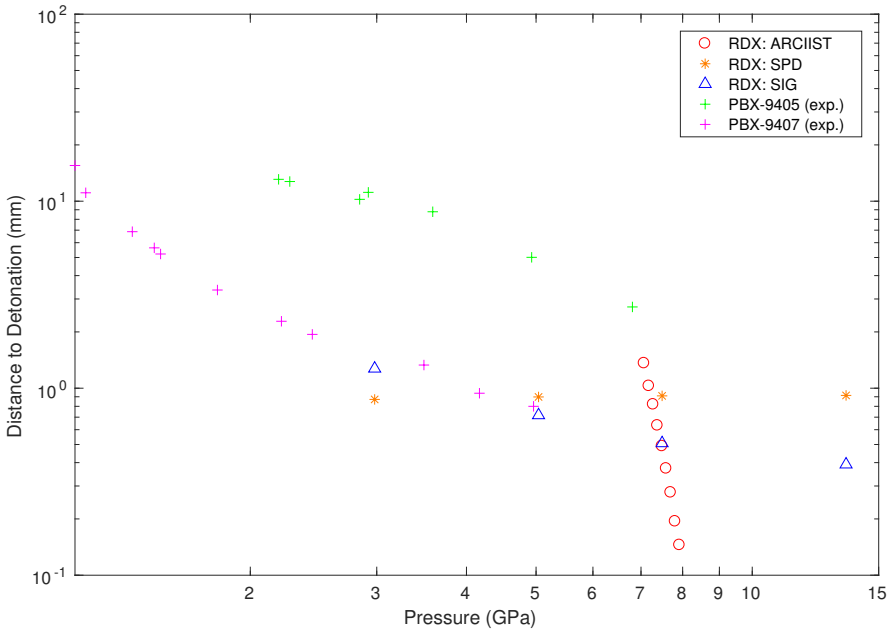

Figure 38. Pop-Plot comparison of all MPEXS RDX simulations with experimental data for PBX-9405 and PBX-9407

parameter profiles. Therefore, it was surprising to discover how far off the steep run-to-detonation trend from the ARCIIST simulations was from the two RDX based PBXs. The steep slope did explain why detonation was never observed in the 0.5 and 0.75 km/s piston cases. Following the tend line of the ARCIIST data in Figure 38, these two data point would be well above the upper limits of the plot and would have required an unreasonably large computational domain to capture. Conversely, the calculations for the 1.05 through 1.5 km/s piston cases found the run-to-detonation distance to be less than one cell length and approaching zero. These three points were well below the vertical limits of the current Pop-Plot and were left off of the Figure 38 in order to make better comparisons with the PBX and burn model data.

The near vertical trend in the ARCIIST data suggests that RDX is highly insensitive to shock initiated detonation. However, this is highly unlikely. PBX-9405 and PBX-9407 are heterogeneous explosives composed of 93.7% and 94% RDX respec-

tively. While the inclusion of plastic binders has been shown to alter the detonation properties of a particular explosive, the variances are never as drastic as the ARCIIST simulations would suggest [14] [21]. Instead, the run-to-detonation results suggest that by replacing the burn models with ARCIIST, a vital piece of information has inadvertently been omitted from the simulation.

As discussed in Section 6.3, the ARCIIST simulations demonstrated a long delay between passage of the initial shock and the point of ignition. This delay was especially apparent in the lower piston speed cases. The LX-14 experimental data, on the other hand, showed a much more gradual development of the hump feature behind the initial shock front. These observations suggest that there may be an issue with ignition sensitivity modeled by ARCIIST in this research.

It is widely accepted that shock initiation of packed, granular explosives is caused by the formation of hot-spots due to micro-structural properties. The properties consist of the collapsing of voids between grains, inter-granular interaction, and defects within the crystal structure itself [54]. Furthermore, there is a correlation between the grain size and the sensitivity of the packed explosive. Larger grain sizes and larger voids between grains require lower shock strength to initiate detonation in and explosive. Conversely, the more tightly packed an explosive sample is, the more resistant it is to shock initiation [35].

Although MPEXS tracks the properties of the condensed and gaseous phases separately, it is still a continuum based hydrocode. Ultimately, it views the mixture in each individual cell of the domain as one continuous material; perfectly mixed with no defects. Therefore, MPEXS has no inherent way of modeling the formation and influence of hot-spots on the ignition of an explosive. Any explosive modeled by MPEXS, or any other continuum hydrocode, should exhibit properties of an explosive material which is highly insensitive to shock initiation. However, this was never a

factor when an empirically derived burn model was used in MPEXS. As previously mentioned, the burn models are calibrated to match experimental Pop-Plot data. Because the explosives used in the experiments contained micro-structural defects, they exhibited hot-spot based ignition in their results. Thus, the empirically based burn models implicitly account for the average hot spot effects and add that level of fidelity into the MPEXS model. By removing the calibration of the mass exchange rate to experimental data, it is assumed that ARCIIST has inadvertently removed the modeling of hot spot based ignition from MPEXS.

6.5 Ignition Sensitivity Study

In Section 6.4, it was observed that MPEXS improperly models RDX as an explosive insensitive to shock initiation when using the ARCIIST implementation developed in this research. This insensitivity was most likely due to the fact that MPEXS does not explicitly model micro-structural ignition mechanisms such as voids or crystal damage which could cause hot spots to form. On the other hand, MPEXS simulations in this research and all previous research efforts which used burn models did not display this insensitivity to shock initiation. Because the burn models themselves were based on empirical run-to-detonation data, the micro-structural ignition mechanisms were implicitly modeled and were automatically included in the mass transition rate between the condensed and gaseous phases.

In order to test the assumption that the incorporation of ARCIIST inadvertently removed information on micro-structural ignition mechanisms from the MPEXS simulations, a method was developed to increase the ignition sensitivity within the mass exchange rate subroutine. Equation 53 was added to Step 1 of the mass exchange rate computation described in Figure 10.

$$T_{IS} = T_s + \phi_s \Psi \quad \text{if } \overline{P} > 1 \text{ GPa} \tag{53}$$

In this equation, an arbitrary ignition sensitivity factor (Ψ) is added to the condensed phase temperature of a cell. The new, higher temperature (T_{IS}) is then sent to the Cantera subroutines in place of T_s in Step 1. By raising the temperature seen in the Arrhenius rate calculations, ignition is forced to occur sooner than previously observed in the simulations using ARCIIST. It should be noted that Equation 53 only takes effect if the mixture pressure ($\overline{P}$) in a cell is above 1 GPa. This restriction prevents ignition from occurring until after the initial shock wave has passed through the cell in question. Furthermore, since the purpose of Equation 53 is to identify the influence of micro-structural mechanics on ignition, ignition sensitivity factor (Ψ) is multiplied by ϕ_s. In this way, the influence of the sensitivity factor is reduced as the condensed phase transition to the gaseous phase. Thus, the loss of any micro-structure ignition mechanisms as the condense phase decomposes is represented in the system.

Equation 53 was developed for the sole purpose of testing the ignition sensitivity of MPEXS while using ARCIIST. It is not based on, nor does it truly simulate actual micro-structural phenomenon. The goal of the ignition sensitivity study discussed in this section was to prove that the integration of ARCIIST into MPEXS had removed key ignition mechanism information from the system. It does not, however, definitively identify what was removed.

Two sensitivity factors were tested in this study. The factors and the associated piston speeds chosen for each simulation are listed in Table 14. In total, six simulations were run using the increased sensitivity scheme described by Equation 53.

The run-to-detonation results from this study are displayed in Figure 39 along with the results from the original ARCIIST runs. As expected, by artificially increasing

Table 14. Supplemental ARCIIST Test Matrix for Ignition Sensitivity Study

Ignition Sensitivity Factor (Ψ) [K]	u_p [km/s]
200	0.75, 0.8, 0.85
400	0.45, 0.5, 0.55

the temperature seen in the Cantera subroutines, ignition of the condensed phase was observed in simulations with piston speeds much lower than those in the original ARCIIST study. As a result, detonation was also able to occur in a shorter distance for these lower piston speeds. This overall decrease in the run-to-detonation distance can be seen in the shallower slopes of the increased sensitivity data series as compared to the original ARCIIST data. Furthermore, as the sensitivity factor was increased, the slope began to fall more in line with the data for PBX-9405 and PBX-9407. These trends lend credibility to the assumption that the implementation of ARCIIST removed the implicit ignition information present in empirically based burn models.

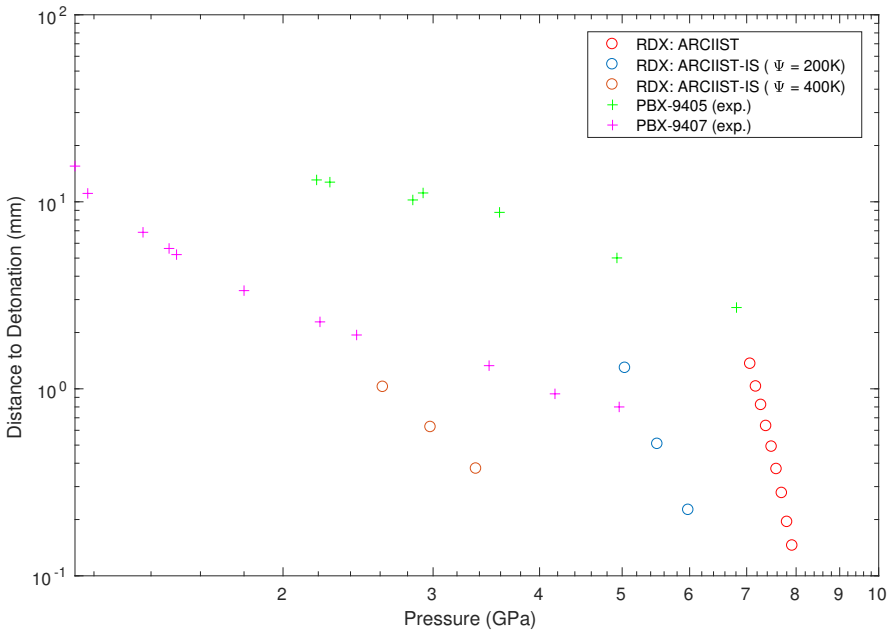

Figure 39. Pop-Plot comparison of ARCIIST Ignition Sensitivity Study simulations with experimental data for PBX-9405 and PBX-9407

Larger ignition sensitivity factors were attempted. However, these resulted in unrealistically chaotic profiles of the key mixture variables. This development was due to the fact that Equation 53 only affects the temperature visible to the Cantera subroutines conducting the micro-scale chemical computations. The increased temperature was not present in the macro-scale hydrodynamic computations in the main MPEXS subroutines. For ignition sensitivity factors over 400 K, this discontinuity between the two simulation levels resulted in jerky increases and decreases in the mass exchange rate between phases and created more chaotic and unrealistic wave forms within the macro-scale simulation domain.

Even with the discontinuity effects, the two ignition sensitivity factors tested in this study demonstrated a relatively smooth DDT as seen in the mixture pressure profile examples shown in Figures 40 and 41. In fact, these cases had a more distributed development of the secondary wave resulting in a rounder pressure wave profile in the early part of the simulation. This development was more consistent with DDT theory than the more spiked secondary waves from the original ARCIIST implementation results.

Furthermore, increasing the ignition sensitivity resulted in particle velocity profiles which more closely resembled the LX-14 results in Section 6.3. As shown in two examples in Figure 42, more rounded hump features behind the initial shock front were observed in the simulations run with increased ignition sensitivity than those run with ARCIIST alone. The simulated velocity gauge locations for the examples in Figure 42 are listed in Table 15. The improved similarities to experimental results when using the increased sensitivity scheme further supports the assumption that the use of ARCIIST alone removes important ignition information from the simulations.

Additional research needs to be conducted to develop a statistical hot spot model. This model should ideally be introduced as a source term in the energy equations of

MPEXS and would increase the internal energy of the condensed phase in a manner proportional to the average size and number of hot spots observed in common explosives. Inclusion of such a hot spot model would complement and greatly increase the utility of the ARCIIST technique in macro-scale explosive hydrocodes.

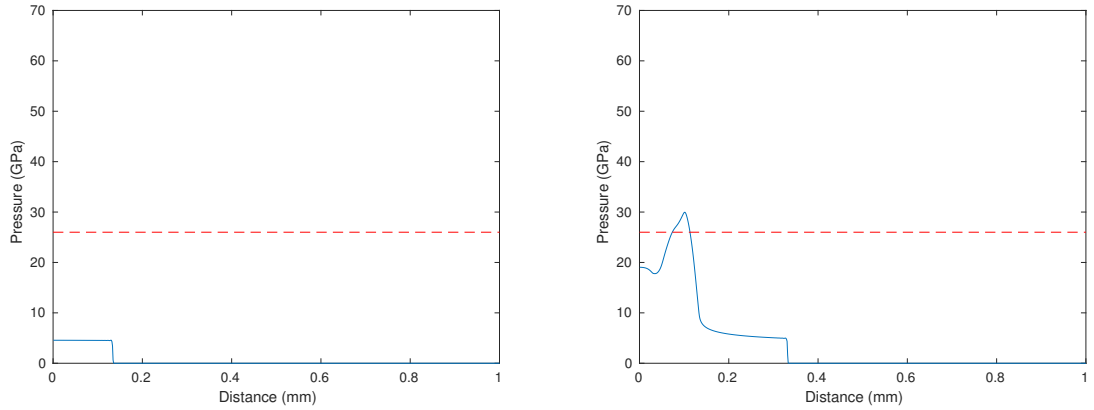

(a)

(b)

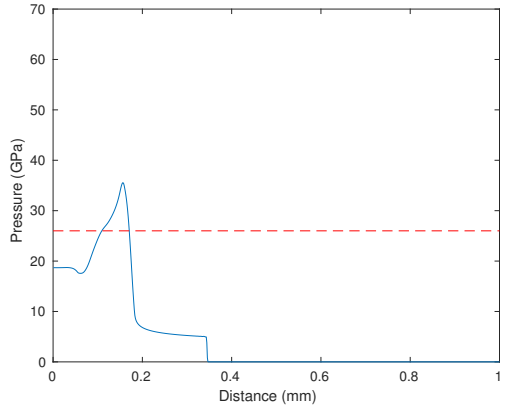

(c)

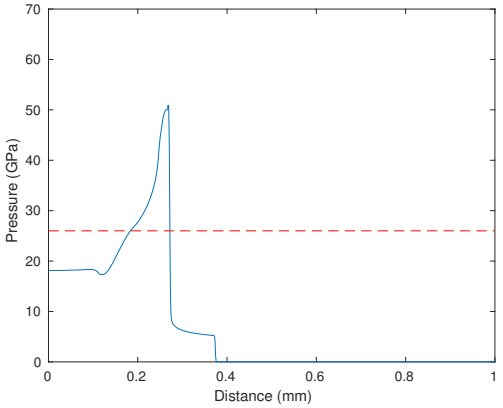

(d)

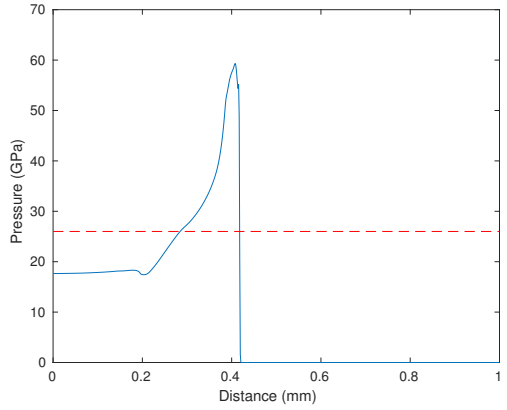

(e)

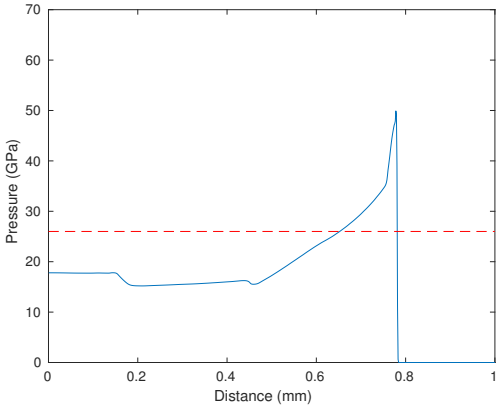

(f)

Figure 40. RDX mixture pressure ($\overline{P}$) profiles for the $\psi = 200K$ ignition sensitivity study using ARCIIST with a 0.8 km/s piston at (a) 0.05**, (b)** 0.125**, (c)** 0.13**, (d)** 0.14**, (e)** 0.155**, and (f)** 0.2 μs**.**

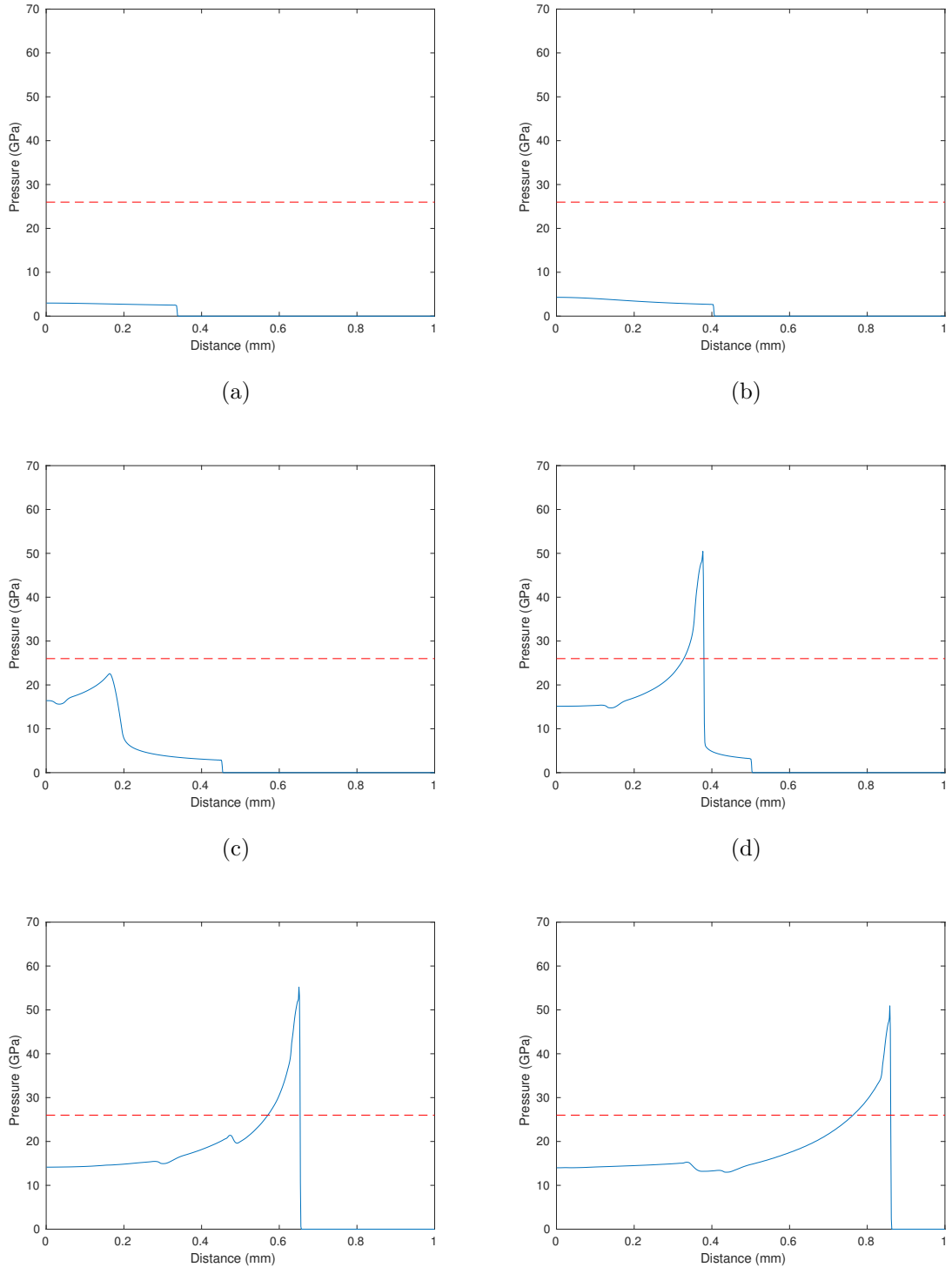

Figure 41. RDX mixture pressure ($\overline{P}$) profiles for the $\psi = 400K$ ignition sensitivity study using ARCIIST with a 0.5 km/s piston at (a) 0.15, (b) 0.18, (c) 0.2, (d) 0.22, (e) 0.25, and (f) 0.275 μs.

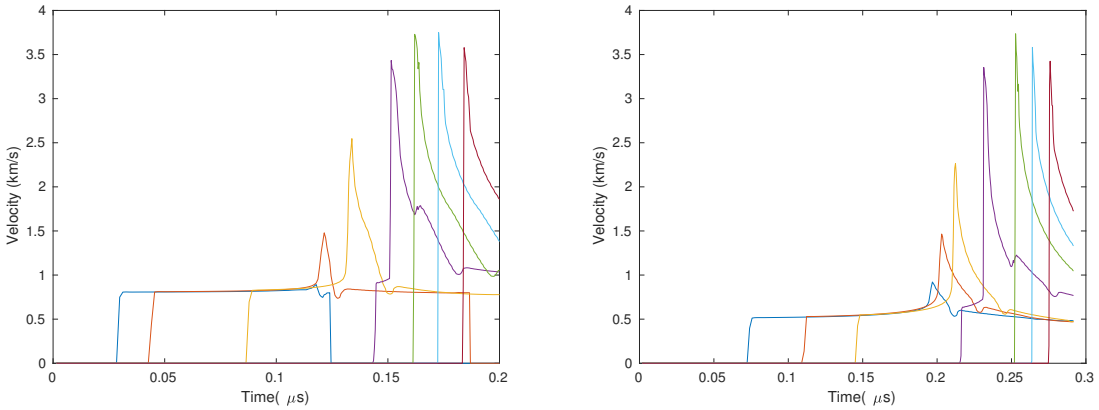

(a) (b)

Figure 42. RDX Particle velocity profiles from the ARCIIST ignition sensitivity study. Gauge positions and simulation parameters are listed in Table 15.

Table 15. Ignition Sensitivity Study Gauge Positions Relative to Initial Impact Location

Test Method	Figure	u_p [km/s]	P_{impact} [GPa]	Gauge Position [mm]
MPEXS-ARCIIST $\psi = 200K$	42a	0.8	5.5	0.1, 0.15, 0.3, 0.5, 0.6, 0.7, 0.8
MPEXS-ARCIIST $\psi = 400K$	42b	0.5	2.98	0.2, 0.3, 0.4, 0.6, 0.8, 0.9, 1.0

VII. Conclusions

Through the course of this research, it has been established that determining the reaction rate of an explosive material under varying conditions is critical to designing hydrocodes capable of simulating deflagration to detonation transition (DDT). Until now, the state of the art for macro-scale hydrocodes was to use one of numerous burn models. These burn models are designed to estimate the bulk chemical reaction rate. Unfortunately, they are largely based on empirical data and must be recalibrated for every new material being simulated. While these calibration methods are well established, they require full synthesis of the explosive before any simulations can be made. This requirement has prevented macro-scale simulations of detonations from becoming more predictive in characterizing new explosive material formulations.

The focus of this research was to reduce the reliance of macro-scale explosive hydrocodes on existing empirical data. This goal was accomplished by replacing common burn models with an Arrhenius rate reacting chemistry model. The Arrhenius Rate Chemistry Informed Inter-Phase Source Term (ARCIIST) technique was developed to create an interface between a series of micro-scale, zero-dimension constant volume thermal explosion (CVTEX) simulations and a macro-scale hydrocode. The information from the CVTEX simulations was used to determine the mass transition rate between the condensed and gaseous phases of a reacting explosive. By integrating this information into a macro-scale hydrocode, the simulation was transformed into a simultaneous multi-scale computation, greatly increasing its capacity to capture the complex physical features of DDT.

ARCIIST was tested by incorporating an Arrhenius reacting chemistry model developed for the cyclic-nitramine RDX by the Naval Research Laboratory (NRL) into the Air Force Research Laboratory's (AFRL) Multi-Phase Explosive Simulation (MPEXS) continuum hydrocode. Due to limitations within the NRL chemistry model

itself, a temperature splitting and capping scheme was employed in order to prevent exponential increases in the mass exchange rate between phases from destabilizing the macro-scale computations. This issue has been discussed with the NRL and efforts are being taken to create an extended Arrhenius rate form of the RDX chemistry model. Once completed, this new model should be self-limiting and the temperature capping may be removed from the current ARCIIST implementation. It is recommended that all future investigations using the ARCIIST technique should use an extended Arrhenius rate model for the explosive being simulated. This format will not only provide better numerical stability, it should also improve the accuracy of the results.

MPEXS simulations of RDX using ARCIIST have been compared to identical simulations using more common, pressure dependent burn models. Results indicate that, through the use of ARCIIST, MPEXS can more accurately capture the complexities of an explosive undergoing shock initiated DDT. For the first time, macro-scale hydrocode captured the formation of the secondary wave structure of a DDT event through the incorporation of fundamental chemistry. This key feature in the transition to detonation is overlooked when using pressure-dependent burn models. These results were verified through qualitative comparisons with empirical data from LX-14 experiments. Furthermore, the pressure profiles of the ARCIIST simulation post-detonation aligned more closely with ZND detonation theory than those produced from simulations using burn models.

Additionally, the run-to-detonation distances computed by the MPEXS simulations of RDX were compared with experimental data for two RDX based Polymer-Bonded Explosives (PBX), PBX-9405 and PBX-9407. The results from the series of simulations run using the ARCIIST technique showed RDX to be uncharacteristically insensitive to shock initiated detonation. The results using a Simple Ignition and Growth (SIG) burn model, on the other hand, were nearly in line with the exper-

imental data for PBX-9407. When using ARCIIST, a significant delay was observed between the passage of the initial shock wave and ignition of the condensed explosive. Based on this observation, it was theorized that the implementation of ARCIIST conducted in this research had inadvertently removed potential micro-structural ignition mechanisms such as hot spots from the MPEXS simulations. Since the pressure dependent burn models used in this research were calibrated to experimental data, the average effects of the micro-structural ignition mechanisms were implicitly included within these models. The NRL chemistry model, on the other hand, does not account for such ignition methods. Thus, when using ARCIIST, MPEXS imperfectly modeled RDX to be insensitive to shock initiated detonation. An ignition sensitivity study was conducted, verifying the theory that the use of ARCIIST removed ignition mechanisms which were implicit to empirical burn models. It is recommended that future research efforts should be devoted to developing a statistical hot spot model. Such a model should be introduced as a source term in the energy equations and should be a function of the average size and number of hot spots in a particular explosive. A micro-structural ignition model of this form would compliment the use of ARCIIST in macro-scale hydrocodes.

Even with its limitations, the ARCIIST technique has successfully linked micro-scale chemical kinetics of the NRL Arrhenius rate model of RDX to macro-scale hydrodynamics of AFRL's MPEXS code. Through the development of this chemically based, temperature dependent technique for computing the mass exchange rate between phases, the ARCIIST technique has incorporated the fundamental observation that the decomposition of energetic materials is temperature based, not pressure based, in a macro-scale simulation. Furthermore, it demonstrated the ability to more accurately capture critical features of DDT which are missed through the use of burn models. This unique capability was accomplished without tailoring the model to fit

experimental results. Additionally, since the NRL chemistry model is based largely on theoretical chemistry, the development of ARCIIST has created a pathway towards the creation of predictive macro-scale models which do not require the physical synthesis of an explosive material.

APPENDICES

A. Additional EOS Validation Data

This appendix contains all of the data referenced in Section 5.1. Figures 43 through 46 show the evolution of the pressure and volume fraction profiles for the simulations conducted to validate the EOS parameters chosen to represent RDX. The solid green line (—) in these figures represents the P_{CJ} for RDX with an initial density of 1.6 g/cm^3. The dashed green line (- - -) shows the expected post-shock pressure from analysis of the non-reacting RDX Hugoniot [14]. Since MPEXS uses a piston attached reference frame, the distances in these figures represents the position in front of the piston at a snap shot in time.

In the early stages of the simulations, the chemical reaction has not yet taken off and the pressure response overall is very close to the expected non-reacting Hugoniot response. This subfigure suggests that the parameters chosen for the Mie-Gruneisen EOS are valid. As time progresses, the pressure at the wave front builds towards and eventually surpassing P_{CJ}.

In final frames, the leading shock front has stabilized. As expected, at the shock front the pressure jumps up past P_{CJ}, capturing the magnitude of the Von Neumann spike. Behind the front pressure rapidly relaxes down through P_{CJ} approximately at the point where the volume fraction of condensed RDX is approximately zero; the end of the reaction zone. This observation suggests that the parameters chosen for the JWL EOS is also behaving properly.

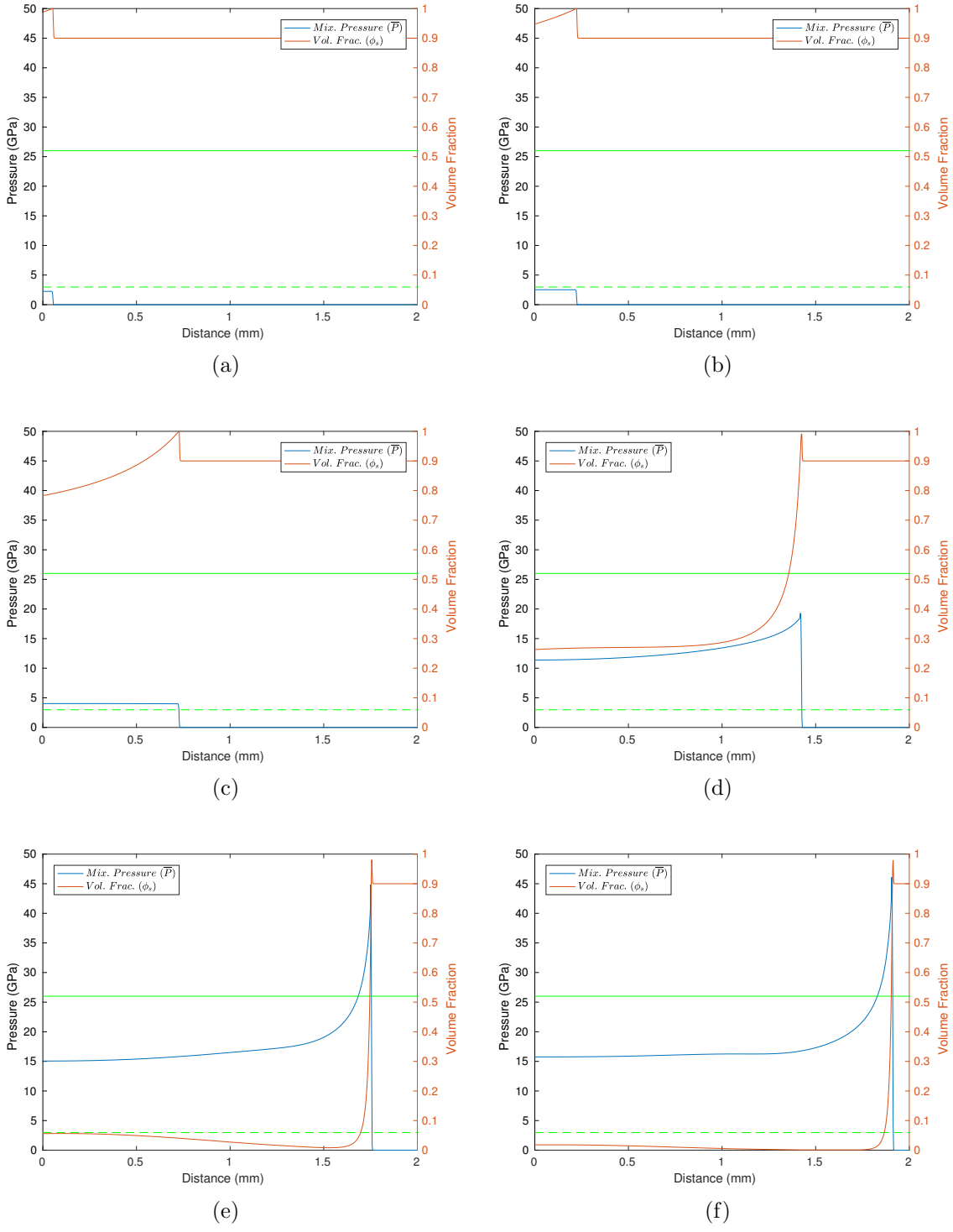

Figure 43. RDX mixture pressure ($\overline{P}$) and condensed phase volume fraction (ϕ_s) profiles using the SIG burn model and 0.5 km/s piston at (a) 0.025, (b) 0.1, (c) 0.3, (d) 0.5, (e) 0.55, and (f) 0.57 μs. The dashed green line (- - -) represents expected response from the non-reacting RDX Hugoniot and the solid green line (—) represents RDX CJ pressure.

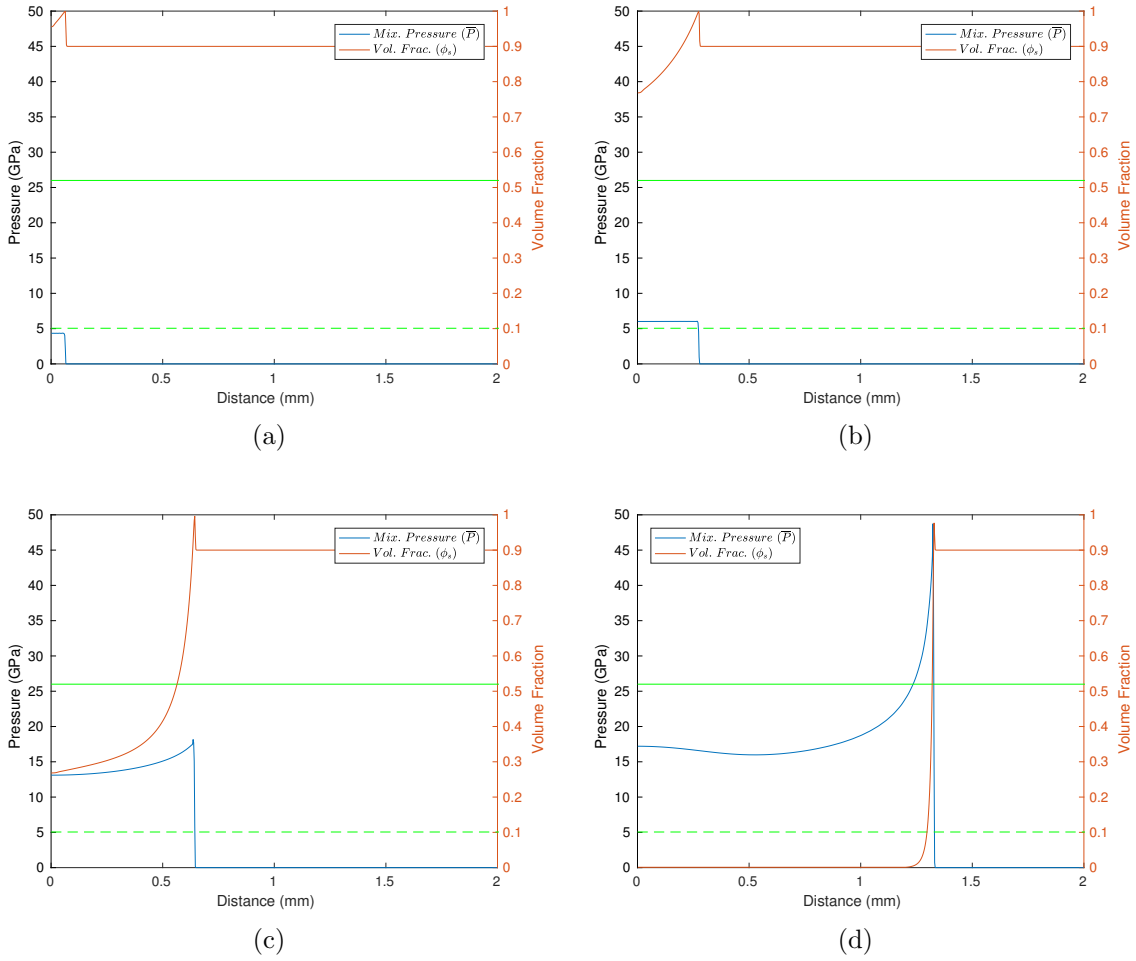

Figure 44. RDX mixture pressure ($\overline{P}$) and condensed phase volume fraction (ϕ_s) profiles using the SIG burn model and 0.75 km/s piston at (a) 0.025, (b) 0.1, (c) 0.2, and (d) 0.3 μs. The dashed green line (- - -) represents expected response from the non-reacting RDX Hugoniot and the solid green line (—) represents RDX CJ pressure.

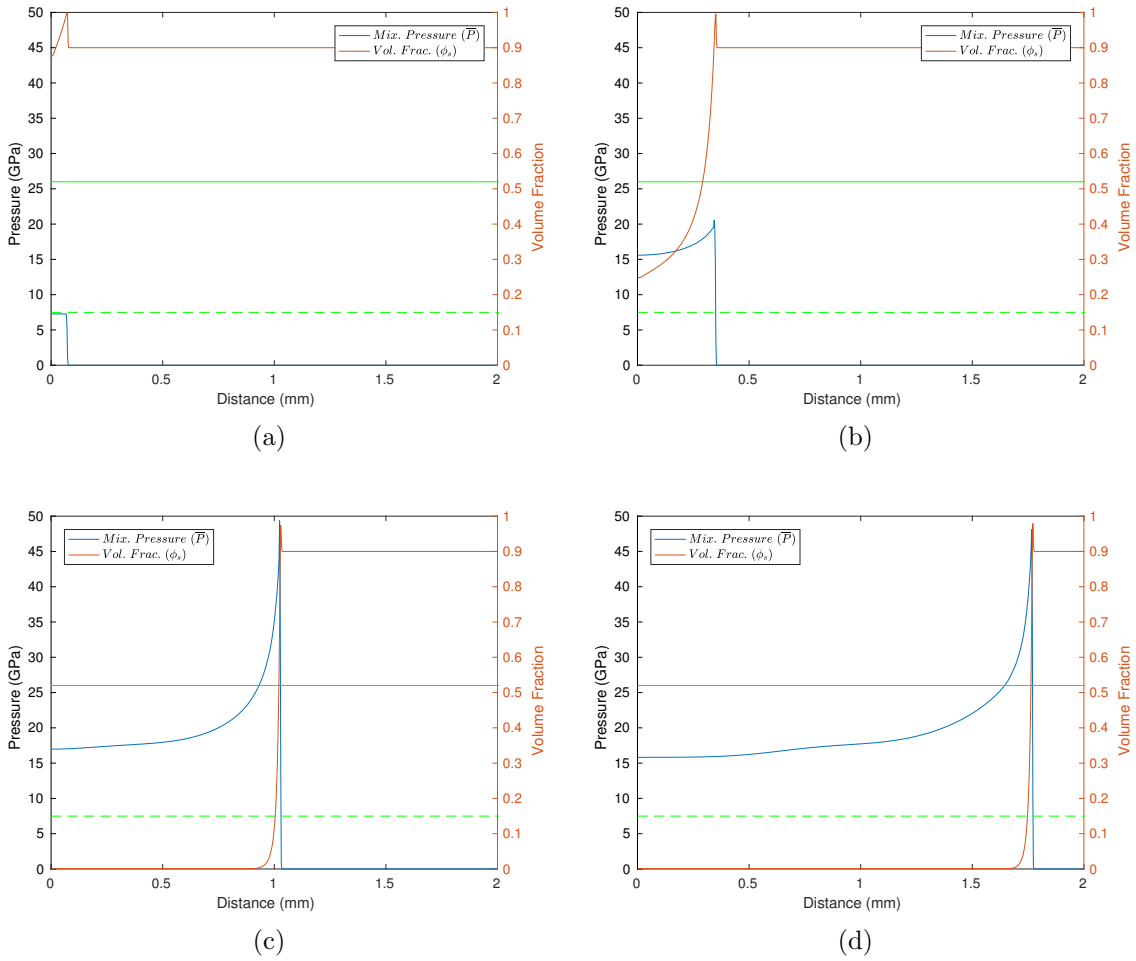

Figure 45. RDX mixture pressure ($\overline{P}$) and condensed phase volume fraction (ϕ_s) profiles using the SIG burn model and 1 km/s piston at (a) 0.025, (b) 0.1, (c) 0.2, and (d) 0.3 μs. The dashed green line (- - -) represents expected response from the non-reacting RDX Hugoniot and the solid green line (—) represents RDX CJ pressure.

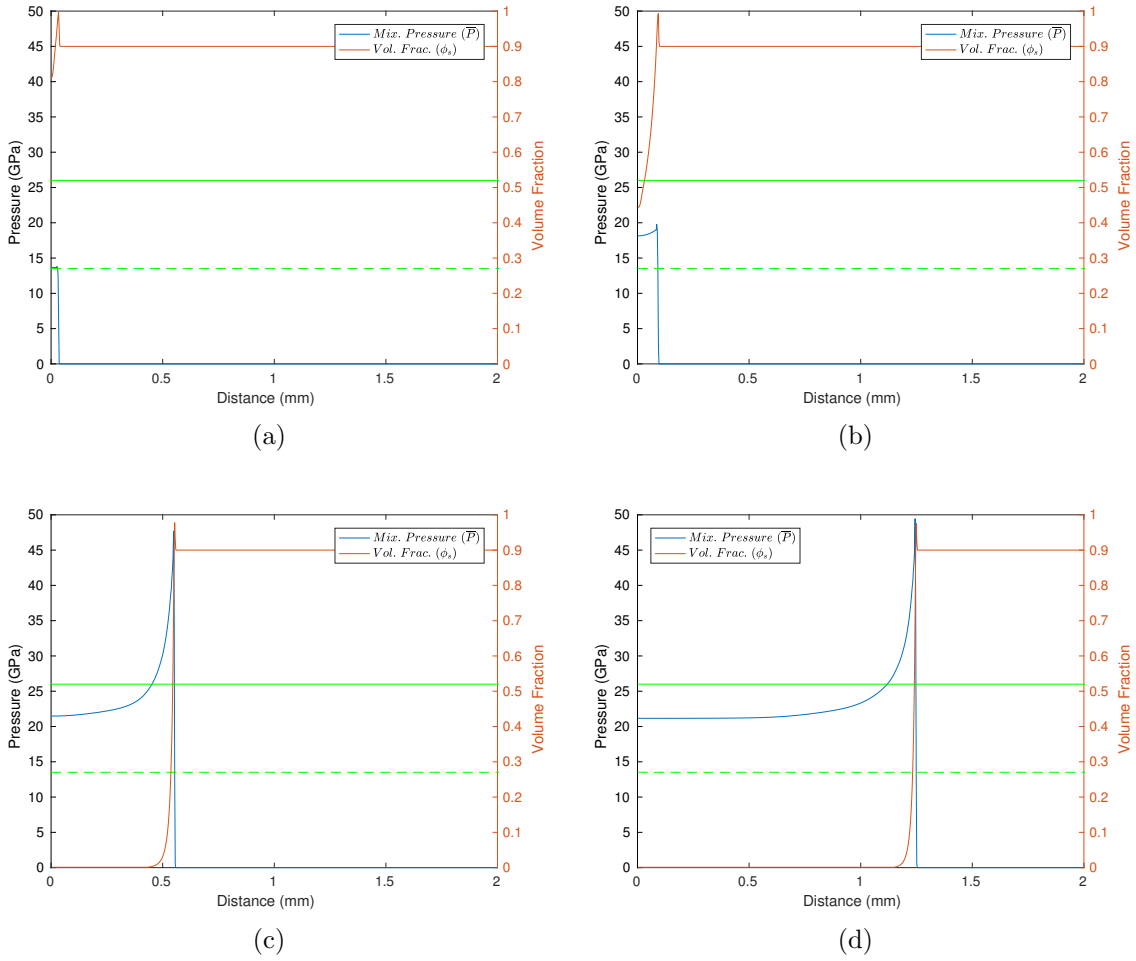

Figure 46. RDX mixture pressure ($\overline{P}$) and condensed phase volume fraction (ϕ_s) profiles using the SIG burn model and 1.5 km/s piston at (a) 0.01, (b) 0.025, (c) 0.1, and (d) 0.2 μs. The dashed green line (- - -) represents expected response from the non-reacting RDX Hugoniot and the solid green line (—) represents RDX CJ pressure.

B. Additional Temporal and Spatial Refinement Data

This appendix contains all of the SIG refinement data referenced in Section 5.3

B.1 Temporal Refinement

The temporal refinement study conducted with SIG used the initial conditions and parameters shown in Table 16. Four simulations were run, each with a different CFL conditions. These conditions are shown in Table 17 along with the corresponding average time step size from each simulation. The results of this study are shown in Figures 47 - 50. These figures show the profiles for mixture pressure ($\overline{P}$), mixture temperature ($\overline{T}$), mixture density ($\overline{\rho}$) and the condensed phase volume fraction (ϕ_s) at two snapshots in time.

Table 16. Initial Conditions for Temporal Refinement with SIG

ρ_s $[g/cm^3]$	ϕ_s	$\overline{\rho}$ $[g/cm^3]$	P $[GPa]$	T $[K]$	u_p $[km/s]$
1.8	0.9	1.6	1.013E-4	300	1.0

Table 17. CFL Conditions for Temporal Refinement with SIG

CFL	$Average\ \Delta t$ $[\mu s]$
0.2	2.5 x 10^{-5}
0.5	6.2 x 10^{-5}
1.0	12.0 x 10^{-5}
2.0	22.7 x 10^{-5}

There were no distinguishable differences observed in the profiles of the four primary variables in Figures 47 - 50 or the run-to-detonation distance. It was decided that a CFL of 1.0 would be used for all tests using SIG to be consistent with ARCIIST runs.

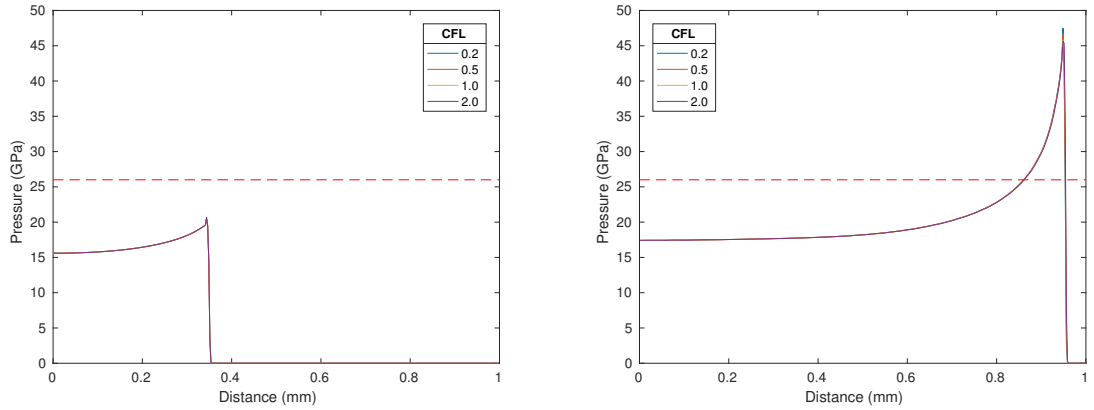

(a) (b)

Figure 47. Temporal Refinement of MPEXS with SIG: Mixture pressure ($\overline{P}$) profiles at (a) $0.1\mu s$ and (b) $0.19\mu s$. The (- - -) line represents RDX CJ pressure. Piston speed of 1 km/s used in all cases.

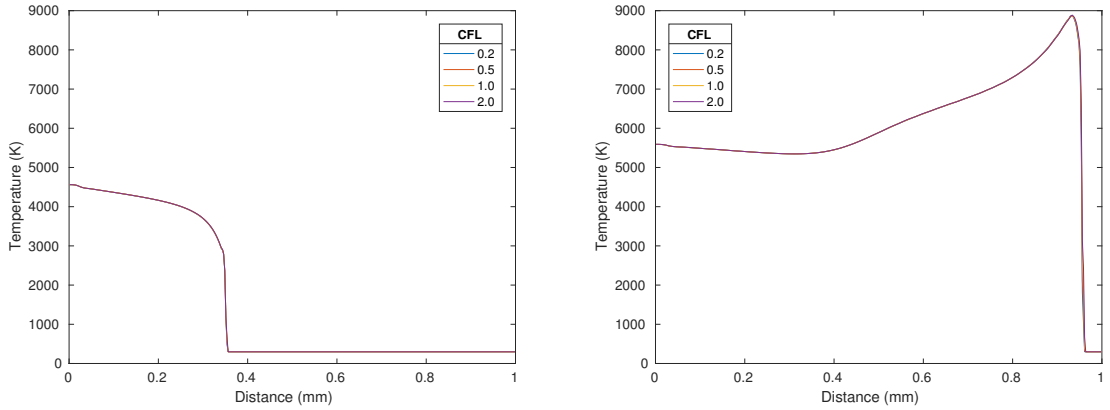

(a) (b)

Figure 48. Temporal Refinement of MPEXS with SIG: Mixture temperature ($\overline{T}$) profiles at (a) $0.1\mu s$ and (b) $0.19\mu s$. Piston speed of 1 km/s used in all cases.

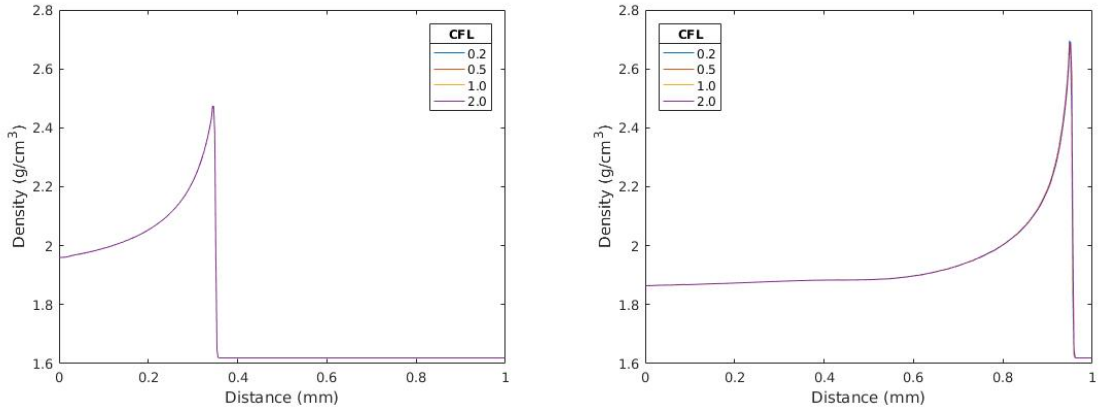

Figure 49. Temporal Refinement of MPEXS with SIG: Mixture density ($\overline{\rho}$) profiles at (a) $0.1\mu s$ and (b) $0.19\mu s$. Piston speed of 1 km/s used in all cases.

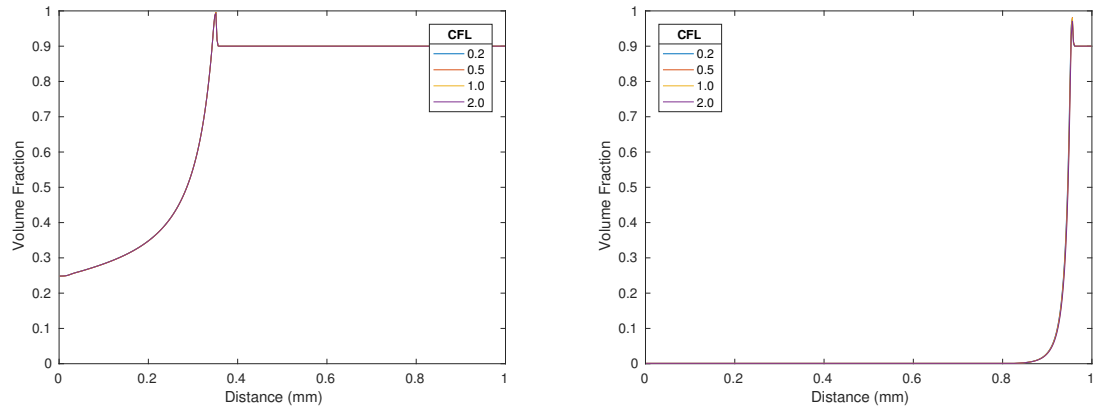

Figure 50. Temporal Refinement of MPEXS with SIG: Condensed phase volume fraction (ϕ_s) profiles at (a) $0.1\mu s$ and (b) $0.19\mu s$. Piston speed of 1 km/s used in all cases.

B.2 Spatial Refinement

Table 18 shows initial conditions and refinement levels tested for the spatial refinement study conducted using SIG. This study conducted in similar fashion as the

temporal refinement study. The results of this study are shown in Figures 51 - 54. As with the temporal refinement study, there were few distinguishable differences observed in the profiles of the four primary variables or the run-to-detonation distance. For this reason, a N_x of 400 cell per mm was chosen for all SIG simulations.

Table 18. Initial Conditions for Spatial Refinement with SIG

ρ_s $[g/cm^3]$	ϕ_s	$\overline{\rho}$ $[g/cm^3]$	P $[GPa]$	T $[K]$	u_p $[km/s]$	N_x $[cells/mm]$
1.8	0.9	1.6	1.013E-4	300	1.0	400, 800, 1600

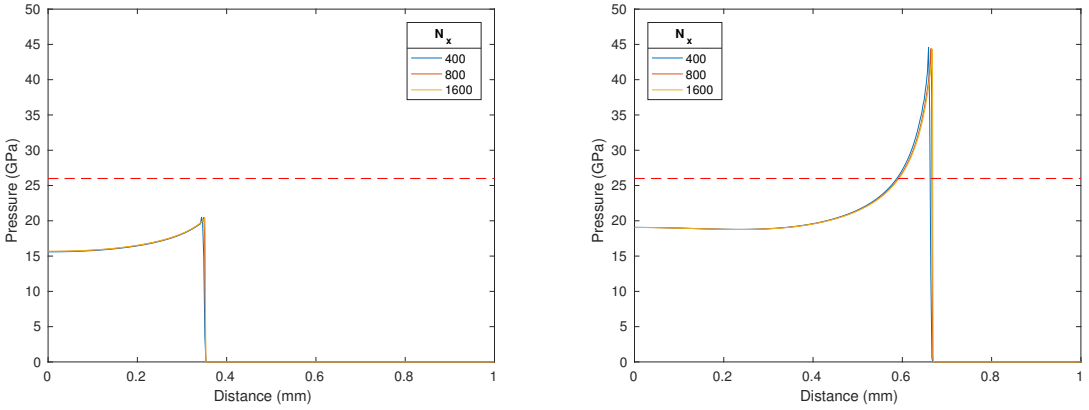

Figure 51. Spatial Refinement of MPEXS with SIG: Mixture pressure ($\overline{P}$) profiles at (a) $0.1\mu s$ and (b) $0.15\mu s$. The dashed red line (- - -) represents RDX CJ pressure. Piston speed of 1 km/s used in all cases.

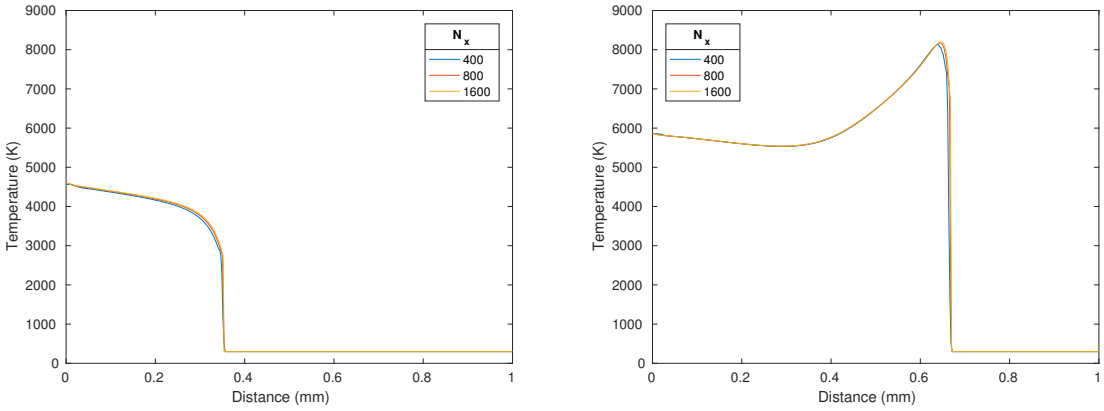

(a) (b)

Figure 52. Spatial Refinement of MPEXS with SIG: Mixture temperature ($\overline{T}$) profiles at (a) $0.1\mu s$ and (b) $0.15\mu s$. Piston speed of 1 km/s used in all cases.

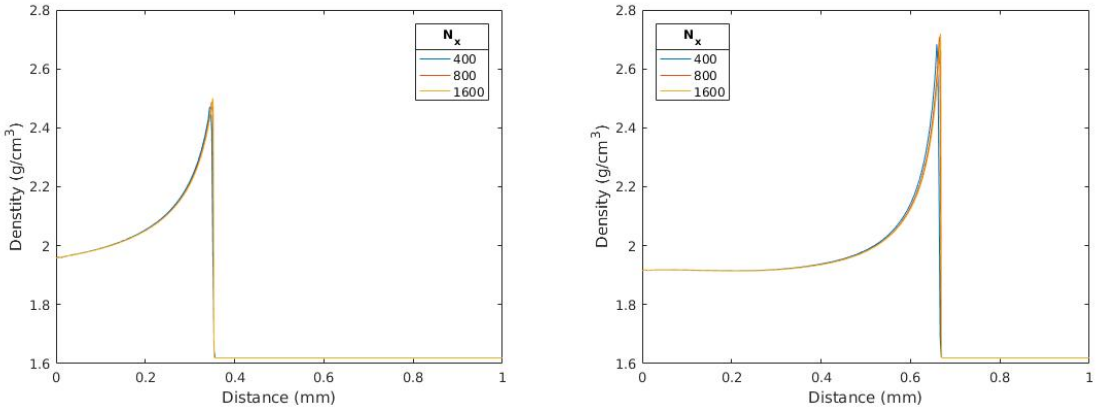

(a) (b)

Figure 53. Spatial Refinement of MPEXS with SIG: Mixture density ($\overline{\rho}$) profiles at (a) $0.1\mu s$ and (b) $0.15\mu s$. Piston speed of 1 km/s used in all cases.

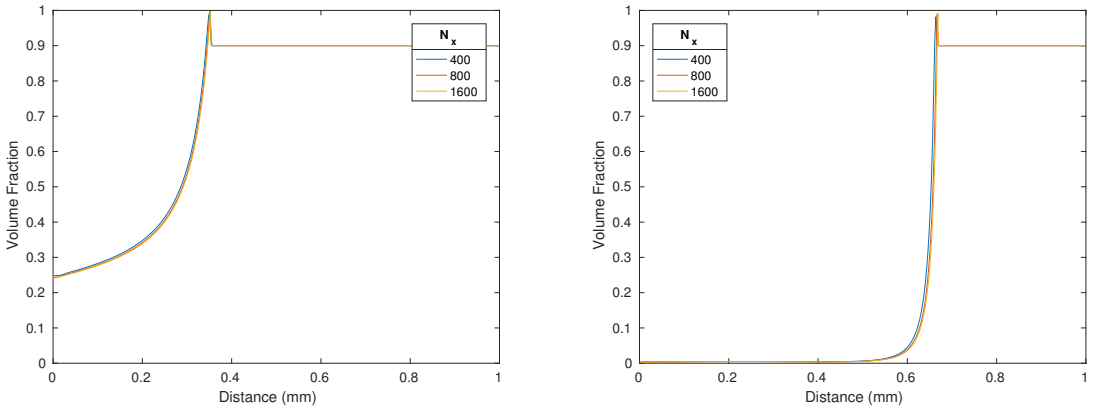

(a) (b)

Figure 54. Spatial Refinement of MPEXS with SIG: Condensed phase volume fraction (ϕ_s) profiles at (a) $0.1\mu s$ and (b) $0.15\mu s$. Piston speed of 1 km/s used in all cases.

C. Additional ARCIIST Simulation Results

This appendix contains the additional examples from the MPEXS simulations of RDX using ARCIIST referenced in Section 6.1. Profile plots of the four primary variables for the 0.96 km/s piston case are shown in Figures 55 - 58. Similarly, profile plots for the 1.2 km/s piston case are shown in Figures 60 - 63. Pressure contour plots for the 0.96 and 1.2 km/s piston cases are shown in Figures 59 and 64 respectively.

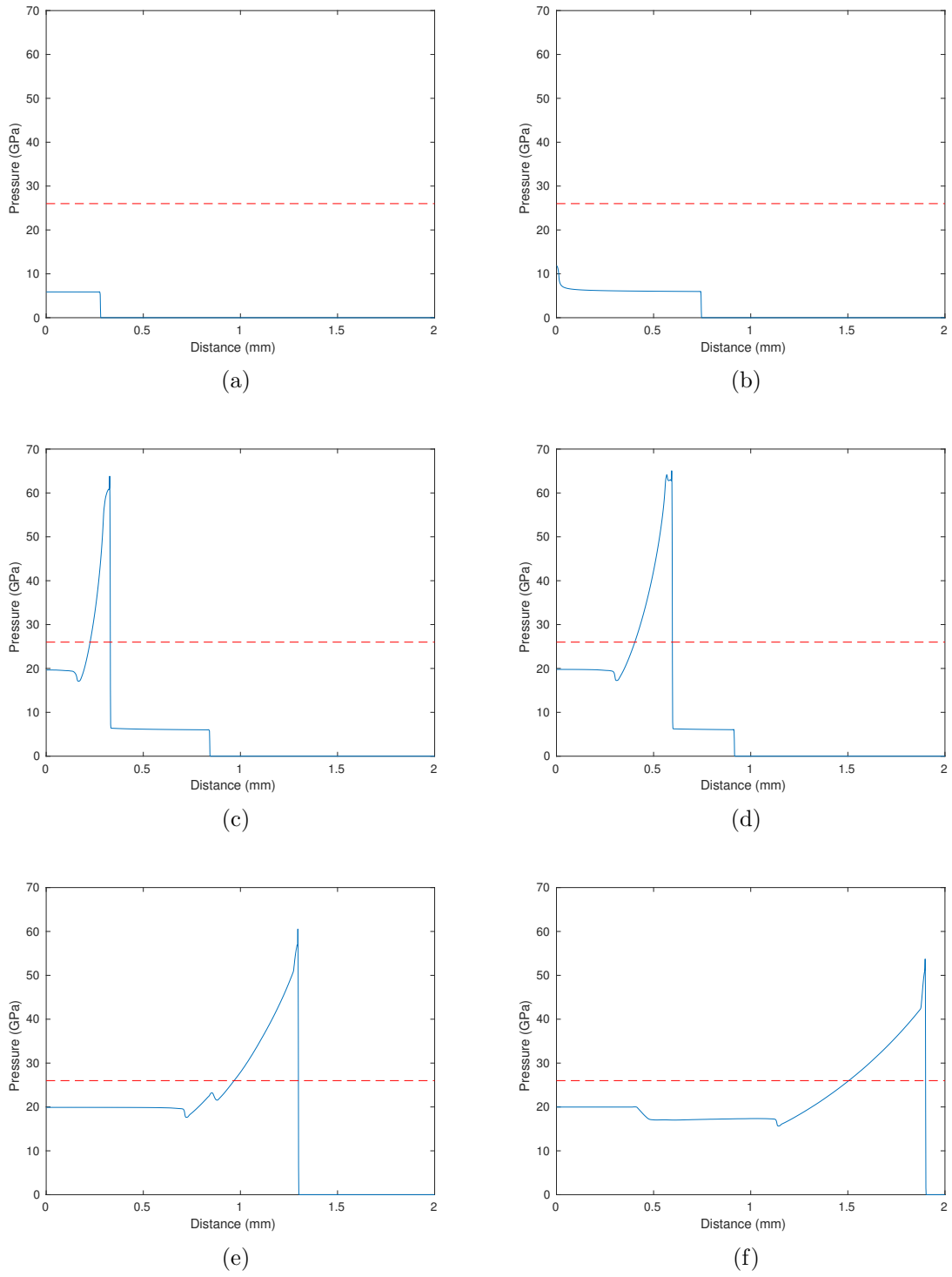

Figure 55. RDX mixture pressure ($\overline{P}$) profiles using ARCIIST with a 0.96 km/s piston at (a) 0.1**, (b)** 0.265**, (c)** 0.3**, (d)** 0.325**, (e)** 0.4**, and (f)** 0.475 μs**. The dashed red line (- - -) represents RDX CJ pressure.**

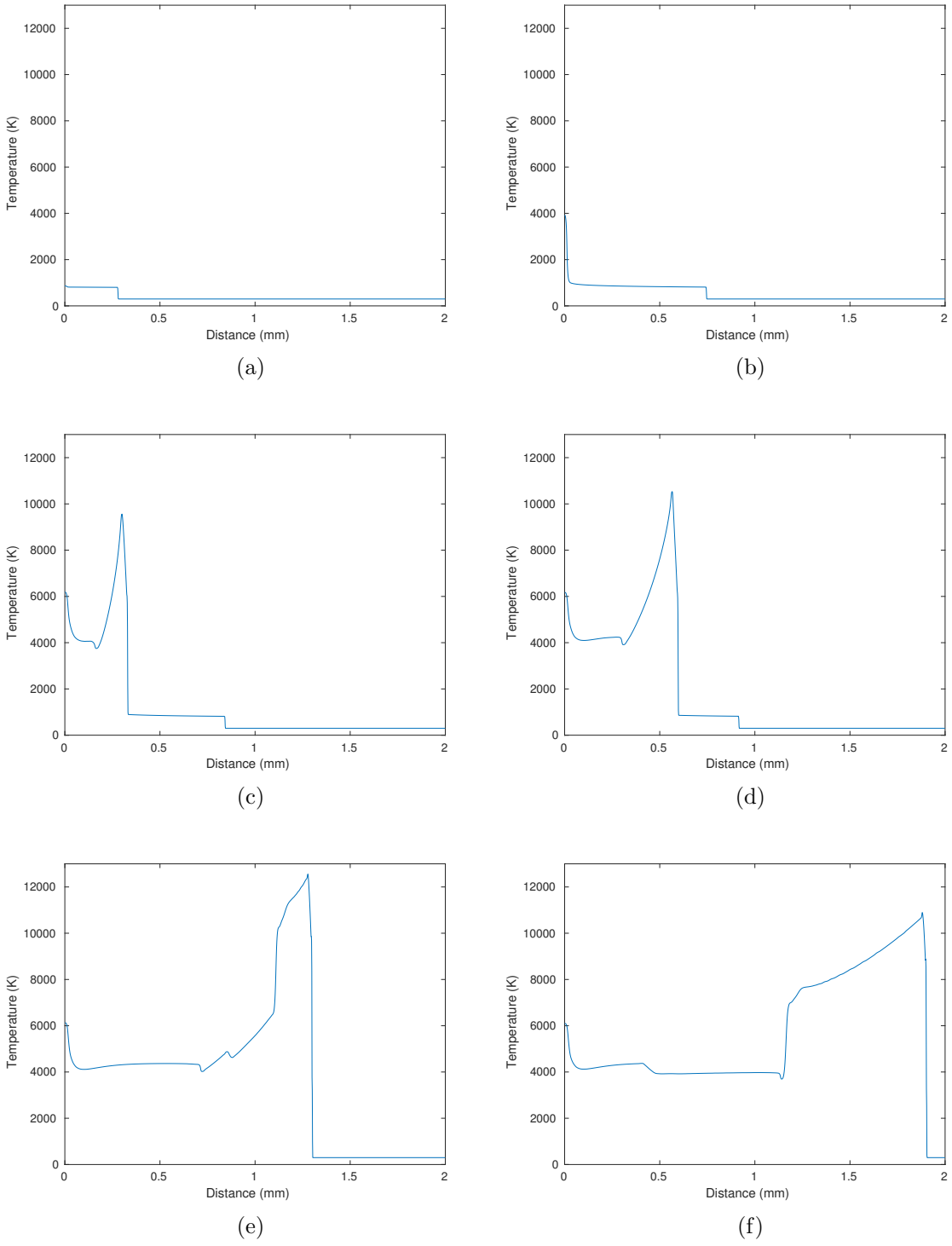

Figure 56. RDX mixture temperature ($\overline{T}$) profiles using ARCIIST with a 0.96 km/s piston at (a) 0.1, **(b)** 0.265, **(c)** 0.3, **(d)** 0.325, **(e)** 0.4, **and (f)** 0.475 μs**.**

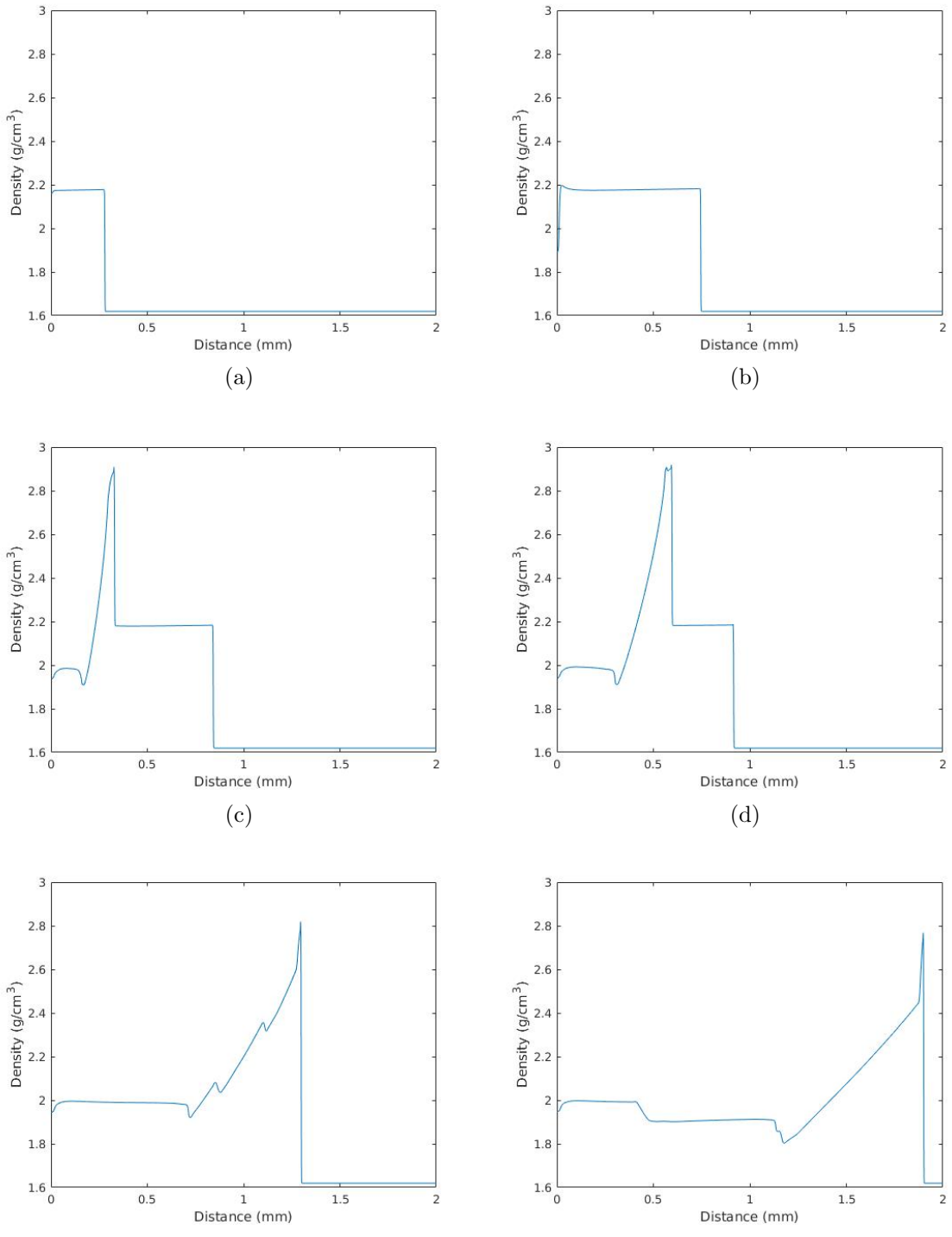

Figure 57. RDX mixture density ($\overline{\rho}$) profiles using ARCIIST with a 0.96 km/s piston at (a) 0.1**, (b)** 0.265**, (c)** 0.3**, (d)** 0.325**, (e)** 0.4**, and (f)** 0.475 μs**.**

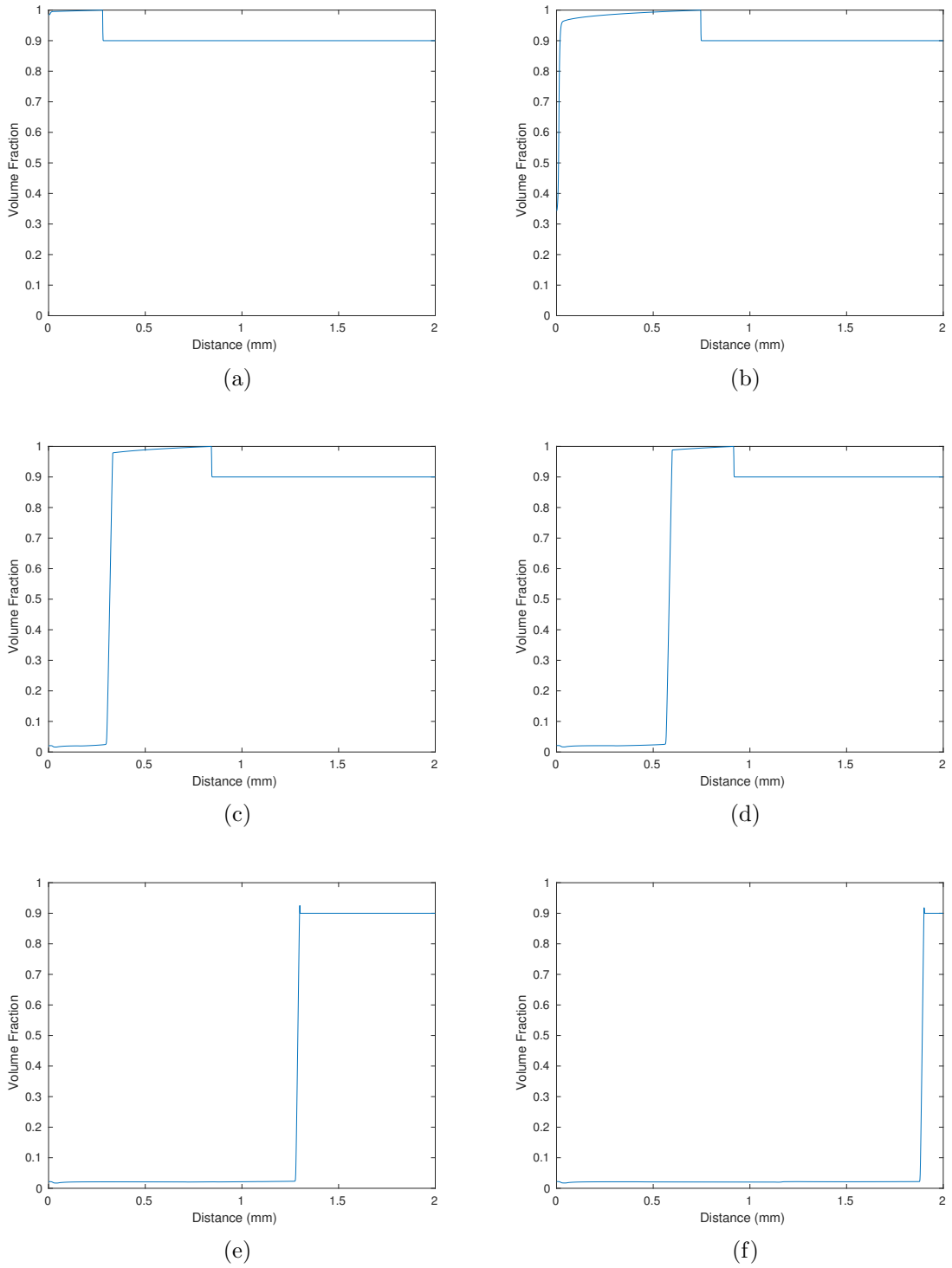

Figure 58. RDX condensed phase volume fraction (ϕ_s) profiles using ARCIIST with a 0.96 km/s piston at (a) 0.1**, (b)** 0.265**, (c)** 0.3**, (d)** 0.325**, (e)** 0.4**, and (f)** 0.475 μs**.**

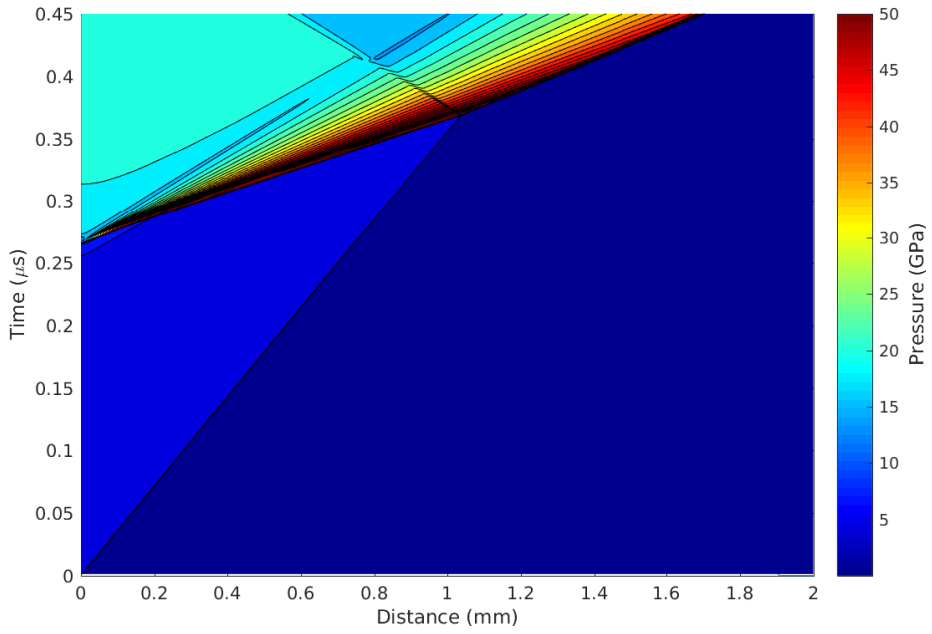

Figure 59. Pressure contour plot from an MPEXS simulation of RDX using ARCIIST. Piston speed was set to 0.96 km/s.

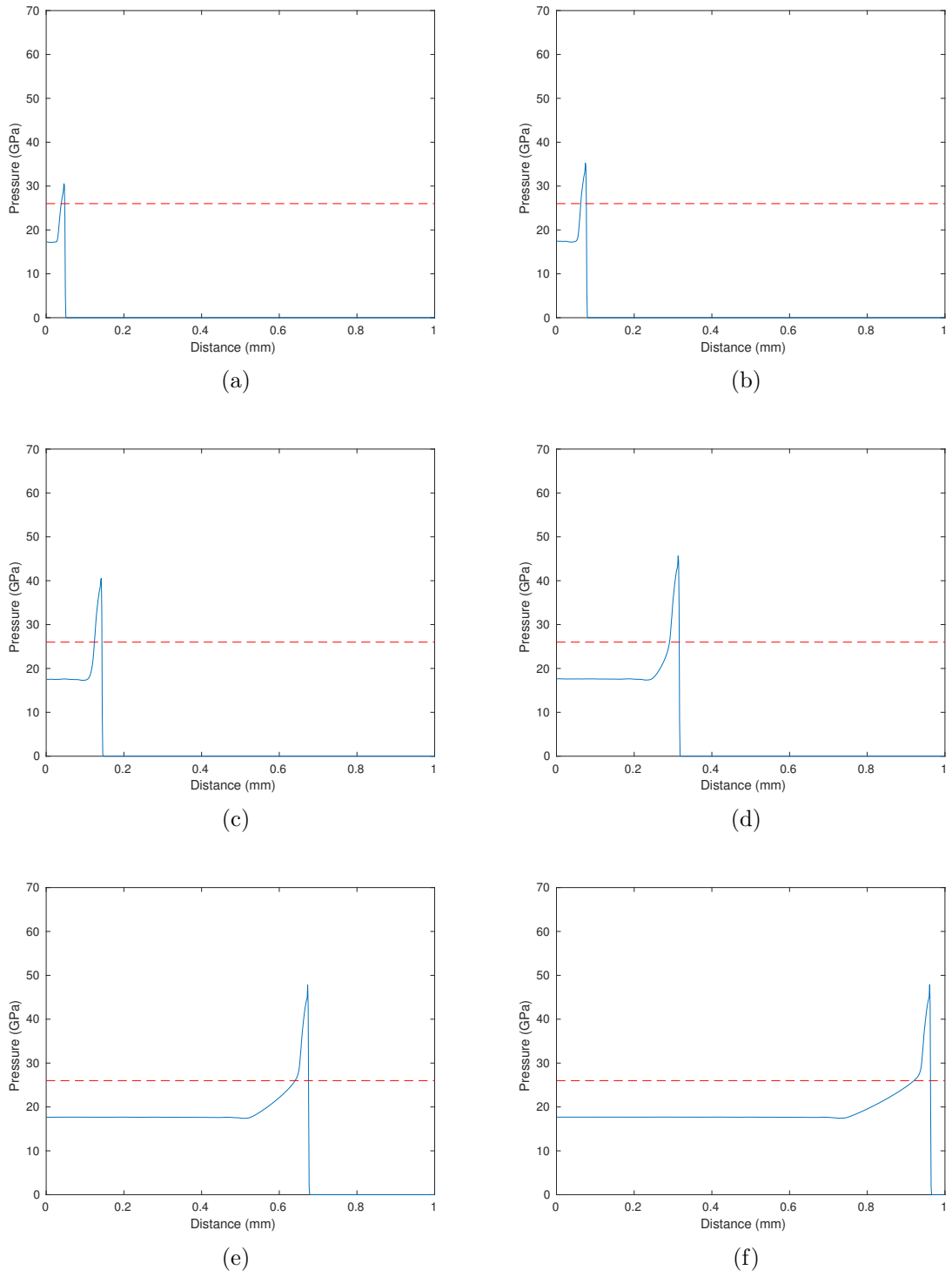

Figure 60. RDX mixture pressure ($\overline{P}$) profiles using ARCIIST with a 1.2 km/s piston at (a) 0.01, (b) 0.015, (c) 0.025, (d) 0.05, (e) 0.1, and (f) 0.14 μs. The dashed red line (- - -) represents RDX CJ pressure.

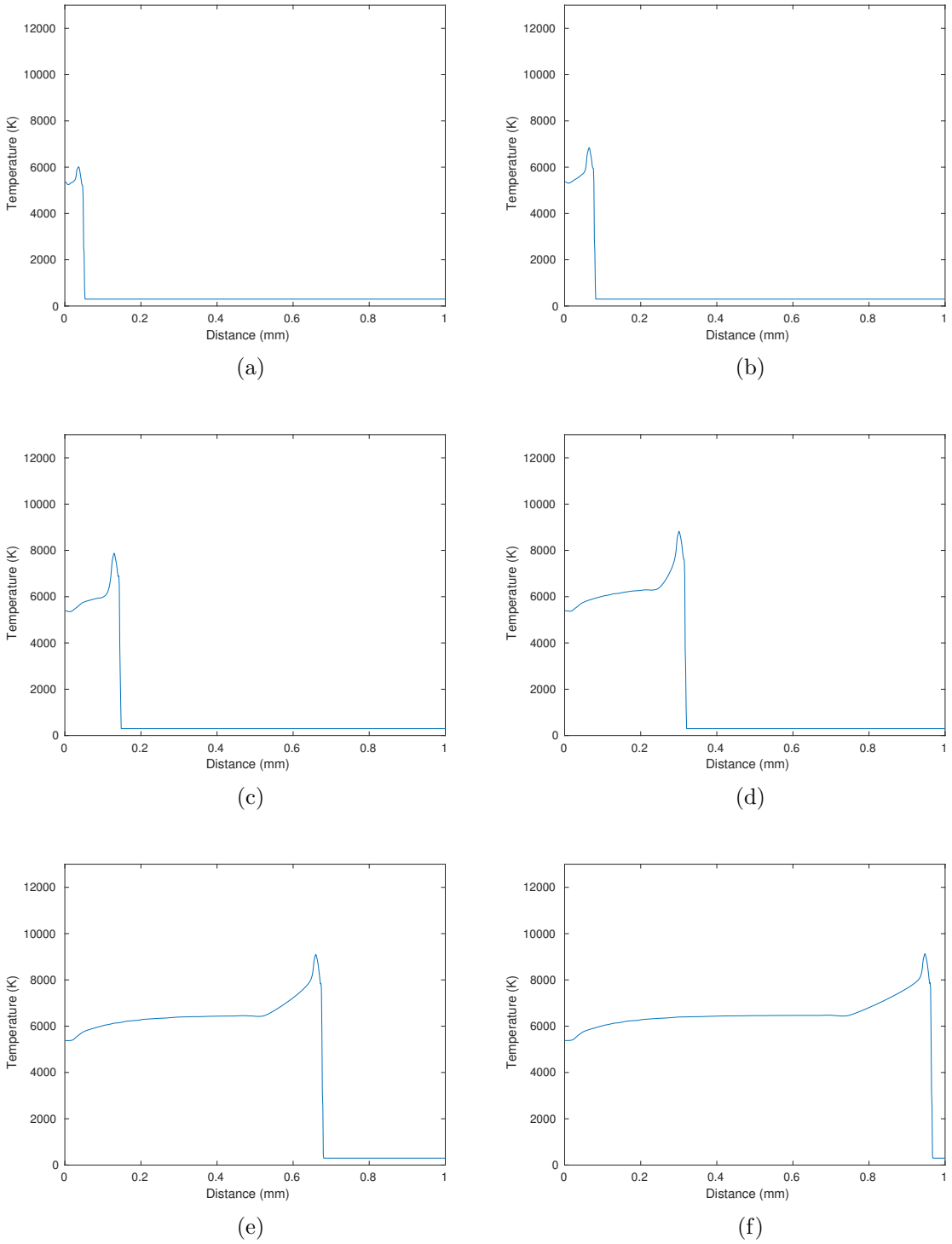

Figure 61. RDX mixture temperature ($\overline{T}$) profiles using ARCIIST with a 1.2 km/s piston at (a) 0.01**, (b)** 0.015**, (c)** 0.025**, (d)** 0.05**, (e)** 0.1**, and (f)** 0.14 μs**.**

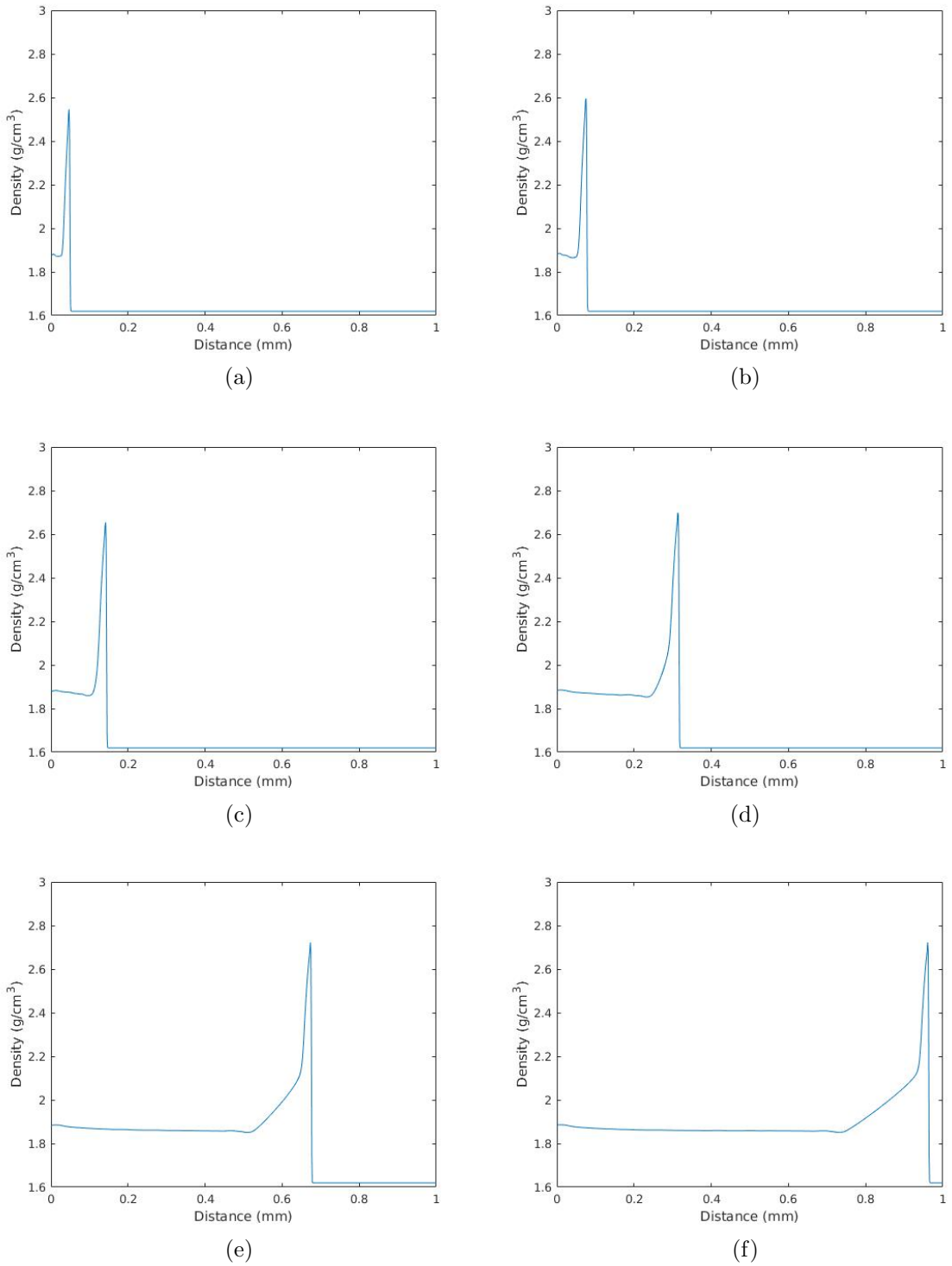

Figure 62. RDX mixture density ($\overline{\rho}$) profiles using ARCIIST with a 1.2 km/s piston at (a) 0.01**, (b)** 0.015**, (c)** 0.025**, (d)** 0.05**, (e)** 0.1**, and (f)** 0.14 μs**.**

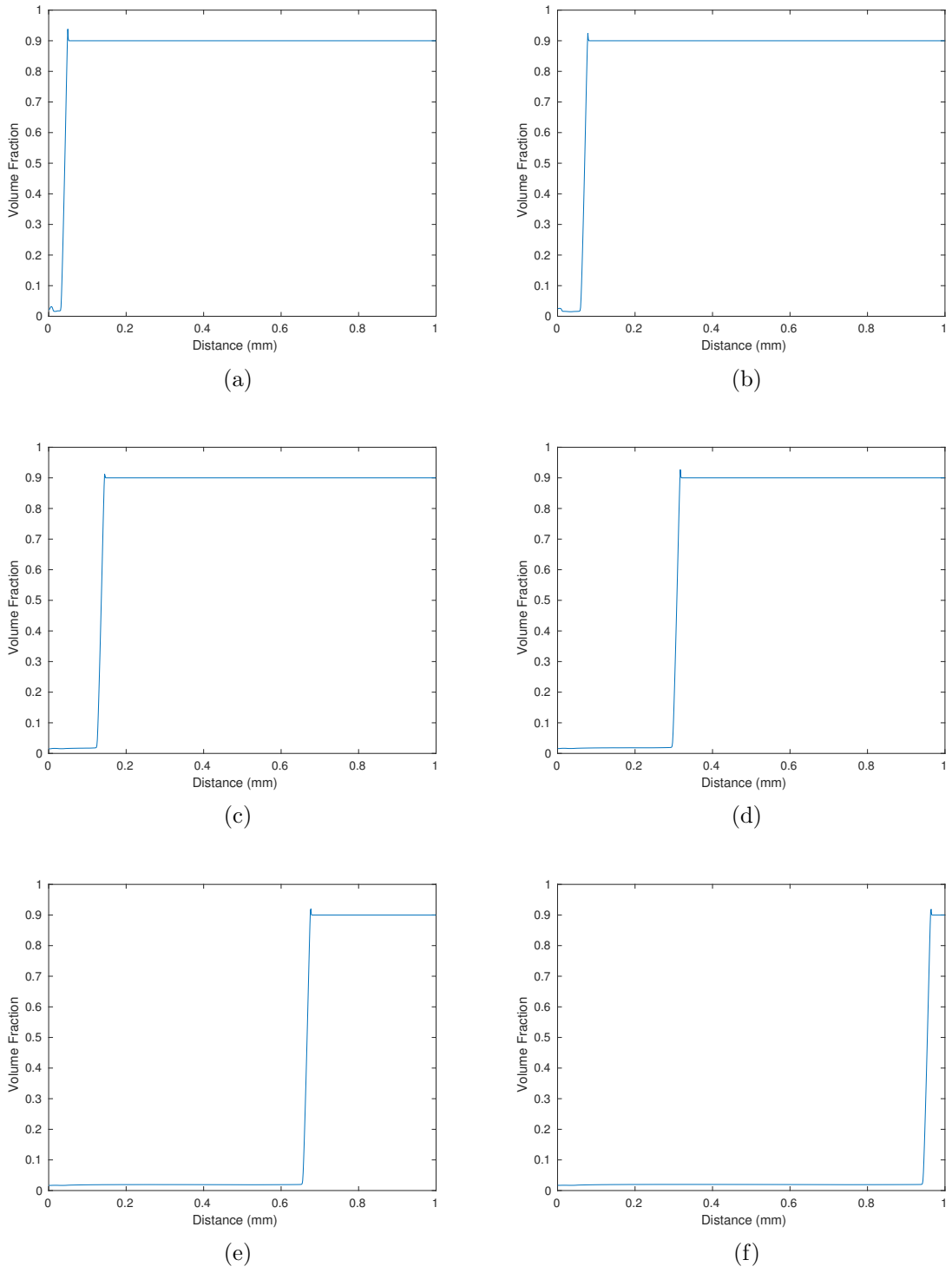

Figure 63. RDX condensed phase volume fraction (ϕ_s) profiles using ARCIIST with a 1.2 km/s piston at (a) 0.01**, (b)** 0.015**, (c)** 0.025**, (d)** 0.05**, (e)** 0.1**, and (f)** 0.14 μs**.**

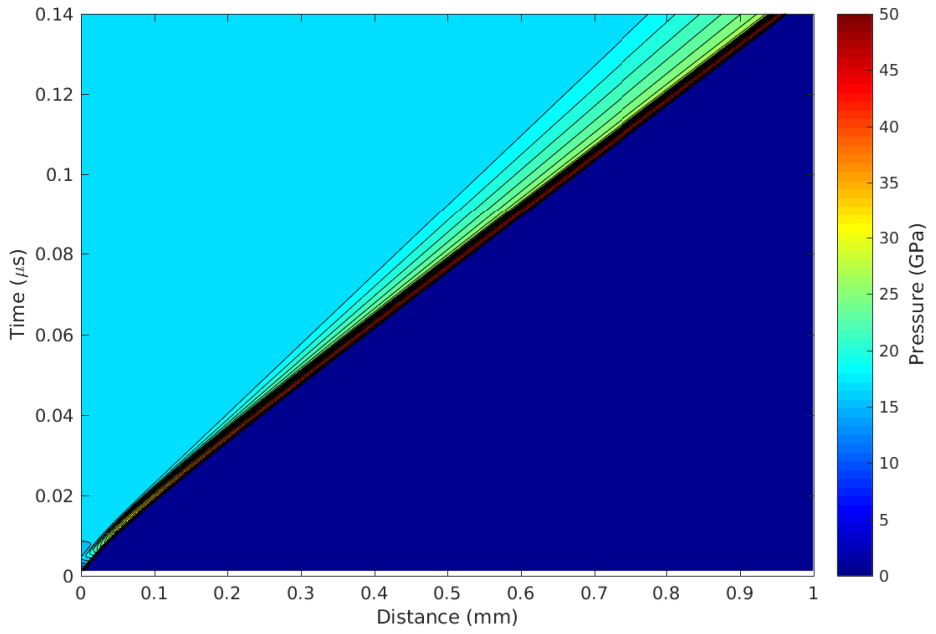

Figure 64. Pressure contour plot from an MPEXS simulation of RDX using ARCIIST. Piston speed was set to 1.2 km/s.

Bibliography

1. "Department of Defense Test Method Standard, Hazard Assessment Tests for Non-Nuclear Munitions". *MIL-STD-2105D*, April 2011.

2. Amar, S., E. Kochavi, Y. Lefler, S. Vaintraub, and D. Sidilkover. "Comparison of BKW and JWL Equations of State for Explosive Simulations". Soreq NRC, Yavne, Israel, July 2015.

3. Baer, M.R. "Modeling heterogeneous energetic materials at the mesoscale". *Thermochimica Acta*, 384(1–2):351–367, 2002. ISSN 0040-6031. URL `http://www.sciencedirect.com/science/article/pii/S0040603101007948`.

4. Baer, M.R. and J.W. Nunziato. "A Two-Phase Mixture Theory for the Deflagration-to-Detonation Transition (DDT) in Reactive Granular Materials". *International Journal of Multiphase Flow*, 12(6):861–889, 1986. ISSN 0301-9322. URL `http://www.sciencedirect.com/science/article/pii/0301932286900339`.

5. Bdzil, J. B., R. Menikoff, S. F. Son, A. K. Kapila, and D. S. Stewart. "Two-phase Modeling of Deflagration-to-Detonation Transition in Granular Materials: Reduced Equations". *Physics of Fluids (1994-present)*, 13(10):3002–3024, 2001. URL `http://scitation.aip.org/content/aip/journal/pof2/13/10/10.1063/1.1398042`.

6. Bedrov, Dmitry, Justin B. Hooper, Grant D. Smith, and Thonas Sewell. "Shock-Induced Transformations in Crystalline RDX: A Uniaxial Constant-Stress Hugoniostat Molecular Dynamics Simulation Study". *The Journal of Chemical Physics*, 131, July 2009.

7. Blazek, Jiri. *Computational Fluid Dynamics: Principles and Applications*. Elsevier, 3rd edition, 2015. ISBN 978-0-08-099995-1.

8. Bobylev, A. V. and T. Ohwada. "The Error of the Splitting Scheme for Solving Evolutionary Equations". *Applied Mathmatics Letters*, 14:45–48, 2001.

9. Bowden, A. W. and A. D Yoffe. *Initiation and Growth of Explosion in Liquids and Solids*. Cambridge University Press, 1952.

10. Campbell, A. W., W. C. Davis, and J. R. Travis. "Shock Initiation of the Detonation in Liquid Explosives". *Physics of Fluids*, 4, 1961.

11. Cawkwell, M. J., T. D. Sewell, L. Zheng, and D. L. Thompson. "Shock-Induced Shear Bands in an Energetic Molecular Crystal: Application of Shock-Front Absorbing Boundary Conditions to Molecular Dynamics Simulations ". *Physical Review B*, B(78), 2008.

12. Chakraborty, Debashis, Richard P. Muller, Siddharth Dasgupta, and William A. Goddard III. *A Detailed Model for the Decomposition of Nitramines: RDX and HMX*. Technical report, California Institute of Technology, Materials and Process Simulation Center.

13. Cook, M. D., P. J. Haskins, and C. Stennett. "Development and Implementation of an Ignition and Growth Model for Homogeneous and Heterogeneous Explosives". *Proceedings of the 11th International Detonation Symposium*, 589–598, 1998.

14. Cooper, Paul W. *Explosives Engineering*. Wiley-VCH, New York, 1996. ISBN 9780471186366.

15. Crochet, Michael Wayne. *Modeling, Numberical Analysis, and Predictions for the Detonation of Multi-Component Energetic Solids*. Dissertation, Louisiana State University, Indiana, December 2013.

16. Crochet, Michael Wayne. "Multiphase Hydrocode Software Quick Start Guide", September 2014. Ver2.

17. Crochet, M.W. and K.A. Gonthier. "Numerical Investigation of a Modified Family of Centered Schemes Applied to Multiphase Equations with Nonconservative Sources". *Journal of Computational Physics*, 255(0):266–292, December 2013. ISSN 0021-9991. URL `http://www.sciencedirect.com/science/article/pii/S002199911300541X`.

18. Crochet, M.W. and K.A. Gonthier. "A Multi-Phase Theory for the Detonation of Granular Explosizes Containing an Arbitrary Number of Solid Components". *International Journal of Multiphase Flow*, (77):76–89, December 2015.

19. Crochet, M.W., K. A. Gronthier, and J. E. Tohline. "Application of a Generalized Multiphase Riemann Solver to a Finite-Volume Method with Nozzling Sources". *AIP Conference Proceedings*, 1426(1):1471–1474, 2012.

20. Davis, James, Sushilkumar Koundinyan, Robert J. Dorgan, Martin Schmidt, and Raymond Ryckman. "Initial Incorporation and Evaluation of Global Reaction Model for Prediction of Chemical Thermal Response". *Joint Army Navy NASA Air Force Meeting*, 46th Combustion Subcommitee, December 2014.

21. Dobratz, B. M. and P. C. Crawford. *LLNL Explosives Handbook. Properties of Chemical Explosives and Explosive Simulants.* Lawrance Livermore National Laboratory, Livermore, 1985.

22. Driels, Morris R. *Weaponeering*. American Institute of Aeronautics and Astronautics, Inc., 2013. ISBN 978-1-6086-925-9.

23. Gibbs, Terry R. and Alphonose Poplato. *LASL Explosive Property Data*. University of California Press, Berkeley, 1980. ISBN 0520040120.

24. Glenn, J. Gregory, Stephen Aubert, and Mac McCormick. *Sympathetic Detonation Predictive Methods*. Technical report, Wright Laboratory, Armament Directorate, August 1993.

25. Gnoffo, Peter A., Roop N. Gupta, and Judy L. Shinn. *Conservation Equations and Physical Models for Hypersonic Air Flows in Thermal and Chemical Nonequilibrium*. Technical report, National Air and Space Administration, February 1989.

26. Goodwin, David G., Harry K. Moffat, and Raymond L. Speth. "Cantera: An Object-oriented Software Toolkit for Chemical Kinetics, Thermodynamics, and Transport Processes". http://www.cantera.org, 2017. Version 2.3.0.

27. Handley, C. A. "The CREST Reactive Burn Model". *Proceedings of the 13th International Detonation Symposium*, 890–894, 2006.

28. Handley, C. A., N. Whitworth, H. James, B. Lambourn, and M-A. Maheswaran. "The CREST Reactive-Burn Model for Explosives". *EPJ Web of Conferences*, 10(4), 2010.

29. Jones, J. D., Xia Ma, B. E. Clements, L. L. Gibson, and R. L. Gustavesen. *Measurement and Reactive Burn Modeling of the Shock to Detonation Transition for the HMX base explosive LX-14*. Technical Report LA-UR-17-25119, Los Alamos National Laboratory, 2017.

30. Klug, Russell. "E-mail conversation with the Director of Engineering, Direct Attack Division, Air Force Life Cycle Management Center", February 2017.

31. Kroonblawd, Matthew P., Thomas D. Sewell, and Jean-Bernard Maillet. "Characteristics of Energy Exchange Between Inter- and Intramolecular Degrees of Freedom in Crystalline 1,3,5-Triamino-2,4,6-Trinitrobenzene (TATB) with Implications for Coarse-Grained Simulations of Shock Waves in Polyatomic Molecular Crystals". *Journal of Chemical Physics*, 144(6), 2016. ISSN 0021-9606.

32. Kurganov, A., S. Noelle, and G. Petrova. "Semidiscrete Central-Upwind Schemes for Hyperbolic Conservation Laws and Hamilton-Jacobi Equations". *SIAM Journal on Scientific Computing*, 23(3):707–740, 2000.

33. Kurganov, A. and E. Tadmor. "New High-Resolution Central Schemes for Nonlinear Conservation Laws and Convection-Diffusion Equations". *Journal of Computational Physics*, 160:241–282, 2000.

34. Lee, E. L. and C. M. Tarver. "Phenomenological Model of Shock Initiation in Heterogeneous Explosives". *Physics of Fluids*, 23(12):2362–2372, 1980.

35. Lu, X., Y. Hamate, and Y. Horie. "Physics Based Ractive Burn Model: Grain Size Effects". *Shock Compression of Condensed Matter Conference Proceedings*, CP 955, 2007.

36. Mader, Charles L. *Numerical Modeling of Explosives and Propellants*. CRC Press, 3rd edition, 2008. ISBN 978-1-4200-5238-1.

37. Nieto, Edwardo. *Simulation of Metal Particulates in High Energetic Materials*. Master's thesis, Air Force Institute of Technology, May 2015.

38. Pereverzev, Andrey and Thomas D. Sewell. "A Theoretical Study of the Relaxation of a Phynyl Group Chemisorbed to and RDX Freestanding Thin Film". *Journal of Chemical Physics*, 145(5), 2016. ISSN 0021-9606.

39. Prasad, Kuldeep, Richard A. Yetter, and Mitchell D. Smooke. "An Eigenvalue Method for Computing the Burning Rates of RDX Propellants". *Combustion Science and Technology*, 124(1-6):35–82, 1997. ISSN 0010-2202.

40. Radhakrishnan, K. and A. C. Hindmarsh. *Description and Use of LSODE, the Livermore Solver for Ordinary Differential Equations*. Technical report, 1993.

41. Schwaab, Matthew J., Robert Greendyke, and Bryan Steward. "Comparison of Burn Rate Models to Reacting Chemistry Model for HMX". *The American Society of Mecahnical Engineers International Mechanical Engineering Congress and Exposition*, November 2016.

42. Schwaab, Matthew J., Robert Greendyke, and Bryan Steward. "Comparison of Finite Chemistry Model to Mixture Pressure Dependent Burn Rate Model for HMX". *Tri-Service Energetic Materials Basic Science Review*, August 2016.

43. Schwaab, Matthew J., Robert Greendyke, and Bryan Steward. "Arrhenius Rate Chemistry-Informed Inter-Phase Source Terms (ARCIIST) ". *20th Biennial International Conference of the APS Topical Group on Shock Compression of Condensed Matter*, July 2017.

44. Schweigert, Igor. "Simulations of Shocked-Induced Chemistry in Materials". *Tri-Service Energetic Materials Basic Science Review*, August 2016.

45. Schweigert, Igor. "Reaction Initiation and Chemical Energy Release in Nitramines". *20th Biennial International Conference of the APS Topical Group on Shock Compression of Condensed Matter*, July 2017.

46. Schwendeman, D. W., C. W. Wahle, and A. K. Kapila. "A Study of Detonation Evolution and Structure for a Model of Compressible Two-Phase Reactive Flow". *Combustion Theory and Modelling*, 12(1):159–204, February 2008. ISSN 13647830.

47. Springer, H. K., C. M. Tarver, J. E. Reaugh, and C. M. May. "Investigating Short-Pulse Shock Initiation in HMX-Based Explosives with Reactive Meso-Scale Simulations". *Journal of Physics: Conference Seriese*, 2014.

48. Stewart, D. S., S. Yoo, and B. L. Wescott. "High-Order Numerical Simulation and Modelling of the Interaction of Energetic and Inert Materials". *Combustion Theory and Modelling*, 11(2):305–332, 2007.

49. Strang, G. "On the construction and comparison of difference schemes. ". *SIAM Journal on Numerical Analysis*, 5(3):506–517, 1968.

50. Thynell, S. T., P. E. Gongwer, and T. B. Brill. "Condensed-Phase Kinetics of Cyclotrimethylenetrinitramine by Modeling the T-jump/Infrared Spectroscopy Experiment". *Journal of Propulsion and Power*, 12:933–939, 1996.

51. Tringe, J. W., J. R. Kercher, H. K. Springer, E. A. Glascoe, H. W. Levie, P. Hsu, T. M. Willey, and J. D. Molitoris. "Numerical and Experimental Study of Thermal Explosions in LX-10 and PBX 9501: Influence of Thermal Damage on Deflagration Processes ". *Journal of Applied Physics*, 114(4), 2013.

52. Trott, Wayne M., Melvin R. Baer, Jaime N. Castaneda, Lalit C. Chhabildas, and James R. Asay. "Investigation of the Mesoscopic Scale Response of Low-Density Pressings of Granular Sugar Under Impact". *Journal of Applied Physics*, 101(2), January 2007.

53. Wescott, B. L., D. S. Stewart, and W.C. Davis. "Equation of State and Reaction Rate for Condensed-Phase Explosives". *Journal of Applied Physics*, 98, 2005.

54. Whitworth, Nicholas. *Mathmatical and Numerical Modelling of Shock Initiation in Heterogeneous Solid Explosives*. Ph.D. thesis, Cranfield University, February 2008.

55. Yetter, R. A., F. L. Dryer, M. T. Allen, and J. L. Gatto. "Development of Gas-Phase Reaction Mechanisms for Nitramine Combustion". *Journal of Propulsion and Power*, 11:683–697, 1995.

56. Zukas, Jonas A. and William P. Walters. *Explosive Effects and Applications*. Springer, 1998. ISBN 978-0-387-95558-2.

REPORT DOCUMENTATION PAGE

Form Approved
OMB No. 0704–0188

1. REPORT DATE *(DD–MM–YYYY)*	2. REPORT TYPE	3. DATES COVERED *(From — To)*
05–31–2018	PhD Dissertation	Oct 2015 — May 2018

4. TITLE AND SUBTITLE

ARRHENIUS RATE CHEMISTRY INFORMED INTER-PHASE SOURCE TERMS (ARCIIST) FOR MACRO-SCALE EXPLOSIVE HYDROCODES

5a. CONTRACT NUMBER

5b. GRANT NUMBER

5c. PROGRAM ELEMENT NUMBER

6. AUTHOR(S)

Matthew J. Schwaab, U.S. Air Force

5d. PROJECT NUMBER

5e. TASK NUMBER

5f. WORK UNIT NUMBER

7. PERFORMING ORGANIZATION NAME(S) AND ADDRESS(ES)

Air Force Institute of Technology
Graduate School of Engineering and Management (AFIT/EN)
2950 Hobson Way
WPAFB OH 45433-7765

8. PERFORMING ORGANIZATION REPORT NUMBER

AFIT-ENY-DS-18-S-072

9. SPONSORING / MONITORING AGENCY NAME(S) AND ADDRESS(ES)

Air Force Office of Scientific Research
875 N Randolph
Arlington VA, 22203

10. SPONSOR/MONITOR'S ACRONYM(S)

AFRL

11. SPONSOR/MONITOR'S REPORT NUMBER(S)

12. DISTRIBUTION / AVAILABILITY STATEMENT

DISTRIBUTION STATEMENT A:
APPROVED FOR PUBLIC RELEASE; DISTRIBUTION UNLIMITED.

13. SUPPLEMENTARY NOTES

14. ABSTRACT

A critical factor in hydrocodes designed to simulate explosive material is defining the chemical reaction rate under various conditions. This rate determines how quickly the granular solid explosive is converted to its gaseous products. Currently, the state of the art for macro-scale hydrocodes is to use one of numerous burn models. These burn models are designed to estimate the bulk chemical reaction rate. Unfortunately, these burn rate models are largely based on empirical data and must be recalibrated for every new material being simulated. This research proposes that the use of Arrhenius Rate Chemistry Informed Interphase Source Terms (ARCIIST) in place of these burn models will not only reduce the reliance of simulations on emperically derived data but will also improve the accuracy for these computational codes. ARCIIST was tested by incorporating an Arrhenius reacting chemistry model developed for the cyclic-nitramine RDX by the Naval Research Laboratory (NRL) into the Air Force Research Laboratory's (AFRL) Multi-Phase Explosive Simulation (MPEXS) continuum hydrocode. ARCIIST demonstrated a unique ability to capture critical features in the deflagration to detonation transition process which were washed out by the common pressure-dependent burn models sunder the same conditions. Furthermore, ARCIIST has successfully linked micro-scale chemical kinetics to macro-scale hydrodynamics. It is, therefore, a critical piece to connecting predictive theoretical chemical kinetics to system scale simulations with less reliance on empirical data.

15. SUBJECT TERMS

ARCIIST, multi-phase, explosive, computational method, hydrocode, burn model, RDX, detonation

16. SECURITY CLASSIFICATION OF:			17. LIMITATION OF ABSTRACT	18. NUMBER OF PAGES	19a. NAME OF RESPONSIBLE PERSON
a. REPORT	b. ABSTRACT	c. THIS PAGE			Dr. Robert B. Greendyke, AFIT/ENY
U	U	U	UU	159	19b. TELEPHONE NUMBER *(include area code)* (937)255-3636x4567; robert.greendyke@afit.edu